

Fall 2013

# An integrated plasma spectroscopic and capacitive sensing platform for water quality diagnostics

John William Sweeney  
*Louisiana Tech University*

Follow this and additional works at: <https://digitalcommons.latech.edu/dissertations>



Part of the [Electrical and Computer Engineering Commons](#)

---

## Recommended Citation

Sweeney, John William, "" (2013). *Dissertation*. 261.  
<https://digitalcommons.latech.edu/dissertations/261>

This Dissertation is brought to you for free and open access by the Graduate School at Louisiana Tech Digital Commons. It has been accepted for inclusion in Doctoral Dissertations by an authorized administrator of Louisiana Tech Digital Commons. For more information, please contact [digitalcommons@latech.edu](mailto:digitalcommons@latech.edu).

**AN INTEGRATED PLASMA SPECTROSCOPIC AND  
CAPACITIVE SENSING PLATFORM FOR WATER  
QUALITY DIAGNOSTICS**

by

John William Sweeney, B.S., M.S.

A Dissertation Presented in Partial Fulfillment  
of the Requirements for the Degree  
Doctor of Philosophy

COLLEGE OF ENGINEERING AND SCIENCE  
LOUISIANA TECH UNIVERSITY

November 2013

UMI Number: 3580364

All rights reserved

INFORMATION TO ALL USERS

The quality of this reproduction is dependent upon the quality of the copy submitted.

In the unlikely event that the author did not send a complete manuscript and there are missing pages, these will be noted. Also, if material had to be removed, a note will indicate the deletion.



UMI 3580364

Published by ProQuest LLC 2014. Copyright in the Dissertation held by the Author.

Microform Edition © ProQuest LLC.

All rights reserved. This work is protected against unauthorized copying under Title 17, United States Code.



ProQuest LLC  
789 East Eisenhower Parkway  
P.O. Box 1346  
Ann Arbor, MI 48106-1346

LOUISIANA TECH UNIVERSITY

THE GRADUATE SCHOOL



October 8, 2013

Date

We hereby recommend that the dissertation prepared under our supervision  
by John William Sweeney

entitled An Integrated Plasma Spectroscopic and Capacitive Sensing Platform  
for Water Quality Diagnostics

be accepted in partial fulfillment of the requirements for the Degree of  
Ph.D. in Engineering

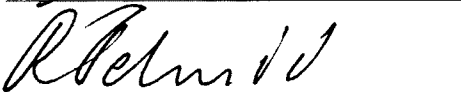
Supervisor of Dissertation Research

Head of Department

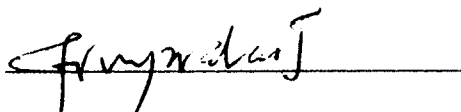
Micro and Nanoscale Systems

Department

Recommendation concurred in:



Advisory Committee




Approved:



Director of Graduate Studies

Approved:



Dean of the Graduate School



Dean of the College

## ABSTRACT

Even in modern times, the consumption of polluted water continues to inflict tremendous suffering on millions of people worldwide that is largely preventable with adequate sanitation practices, routine water quality diagnostics, and treatment. However, conventional water quality monitoring practices remain a time consuming endeavor, where water samples collected on-site are transported to off-site laboratories for evaluation with laboratory-scale chemical analysis devices. While considerable efforts have been made to miniaturize these devices for in-field use, many of the devices reported in the literature provide an incomplete assessment of a water contaminant's environmental impact by focusing on identifying its chemical composition and providing limited or no data regarding the contaminant's concentration.

A water contaminant's chemical composition *and* concentration must be known to adequately assess its human health and environmental impact, as well as coordinating effective restoration and maintenance efforts. The field portable water diagnostic system reported here addresses this need with dual miniaturized plasma spectroscopic and capacitive sensing elements. Both sensing platforms capitalize on a water sample preconcentration stage that isolates contaminant particles from the liquid water solution as a porous thin film. This arrangement yields a more robust spectral emission signature from which the contaminant can be spectroscopically identified and allows the contaminant's concentration to be estimated as a function of the film's capacitance. A

numerical contaminant concentration-to-capacitance model was developed for water samples containing single and multiple contaminant species to interpret the capacitive sensor's output, incorporating the physical parameters of the contaminant material and the device's capacitive analysis chamber which houses the porous contaminant film.

Prototypes of each sensing platform were developed separately to investigate first generation design flaws and optimize the spectroscopic and capacitive analysis procedures. Design modifications for each platform were then incorporated into an integrated diagnostic system, combining both sensing platforms, to perform a complete water quality analysis of a pollutant's chemical composition and concentration. Performance testing of the integrated diagnostic system focused on analyzing representatives of suspended and dissolved water contaminants that promote the incubation and spread of waterborne pathogens at concentration ranges comparable to regulations set by the United States Environmental Protection Agency.

## APPROVAL FOR SCHOLARLY DISSEMINATION

The author grants to the Prescott Memorial Library of Louisiana Tech University the right to reproduce, by appropriate methods, upon request, any or all portions of this Thesis. It is understood that "proper request" consists of the agreement, on the part of the requesting party, that said reproduction is for his personal use and that subsequent reproduction will not occur without written approval of the author of this Thesis. Further, any portions of the Thesis used in books, papers, and other works must be appropriately referenced to this Thesis.

Finally, the author of this Thesis reserves the right to publish freely, in the literature, at any time, any or all portions of this Thesis.

Author John Sweeney

Date 11/4/2013

## **DEDICATION**

I would like to dedicate this work to my father and mother, Ronal and Barbara Sweeney, who continually emphasized the value of an education and selflessly encouraged and supported me along this journey.



## TABLE OF CONTENTS

|  |      |
|--|------|
| ABSTRACT .....                                     | iii  |
| DEDICATION .....                                   | vi   |
| LIST OF TABLES .....                               | xii  |
| LIST OF FIGURES.....                               | xiv  |
| ACKNOWLEDGMENTS.....                               | xvii |
| CHAPTER 1 INTRODUCTION.....                        | 1    |
| 1.1 Importance of the Work.....                    | 1    |
| 1.1.1 The Global Water Crisis .....                | 2    |
| 1.1.2 Response to the Global Water Crisis.....     | 3    |
| 1.2 Total Suspended Solids and Turbidity .....     | 4    |
| 1.3 Health Implications of TSS and Turbidity ..... | 5    |
| 1.4 Water Quality Assessment Methods .....         | 7    |
| 1.4.1 Secchi Disks .....                           | 7    |
| 1.4.2 Nephelometers.....                           | 8    |
| 1.4.3 TSS Measurement Systems .....                | 8    |
| 1.5 Traditional Water Diagnostic Tools .....       | 9    |
| 1.5.1 Gas Chromatographs .....                     | 9    |
| 1.5.2 Mass Spectrometers.....                      | 10   |
| 1.5.3 Plasma Spectrometers.....                    | 10   |
| 1.6 Miniaturized Water Diagnostic Tools .....      | 11   |
| 1.7 Dissertation Objectives.....                   | 13   |

|  |  |    |
|--|--|----|
| 1.8  | Organization of this Dissertation.....             | 17 |
| CHAPTER 2 PLASMA SPECTROSCOPY PRINCIPLES.....        |  | 19 |
| 2.1  | Plasma Physics .....                               | 19 |
| 2.2  | Emission Spectroscopy Physics .....                | 21 |
| CHAPTER 3 PLASMA SPECTROSCOPIC SENSING PLATFORM..... |  | 25 |
| 3.1  | Research Objectives .....                          | 25 |
| 3.2  | Design Considerations.....                         | 26 |
| 3.3  | Plasma Spectroscopic Sensor Design.....            | 27 |
| 3.3.1  | Sample Preconcentration Overview .....             | 28 |
| 3.3.2  | Water Sample Contaminant Preconcentration.....     | 29 |
| 3.3.3  | Plasma Spectroscopic Analysis .....                | 30 |
| 3.4  | Device Fabrication.....                            | 31 |
| 3.5  | Experimental Setup .....                           | 36 |
| 3.6  | Results .....                                      | 37 |
| 3.6.1  | Background Spectral Data .....                     | 37 |
| 3.6.2  | Al <sub>2</sub> O <sub>3</sub> Spectral Data ..... | 41 |
| 3.6.3  | CaCO <sub>3</sub> Spectral Data .....              | 43 |
| 3.6.4  | CuO Spectral Data .....                            | 44 |
| 3.6.5  | FeO Spectral Data.....                             | 46 |
| 3.6.6  | MgO Spectral Data .....                            | 47 |
| 3.6.7  | NaCl Spectral Data .....                           | 49 |
| 3.6.8  | Microheater Performance .....                      | 50 |
| 3.7  | Discussion.....                                    | 51 |
| 3.7.1  | Design Issues .....                                | 51 |
| 3.7.2  | Experimental Issues.....                           | 53 |

|  |    |
|--|----|
| 3.8 Conclusion.....  | 54 |
| CHAPTER 4 CAPACITIVE SENSING PRINCIPLES.....               | 55 |
| 4.1 Capacitor Physics .....                                | 55 |
| 4.2 Capacitor Circuits.....                                | 56 |
| 4.3 Dielectric Properties of Composite Materials .....     | 57 |
| 4.3.1 Weiner's Limits .....                                | 58 |
| 4.3.2 Lichtenecker's Mixture Formulation.....              | 58 |
| 4.3.3 Modified Lichtenecker Mixture Formulation.....       | 59 |
| CHAPTER 5 CAPACITIVE SENSING PLATFORM.....                 | 62 |
| 5.1 Research Objectives .....                              | 62 |
| 5.2 Design Considerations.....                             | 63 |
| 5.3 Capacitive Sensor Design.....                          | 64 |
| 5.3.1 Design Modifications .....                           | 65 |
| 5.3.2 Device Parameters .....                              | 67 |
| 5.4 Contaminant Concentration Models.....                  | 69 |
| 5.4.1 Single Contaminant Concentration Model .....         | 70 |
| 5.4.2 Multiple Contaminant Concentration Model.....        | 75 |
| 5.5 Device Fabrication.....                                | 78 |
| 5.6 Experimental Setup .....                               | 81 |
| 5.6.1 Sensor Calibration .....                             | 82 |
| 5.7 Results .....  | 86 |
| 5.7.1 Single Contaminant Theoretical Predictions .....     | 88 |
| 5.7.2 Al <sub>2</sub> O <sub>3</sub> Capacitance Data..... | 90 |
| 5.7.3 NaCl Capacitance Data.....                           | 94 |
| 5.7.4 SiO <sub>2</sub> Capacitance Data.....               | 98 |

|   |   |     |
|---|---|-----|
| 5.7.5                                       | Multiple Contaminant Theoretical Predictions.....                       | 101 |
| 5.7.6                                       | Equal Contaminant Mixture Capacitance Data .....                        | 104 |
| 5.7.7                                       | Al <sub>2</sub> O <sub>3</sub> -Dominant Mixture Capacitance Data ..... | 107 |
| 5.7.8                                       | NaCl-Dominant Mixture Capacitance Data .....                            | 110 |
| 5.7.9                                       | SiO <sub>2</sub> -Dominant Mixture Capacitance Data .....               | 113 |
| 5.8   | Discussion.....   | 116 |
| 5.8.1                                       | Capacitive Sensor Design Issues .....                                   | 116 |
| 5.8.2                                       | Numerical Concentration-to-Capacitance Model Issues .....               | 117 |
| 5.8.3                                       | Experimental Setup Issues.....  | 117 |
| 5.9   | Conclusion.....   | 118 |
| CHAPTER 6 INTEGRATED SENSING PLATFORM ..... |   | 119 |
| 6.1   | Research Objectives .....   | 119 |
| 6.2   | Design Considerations.....  | 119 |
| 6.2.1                                       | Plasma Spectroscopic Platform Modifications.....                        | 120 |
| 6.2.2                                       | Capacitive Sensing Platform Modifications .....                         | 120 |
| 6.3   | Integrated Sensor Design.....   | 121 |
| 6.4   | Modified Single Contaminant Concentration Model .....                   | 124 |
| 6.4.1                                       | Bulk Density Optimization.....  | 125 |
| 6.4.2                                       | Modified Lichtenecker Equation .....                                    | 126 |
| 6.4.3                                       | Capacitor Plate Oxides .....  | 127 |
| 6.5   | Device Fabrication.....   | 129 |
| 6.6   | Experimental Setup .....  | 131 |
| 6.7   | Results .....   | 134 |
| 6.7.1                                       | Baseline/Theoretical Capacitance Predictions.....                       | 134 |
| 6.7.2                                       | CaCO <sub>3</sub> Spectral Data .....                                   | 136 |

|              |   |     |
|--------------|---|-----|
| 6.7.3        | CaCO <sub>3</sub> Capacitance Data.....           | 138 |
| 6.7.4        | MgO Spectral Data .....                           | 142 |
| 6.7.5        | MgO Capacitance Data.....                         | 143 |
| 6.7.6        | NaCl Spectral Data .....                          | 148 |
| 6.7.7        | NaCl Capacitance Data.....                        | 150 |
| 6.8          | Discussion.....                                   | 154 |
| 6.9          | Conclusion.....                                   | 155 |
| APPENDIX A   | COMPREHENSIVE SPECTRAL LINE DATA.....             | 156 |
| APPENDIX B   | FIRST GENERATION SINGLE CONTAMINANT MODEL.....    | 159 |
| APPENDIX C   | FIRST GENERATION MULTIPLE CONTAMINANT MODEL ..... | 161 |
| APPENDIX D   | SECOND GENERATION SINGLE CONTAMINANT MODEL .....  | 164 |
| BIBLIOGRAPHY | .....   | 167 |

## LIST OF TABLES

|  |     |
|--|-----|
| <b>Table 5-1:</b> Theoretical baseline capacitances as a function of plate spacing. ....                         | 68  |
| <b>Table 5-2:</b> Calibration results used to determine optimal plate separation distance. ....                  | 85  |
| <b>Table 5-3:</b> Calibration/fringe capacitance results for each plate separation distance.....                 | 85  |
| <b>Table 5-4:</b> Physical parameters of single contaminant porous films.....                                    | 88  |
| <b>Table 5-5:</b> Theoretical parameters of the Al <sub>2</sub> O <sub>3</sub> contaminant particle films. ....  | 90  |
| <b>Table 5-6:</b> Theoretical and experimental data summary for Al <sub>2</sub> O <sub>3</sub> contaminants..... | 94  |
| <b>Table 5-7:</b> Theoretical parameters of the NaCl contaminant particle films. ....                            | 95  |
| <b>Table 5-8:</b> Theoretical and experimental data summary for NaCl contaminants.....                           | 97  |
| <b>Table 5-9:</b> Theoretical parameters of the SiO <sub>2</sub> contaminant particle films. ....                | 98  |
| <b>Table 5-10:</b> Theoretical and experimental data summary for SiO <sub>2</sub> contaminants.....              | 100 |
| <b>Table 5-11:</b> Multi-contaminant mixture concentration model parameters.....                                 | 101 |
| <b>Table 5-12:</b> Theoretical parameters of the equal contaminant mixture films.....                            | 104 |
| <b>Table 5-13:</b> Theo/Exp data summary for equal mixture contaminants films. ....                              | 106 |
| <b>Table 5-14:</b> Theoretical parameters of the Al <sub>2</sub> O <sub>3</sub> -dominant mixture films. ....    | 107 |
| <b>Table 5-15:</b> Theo/Exp data summary for Al <sub>2</sub> O <sub>3</sub> -dominant mixture films. ....        | 109 |
| <b>Table 5-16:</b> Theoretical parameters of the NaCl-dominant mixture films. ....                               | 110 |
| <b>Table 5-17:</b> Theo/Exp data summary for NaCl-dominant mixture films. ....                                   | 112 |
| <b>Table 5-18:</b> Theoretical parameters of the SiO <sub>2</sub> -dominant mixture films. ....                  | 113 |
| <b>Table 5-19:</b> Theo/Exp data summary for SiO <sub>2</sub> -dominant mixture films. ....                      | 115 |
| <b>Table 6-1:</b> Cu oxide film parameters.....  | 129 |
| <b>Table 6-2:</b> Simulated contaminant parameters based on reference bulk densities. ....                       | 135 |

|   |     |
|---|-----|
| <b>Table 6-3:</b> Theo/Exp data summary for CaCO <sub>3</sub> films, for reference $\eta$ .....             | 139 |
| <b>Table 6-4:</b> Theo/Exp data summary for CaCO <sub>3</sub> films, with optimized $\eta$ and offset. .... | 141 |
| <b>Table 6-5:</b> CaCO <sub>3</sub> film parameters based on optimized $\eta$ . ....                        | 141 |
| <b>Table 6-6:</b> Theo/Exp data summary for MgO films, for reference $\eta$ .....                           | 145 |
| <b>Table 6-7:</b> Theo/Exp data summary for MgO films, with optimized $\eta$ and offset. ....               | 147 |
| <b>Table 6-8:</b> MgO film parameters based on optimized $\eta$ . ....                                      | 148 |
| <b>Table 6-9:</b> Theo/Exp data summary for NaCl films, for reference $\eta$ .....                          | 151 |
| <b>Table 6-10:</b> Theo/Exp data summary for NaCl films, with optimized $\eta$ and offset. ....             | 153 |
| <b>Table 6-11:</b> NaCl film parameters based on optimized $\eta$ . ....                                    | 154 |
| <b>Table A-1:</b> Comprehensive atomic and molecular spectral line data.....                                | 157 |

## LIST OF FIGURES

|   |    |
|---|----|
| <b>Figure 1-1:</b> Overview of the capacitive/spectroscopic analysis procedure. ....                      | 15 |
| <b>Figure 2-1:</b> Plasma behavior modeled with a simple monatomic gas. ....                              | 20 |
| <b>Figure 2-2:</b> Overview of plasma emission spectroscopy procedure. ....                               | 23 |
| <b>Figure 2-3:</b> Sample emission spectrum of Hg. ....   | 24 |
| <b>Figure 3-1:</b> Plasma spectroscopic analysis procedure. ....  | 30 |
| <b>Figure 3-2:</b> Microheater/electrode mask patterns used for the first generation device. ...          | 32 |
| <b>Figure 3-3:</b> Fabrication process for the first generation plasma spectroscopic sensor. ....         | 33 |
| <b>Figure 3-4:</b> Finalized plasma spectroscopic prototypes for each mask pattern. ....                  | 35 |
| <b>Figure 3-5:</b> Air background spectrum of the first testing session. ....                             | 38 |
| <b>Figure 3-6:</b> Close-up of the first session air background spectrum. ....                            | 38 |
| <b>Figure 3-7:</b> Air background spectrum of second testing session. ....                                | 40 |
| <b>Figure 3-8:</b> Close-up of the second session air background spectrum. ....                           | 40 |
| <b>Figure 3-9:</b> Al <sub>2</sub> O <sub>3</sub> atomic and molecular fragment spectrum at 100 ppm. .... | 42 |
| <b>Figure 3-10:</b> CaCO <sub>3</sub> atomic and molecular fragment spectrum at 100 ppm. ....             | 43 |
| <b>Figure 3-11:</b> CuO atomic fragment spectrum at 10 ppm. ....  | 45 |
| <b>Figure 3-12:</b> Cu ion spectral line intensity versus concentration. ....                             | 45 |
| <b>Figure 3-13:</b> FeO atomic fragment spectrum at 10 ppm. ....  | 46 |
| <b>Figure 3-14:</b> Fe ion spectral line intensity versus concentration. ....                             | 47 |
| <b>Figure 3-15:</b> MgO atomic and molecular fragment spectrum at 100 ppm. ....                           | 48 |
| <b>Figure 3-16:</b> NaCl atomic fragment spectrum at 10 ppm. ....   | 49 |



|  |     |
|--|-----|
| <b>Figure 3-17: Na ion spectral line intensity versus concentration.</b> .....   | 50  |
| <b>Figure 4-1: Parallel-connected capacitor network.</b> .....   | 57  |
| <b>Figure 4-2: Series-connected capacitor network.</b> .....   | 57  |
| <b>Figure 5-1: Capacitive analysis of water contaminant concentration.</b> .....   | 64  |
| <b>Figure 5-2: Parallel dielectric layers of the contaminant particle film and air space.</b> .....                          | 70  |
| <b>Figure 5-3: Effective volume of contaminant particles and voids in the porous film.</b> .....                             | 71  |
| <b>Figure 5-4: Fabrication process for the first generation capacitive sensor.</b> .....                                     | 80  |
| <b>Figure 5-5: Experimental setup used to calibrate and test the capacitive sensor.</b> .....                                | 81  |
| <b>Figure 5-6: Calibration results for each plate spacing</b> .....  | 83  |
| <b>Figure 5-7: Simulated single contaminant capacitances for each electrode spacing</b> .....                                | 89  |
| <b>Figure 5-8: Theoretical and experimental results for Al<sub>2</sub>O<sub>3</sub> films, <math>d=0.59</math> mm.</b> ..... | 92  |
| <b>Figure 5-9: Theoretical and experimental results for Al<sub>2</sub>O<sub>3</sub> films, <math>d=1.0</math> mm.</b> .....  | 92  |
| <b>Figure 5-10: Theoretical and experimental results for NaCl films, <math>d=0.59</math> mm.</b> .....                       | 96  |
| <b>Figure 5-11: Theoretical and experimental results for NaCl films, <math>d=1.0</math> mm.</b> .....                        | 96  |
| <b>Figure 5-12: Theoretical and experimental results for SiO<sub>2</sub> films, <math>d=0.59</math> mm.</b> .....            | 99  |
| <b>Figure 5-13: Theoretical and experimental results for SiO<sub>2</sub> films, <math>d=1.0</math> mm.</b> .....             | 99  |
| <b>Figure 5-14: Multi-contaminant theoretical capacitances for each electrode spacing.</b> ..                                | 103 |
| <b>Figure 5-15: Theo/Exp data for equal contaminant mixture films, <math>d=0.59</math> mm.</b> .....                         | 105 |
| <b>Figure 5-16: Theo/Exp data for equal contaminant mixture films, <math>d=1.0</math> mm.</b> .....                          | 105 |
| <b>Figure 5-17: Theo/Exp data for Al<sub>2</sub>O<sub>3</sub>-dominant mixture films, <math>d=0.59</math> mm.</b> .....      | 108 |
| <b>Figure 5-18: Theo/Exp data for Al<sub>2</sub>O<sub>3</sub>-dominant mixture films, <math>d=1.0</math> mm.</b> .....       | 108 |
| <b>Figure 5-19: Theo/Exp data for NaCl-dominant mixture films, <math>d=0.59</math> mm.</b> .....                             | 111 |
| <b>Figure 5-20: Theo/Exp data for NaCl-dominant mixture films, <math>d=1.0</math> mm.</b> .....                              | 111 |
| <b>Figure 5-21: Theo/Exp data for SiO<sub>2</sub>-dominant mixture films, <math>d=0.59</math> mm.</b> .....                  | 114 |
| <b>Figure 5-22: Theo/Exp data for SiO<sub>2</sub>-dominant mixture films, <math>d=1.0</math> mm.</b> .....                   | 114 |

|   |     |
|---|-----|
| <b>Figure 6-1:</b> Three layer schematic of the integrated sensor prototype. ....                         | 122 |
| <b>Figure 6-2:</b> Capacitive/spectroscopic analysis procedure for the integrated device. ....            | 123 |
| <b>Figure 6-3:</b> Cu capacitor plate oxide capacitor representation and schematic. ....                  | 127 |
| <b>Figure 6-4:</b> Fabrication process for the integrated sensor. ....                                    | 130 |
| <b>Figure 6-5:</b> Finalized integrated sensor prototype.....   | 131 |
| <b>Figure 6-6:</b> Experimental setup used to test the integrated sensor prototype.....                   | 132 |
| <b>Figure 6-7:</b> Theoretical contaminant capacitances based on reference bulk densities... 135          |     |
| <b>Figure 6-8:</b> CaCO <sub>3</sub> atomic and molecular fragment spectra at 3.5 g/L. ....               | 136 |
| <b>Figure 6-9:</b> CaCO <sub>3</sub> fragment spectral line intensity versus concentration. ....          | 137 |
| <b>Figure 6-10:</b> Theo/Exp results for CaCO <sub>3</sub> films, for reference $\eta$ . ....             | 138 |
| <b>Figure 6-11:</b> Theo/Exp results for CaCO <sub>3</sub> films, with optimized $\eta$ .....             | 140 |
| <b>Figure 6-12:</b> Theo/Exp results for CaCO <sub>3</sub> films, for optimized $\eta$ , with offset..... | 140 |
| <b>Figure 6-13:</b> MgO atomic and molecular fragment spectra at 5 g/L.....                               | 142 |
| <b>Figure 6-14:</b> MgO fragment spectral line intensity versus concentration. ....                       | 143 |
| <b>Figure 6-15:</b> Theo/Exp results for MgO films, for reference $\eta$ . ....                           | 144 |
| <b>Figure 6-16:</b> Theo/Exp results for MgO films, with optimized $\eta$ .....                           | 146 |
| <b>Figure 6-17:</b> Theo/Exp results for MgO films, for optimized $\eta$ , with offset.....               | 146 |
| <b>Figure 6-18:</b> NaCl atomic and molecular fragment spectra at 5 g/L.....                              | 149 |
| <b>Figure 6-19:</b> NaCl fragment spectral line intensity versus concentration. ....                      | 149 |
| <b>Figure 6-20:</b> Theo/Exp results for NaCl films, for reference $\eta$ . ....                          | 150 |
| <b>Figure 6-21:</b> Theo/Exp results for NaCl films, with optimized $\eta$ .....                          | 152 |
| <b>Figure 6-22:</b> Theo/Exp results for NaCl films, for reference $\eta$ , with offset.....              | 152 |

## ACKNOWLEDGMENTS

I would like to thank my advisors—Dr. Lee Sawyer and Dr. Chester Wilson—for their guidance and support throughout my graduate career. I would also like to thank each of my PhD committee members—Dr. Randy Null, Dr. Sven Eklund, Dr. Rastko Selmic, Dr. Long Que, and Dr. Arun Jaganathan—for their helpful feedback and encouragement as the projects reported here were underway and during the preparation of this work.

I would also like to thank the technical staff at Louisiana Tech’s Institute for Micromanufacturing—Debbie Wood, Dee Tatum, Dr. Alfred Gunasekaran, Dr. John McDonald, and the late Scott Williams—whose support and technical expertise were an invaluable asset toward completing the projects reported here.

I am also grateful to the Louisiana Space Consortium (LaSPACE), the National Science Foundation, and the Louisiana Board of Regents for providing the fellowship funding support that allowed me to pursue this degree.

Finally, I would like to thank my father, mother, brother, and my friends for their unwavering support and encouragement throughout my educational experience.

# **CHAPTER 1**

## **INTRODUCTION**

### **1.1 Importance of the Work**

Water is the biological foundation for all life on Earth and is essential for maintaining the planet's diverse ecosystem. All flora and fauna species require water for a host of biological functions, including hydration, respiration, production of food and energy, or as a habitat. Human civilization places additional demands on water for sanitation, economic, and social purposes. In the modern world, secure global sources of clean water provide the substrate upon which healthy and stable societies are built.

Yet throughout the developed and developing world, maintaining the purity of natural and manmade water sources requires constant vigilance. Human activities and natural processes can often jeopardize the potability of water reserves with serious public health, ecological, political, and economic consequences. Water contamination resulting from human efforts—such as industrial wastewater discharges, urban runoff, corrosion of plumbing systems, and improperly managed sewage, among others—can introduce a wide range of potential contaminant species with acute human health and ecological consequences. Natural geological events—including floodwater runoff and the erosion of rock and mineral deposits—also represent a significant source of water pollution. Even today, clean water remains a fragile commodity, particularly in the developing world

where potable water reserves are often scarce and the resources for regulation and maintenance are often inadequate.

The diversity of water contaminants that could be encountered in a water diagnostic scenario is vast, ranging from organic, inorganic, microbial, pesticides, herbicides, and radioactive pollutants [1]. However, the classification of water contaminant is not limited to species that are inherently toxic to humans or the environment. For example, waters with high inert particle concentrations or *turbidity* also pose a significant environmental risk by supporting the growth and spread of waterborne pathogens [2]. The high concentrations of biological waste typically found in turbid waters have been demonstrated to simultaneously supply nourishment to meager pathogen cultures and neutralize disinfection agents, allowing rapid population growth. The water medium also provides the pathogen culture with an efficient means of expansion and route of infection for humans when consumed or used for sanitation.

#### 1.1.1 The Global Water Crisis

According to a 2008 World Health Organization report on global water-related issues, inadequate access to potable water for drinking and sanitation is estimated to account for 9.1% of diseases and 6.3% of fatalities worldwide [3]. In 2002 alone, illnesses contracted from consuming or handling polluted water were responsible for over 6.2 million deaths. The developing immune systems of children under the age of five are particularly susceptible to waterborne illnesses. For example, diarrhea and the subsequent malnutrition resulting from consuming pathogen-infested water claims the lives of over 1.4 million children every year in developing nations. Recognizing that these water-

related illnesses are largely preventable with adequate water quality regulations and diagnostic tools renders these grim statistics even more tragic.

Today, an estimated 783 million people still lack access to clean drinking water and 2.5 billion (approximately 35% of the world's population) are without access to clean water for sanitation [4]. The vast majority of those afflicted with poor water options live in the developing nations of sub-Saharan Africa and southern and eastern Asia. However, the governmental regulations and complex water systems of developed nations are not immune to waterborne pathogen outbreaks. For example, between 1920 and 2002, 1870 waterborne pathogen outbreaks were reported in the United States, resulting in 883,806 infections and 1165 fatalities [5]. In response to these alarming statistics, organizations such as the United States' National Academy of Engineering has projected that securing and maintaining global potable water reserves will be one of greatest challenges humanity faces in the 21<sup>st</sup> century [6].

#### 1.1.2 Response to the Global Water Crisis

Today, water quality diagnostics largely remains an off-site endeavor. In a typical environmental testing scenario, multiple water samples are collected on-site and transported to off-site laboratories for evaluation with traditional, laboratory-scale chemical analysis devices. In recent decades, researchers in governments, industry, and academia have responded to the world's water crisis by investing considerable resources into the development of portable diagnostic devices that can provide a quick, on-site water quality analysis. While field portability and real-time monitoring capabilities have been the primary goals motivating this research, these efforts will also likely lead to more economical diagnostic tools that require less power and simpler manufacturing

techniques based on lithographic and batch fabrication processes. The development of portable and inexpensive (or even essentially disposable) water diagnostic devices would also support efforts toward improving access to potable water in the developing world, where resources for environmental regulations and monitoring are often limited.

However, many of the miniaturized diagnostic devices reported from these efforts have focused primarily on identifying a water contaminant's chemical composition and often offer limited or no information regarding its concentration. Water quality surveys made with such devices could in turn yield an incomplete assessment of the human health and environmental consequences of a contamination event and reduce the effectiveness of coordinated clean up efforts. The lack of impurity concentration data could also have disastrous consequences when the contaminant species in question may be generally non-toxic at low concentrations but supports the incubation of waterborne pathogens at higher concentrations, as described earlier.

In light of this situation, the primary research focus of this dissertation will be toward the development of a complete water quality diagnostic system that can be used to identify a water contaminant's chemical composition *and* concentration. Additionally, this work will strive to minimize the diagnostic system's packaging for field portability as well as its material and fabrication costs, where possible, to encourage the adoption of water quality devices such as this in the developing world.

## **1.2 Total Suspended Solids and Turbidity**

With respect to environmental regulations regarding water quality, *turbidity* and *total suspended solids (TSS)* are two common parameters used to describe the concentration of dissolved and suspended particles in a water source, respectively.

Turbidity is a measurement of the optical transparency of a water sample and refers to the degree of “cloudiness” or “haziness” as the result of light scattered from dissolved particulates [2]. Using this parameter, high turbidity represents a high particle concentration with low transparency and low turbidity represents a low particle concentration with high transparency. Prior to the introduction of inexpensive photodetectors, turbidity measurements were made with a technician’s naked-eye comparisons of a water sample’s transparency against that of a pre-concentrated standard and remained a subjective diagnostic tool.

The quantity of total suspended solids in a water sample, however, is a direct measurement of particle concentration and is expressed as a density in grams-per-liter (g/L) [7]. The TSS analysis process consists of filtering a known volume of water through a microfiber filter and measuring the mass of particles that accumulate on the filter to determine the density of particles in the sample (mass divided by volume). Because turbidity and TSS measurements represent similar water quality parameters, many environmental regulatory agencies often use the terms interchangeably in their literature. However, the TSS parameter will be the focus of this research, as this parameter provides a direct measurement of a water sample’s particle concentration.

### **1.3 Health Implications of TSS and Turbidity**

In addition to being aesthetically unappealing for human consumption, surface waters and treated water reserves with high particle concentrations can function as a nutrient-rich habitat for pathogens that, if introduced into municipal water distribution systems, can lead to widespread waterborne disease outbreaks [5]. *Cryptosporidium* and *Giardia* are two pathogens commonly detected in both surface waters and treated water



reserves with high particle concentrations and have been responsible for numerous waterborne disease outbreaks in the United States [8] [9]. In fact, water has been shown to be the facilitating medium in approximately 90% of these pathogens' outbreaks [10]. While generally not lethal to humans provided adequate medical care and nutrition, *Cryptosporidium* and *Giardia* infections can cause moderate to severe gastrointestinal illness, with symptoms including vomiting, fever, diarrhea, and headache. However, children, the elderly, and individuals with weakened immune systems (*i.e.* HIV/AIDS) can face life-threatening complications from infection.

Several studies have shown that waters with high concentrations of clay, silt, and organic and inorganic particles can provide pathogens such as *Cryptosporidium* and *Giardia* pathogens with protection against disinfecting agents intended to neutralize or limit the cultures' population growth [11] [12] [13]. While the exact mechanism for this disinfectant resistance phenomenon remains unclear, it has been hypothesized that microorganisms become attached to the larger suspended particles and thereby limit their exposure to the disinfecting agent [14]. Highly turbid waters also often contain high concentrations of algal biomass, decayed plant matter and animal remains, and human and animal wastes that can provide pathogens with a rich source of nutrients for rapid population growth. When acting in concert, these varied particle contaminants can limit the effectiveness of disinfectant treatments and often aid in the regrowth of the pathogen cultures after treatment. Fortunately, studies have demonstrated a positive correlation between the reduction of particle concentrations in surface and filtered water reserves and the removal of pathogens such as *Cryptosporidium* and *Giardia* [15].

## 1.4 Water Quality Assessment Methods

To ensure the purity of surface and filtered water reserves, government regulatory agencies, such as the Environmental Protection Agency (EPA) in the United States, have identified the most plausible water contaminant species, set their maximum legal concentrations to ensure public health, and have implemented services to routinely sample and verify a particular source's compliance with these regulations. With respect to TSS and turbidity regulations in the United States, the EPA's *Methods for Chemical Analysis of Water and Wastes* publication defines the approved measurement procedures for monitoring and reporting data for each water quality parameter [16].

### 1.4.1 Secchi Disks

Invented in 1865 as a primitive water quality measurement tool, a Secchi disk is a circular disk attached to a beam, which is then inserted into the body of water under investigation. The top face of the disk is often colored or features patterns to increase its visibility in the water to the analyst. The disk is inserted deeper into the water until the disk is no longer visible. This depth is known as the Secchi depth and is used to estimate the water's turbidity utilizing the Beer-Lambert Law [17].

The accuracy of turbidity measurements made with a Secchi disk is often limited by the photosensitivity of the analyst's eyes, the amount of ambient sunlight, and the time of day at which the measurement is taken. Furthermore, Secchi disks are generally not suitable for measuring the turbidity of fast moving waters such as rivers [18] [19]. While Secchi disks remain a popular water diagnostic tool for amateur biologists and citizen volunteers, their subjective measurements prevent them from being EPA-approved devices for turbidity and TSS monitoring and reporting.

#### 1.4.2 Nephelometers

Nephelometers are currently the only EPA approved tool for measuring a water source's turbidity (EPA Method 180.1) [16]. Nephelometers measure particle concentration in a water sample by comparing the amount of light reflected from the sample housed in an optically clear vial at a 90° angle against that of a pre-concentrated formazine standard. Nephelometers measure turbidity in units of nephelometric units (NTU), which typically range from 0-40 NTU for water diagnostic applications [2]. While EPA turbidity regulations vary with the location of the water source and its uses, the maximum allowable turbidity in surface water and treated water reserves is generally five and one NTU, respectively [20].

Though the semi-quantitative turbidity measurements made with nephelometers are superior to the qualitative measurements of Secchi disks, nephelometric analysis is not without its flaws. As nephelometers are optical devices, scratches, dirt, films, and other optical defects on sample vials can distort their measurements [2]. Samples containing bubbles or settled particulates can also introduce error. Additional care must be taken to prevent accumulation of dust particles within the device, as well as condensation in humid environments. Furthermore, nephelometers must be calibrated prior to testing to account for the intrinsic reflectivity of the particles being measured in order to obtain a meaningful turbidity measurement.

#### 1.4.3 TSS Measurement Systems

In the United States, EPA Method 160.2 is the only approved method for measuring and reporting TSS water contaminants [21]. First, a 100 mL water sample is filtered through a pre-weighed glass microfiber filter, which is then placed in an oven for

one hour at 103-105°C. If necessary, the filter is then placed in a desiccator to remove excess moisture before weighing. The filter's initial mass is subtracted from its filtered mass to determine the mass of suspended particles in the sample. The density of suspended particles is calculated by dividing the particle mass by the original sample volume. The effective TSS measurement range for this procedure ranges from 2-20,000 mg/L. Like the EPA turbidity regulations, TSS regulations also vary according to the water source location and its use, but are often in the range of 0.01 to 0.1 g/L. While EPA Method 160.2 provides an ideal quantitative measurement of a water sample's particle concentration, the additional equipment needed (oven, desiccators) to perform this procedure is too cumbersome for field-portable applications [22] [7].

## **1.5 Traditional Water Diagnostic Tools**

In recent decades, several laboratory-scale chemical analysis tools have been developed to identify a contaminant's atomic and molecular composition. While no single chemical analysis device is currently capable of detecting all of the diverse compounds that could be found in environment monitoring scenarios, several of these devices are capable of discriminating many of the commonly detected water contaminants, such as metallic, organic, and inorganic particulates. These chemical analysis devices fall into one of three categories: gas chromatographs, mass spectrometers, and plasma spectrometers.

### **1.5.1 Gas Chromatographs**

Gas chromatographs are used to identify a water contaminant's chemical structure by flowing a vaporized sample mixed into an inert flow gas through a narrow tube lined with strips of several different adsorbing materials to which the sample compounds

become imbedded, depending on their chemical properties. The rate at which these compounds exit the tube via adsorption, and the location at which this occurs, is used to identify the sample's chemical structure when coupled to a mass or plasma spectrometer.

### 1.5.2 Mass Spectrometers

Mass spectrometers are often most useful in water diagnostics for identifying a contaminant's molecular structure. Mass spectrometers first vaporize and ionize a sample's molecular constituents and then accelerate the ions in a magnetic field. The analyte's ions are deflected in a magnetic field as a function of their mass and their impact location along a sensor array can be used determine the ion's mass and chemical structure. Gas chromatograph/mass spectrometer hybrids have also been developed to achieve an even greater level of chemical species discrimination.

### 1.5.3 Plasma Spectrometers

Plasma spectrometers are generally more suitable for identifying an analyte's atomic (particularly metallic) components but can also observe simple molecular compounds. Plasma spectrometers first ionize a sample in a plasma discharge that then recombines with free electrons in the plasma to produce characteristic spectral emissions. These emissions can be measured according to their wavelength and intensity (number of photon counts per wavelength) for spectroscopic identification. For atomic samples, plasma spectroscopy offers a direct method of identification. For molecular samples however, this process provides a means of *indirect* chemical identification, as the measured spectra represent ionized fragments of the original molecule rather than the spectra of the molecule itself. Laser induced breakdown spectroscopy (LIBS) systems are an extension of the basic plasma spectroscopy concept, but utilize a high-power laser to

energize a gaseous, liquid, or solid sample, creating a plasma discharge, and observing its emission spectrum for contaminant chemical identification.

### **1.6 Miniaturized Water Diagnostic Tools**

The traditional embodiments of the devices described above however are generally not suitable for field-portable applications, due to their large size and mass, their need for high current and voltage power supplies, and vacuum and flow gas equipment. Because of these limitations, there has been considerable interest among industrial and academic researchers to develop miniaturized embodiments of these devices for a variety of applications, including water diagnostics. In general, the design complexity inherent to gas chromatographs and mass spectrometers make them less amenable to miniaturization, compared with the relatively simpler components needed to construct a plasma spectroscopic device.

Several miniaturized plasma spectroscopic devices have been reported for the detection of atomic and molecular impurities. In one report, a gaseous sample was pumped into a Teflon tube where a large, pulsed DC bias was applied between two electrodes in a He ambient. The sample was ionized in the plasma discharge and its spectral emissions were measured with an off-chip spectrometer [23]. However, this device's analysis was limited to gaseous samples and the helium ambient must be replenished after each test, requiring the transportation of large gas tanks for field-portable applications. Molecular emission detectors utilizing on-chip DC microplasmas within microfluidic channels have also been developed [24] [25] [26] [27]. These devices pumped gaseous samples mixed with an inert flow gas into a microfluidic chamber where an on-chip microplasma provided atomic and molecular spectra by

excitation. Versions operating at low-pressure and atmospheric pressure were reported. In the former, the microplasma chip was coupled with an off-chip, traditional gas chromatograph for spectral analysis and required additional vacuum equipment for low-pressure operation. The latter used an off-chip monochromator and photomultiplier tube.

Research on direct-current (DC) nitrogen microplasmas has supported the development of microelectromechanical systems (MEMS) that perform plasma spectroscopic analysis in air at atmospheric pressure [28] [29]. A plasma spectroscopic-based liquid electrode spectral emission chip (LEd-SpEC) operating in air and at atmospheric pressure has been reported for detecting metallic water impurities [30]. Impurities in the liquid water cathode were sputtered into an on-chip DC microplasma and detected with an off-chip spectrometer. However, the lifetime of the polyimide channels used as reservoirs for the liquid electrodes was found to be limited, reducing the device's overall useful lifetime [31]. This particular report is notable among other efforts towards development of miniaturized plasma spectroscopic devices as the authors attempted to measure a water contaminant's concentration by comparing the spectral line intensity ratios of the contaminant against that of an ambient background gas. However, this technique remains an indirect concentration measurement with limited results.

Development of plasma spectroscopic detectors which utilize magnetically confined plasma discharges have been shown to reduce the average energy of electrons in the plasma glow region, thereby providing a potential method of exciting a molecular compound to produce characteristic emission spectra without fragmentation [32]. In one report, a niobium powder and epoxy mixture was cast in a Teflon mold to fabricate hollow cathode structures that achieved plasma spectral intensities an order of magnitude

greater than previous microplasma-based devices. The large vacuum equipment needed to realize these results, however, are not ideal for field-portable devices.

The use of partially evaporated water samples, or slurries, in inductively coupled plasma (ICP) spectroscopic devices has been shown to reduce contaminant detection limits [33] [34]. The improved detection limits are primarily attributed to the higher contaminant concentration in the vapor released from the slurried sample but are supported by reduced transport effects from decreasing the distance traveled by the sample vapor to the excitation source. “Dry” samples are often preferred over liquid samples for microplasma spectroscopy systems where large liquid samples may extinguish the plasma [35]. In these devices, water samples are inserted into a dimple pressed into a metal foil or a coiled metal filament and vaporized by applying a voltage to the foil or filament. The vaporized sample is delivered to a plasma discharge by a flow gas and the spectral emissions are observed. However, the large size of these devices, their flow gas and laboratory-scale power supply requirements are too cumbersome for on-site environmental monitoring applications.

While all of the research efforts reported above have made significant progress towards developing miniaturized and field portable diagnostic tools, all but one report has focused exclusively on identifying a contaminant’s chemical structure. What is needed is a miniaturized system that identifies both chemical composition *and* concentration.

## **1.7 Dissertation Objectives**

The primary objective of this dissertation is the development a miniaturized diagnostic device that is capable of performing a complete on-site water quality analysis that includes an evaluation of a pollutant’s chemical composition and concentration. This



functionality will be achieved through a two-phase electrochemical analysis process performed by MEMS-scale plasma spectroscopic and capacitance-based sensing platforms. To enhance the finalized water diagnostic system's sensitivity, both sensing platforms will also exploit a water sample preconcentration stage in which the liquid water sample is converted into a dry and porous contaminant particle film. In this arrangement, the isolated contaminant particles will yield more robust emission spectra, enabling a more sensitive spectroscopic analysis of the contaminant's chemical structure, and the isolated contaminant particles' dielectric properties can be measured with greater precision in the absence of the high-permittivity water solution, enabling a more precise measurement of the impurity's concentration in conjunction with a numerical capacitance-to-concentration model.

Initially, each sensing platform will be developed separately to investigate the optimal design, fabrication process, and analysis procedure for each device. A numerical concentration-to-capacitance model will also be derived in conjunction with the development of the capacitive sensing prototype to interpret its output. This numerical model will incorporate physical parameters of the specific contaminant under investigation and the capacitance device's analysis chamber to estimate the porous contaminant film's capacitance with maximum accuracy. Finally, each sensing platform will be integrated onto a single substrate and incorporate design revisions uncovered in their respective development efforts. The integrated diagnostic system's analytical capabilities will then be evaluated with powdered materials representing common suspended and dissolved water contaminant species at multiple concentrations comparable to EPA regulation limits.

An overview of the integrated water diagnostic system's two-phase capacitive/plasma spectroscopic analysis procedure is illustrated in **Figure 1-1**.

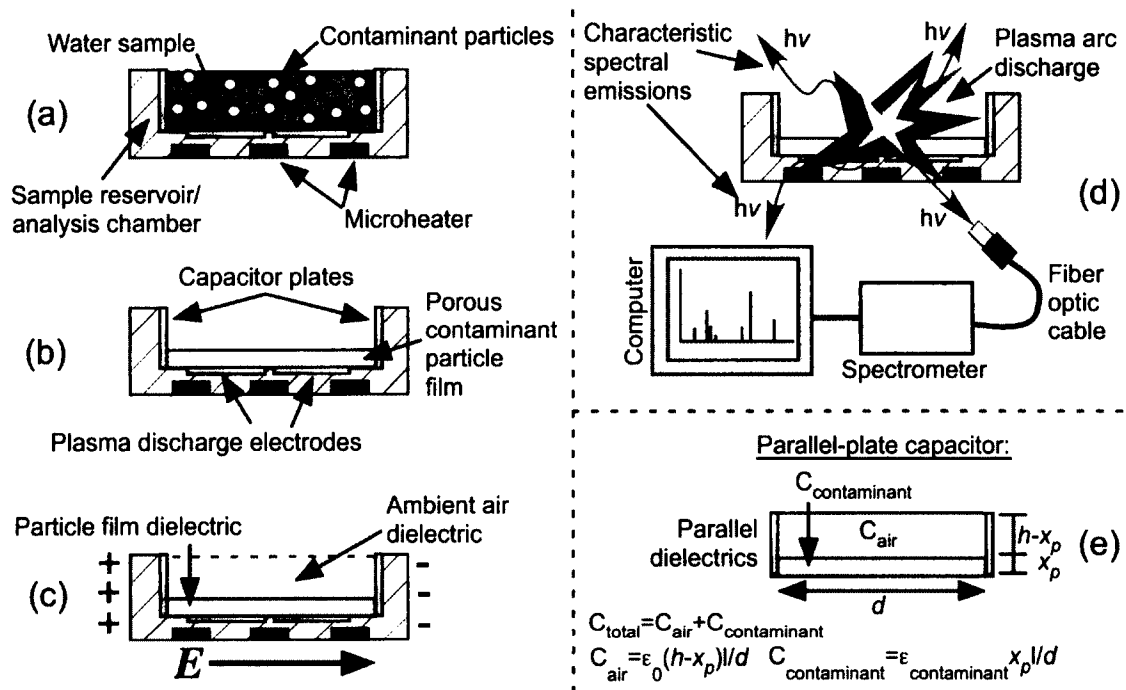


**Figure 1-1:** Overview of the capacitive/spectroscopic analysis procedure.

First, a water sample is injected into a dual-purpose sample reservoir and analysis chamber that contains the plasma spectroscopic and capacitive sensing elements (**Figure 1-1a**). Here, two opposing walls of the rectangular analysis chamber are patterned with metal to serve as the plate electrodes of a parallel-plate capacitor and metal filaments are embedded in a microchannel etched in the chamber base to serve as plasma discharge electrodes. The water sample is then preconcentrated as a porous contaminant particle film via evaporation by applying current to an on-chip thin film microheater (**Figure 1-1b**). Next, the total capacitance of the sample reservoir/analysis chamber, including the contaminant film and ambient air filling the remainder of the chamber volume and interparticle voids, is recorded with an off-chip capacitance measurement board to

preserve the contaminant film's original dielectric properties for a detailed concentration analysis with the numerical model in a later step (**Figure 1-1c**).

A high-voltage DC bias is then applied to the plasma discharge electrodes to ionize particles in the contaminant film. Electron transitions in atomic and molecular contaminant ions result in the release of characteristic emission spectra from which the impurity can be identified with an off-chip spectrometer (**Figure 1-1d**). With the impurity's chemical composition now known, its relative permittivity, density, and bulk density parameters can be utilized in the numerical concentration model to separate the capacitance of the contaminant particle film from that of the ambient air by modeling the analysis chamber's total capacitance as two parallel-connected rectangular dielectrics, representing the capacitance contribution of the contaminant film and ambient air. The numerical model is also derived to estimate the volume fractions of the contaminant material and air voids in the porous film in order to calculate the film's effective permittivity. Finally, the numerical model's estimates of the contaminant film's isolated capacitance as a function of concentration can be compared with capacitance data recorded experimentally with the device (**Figure 1-1e**).

Contaminant materials investigated in this work were selected to represent dissolved and suspended-type water contaminants that could contribute to the incubation and spread of waterborne pathogens such as *Cryptosporidium* and *Giardia*, including  $\text{Al}_2\text{O}_3$ ,  $\text{CaCO}_3$ ,  $\text{CuO}$ ,  $\text{FeO}$ ,  $\text{MgO}$ ,  $\text{NaCl}$  and  $\text{SiO}_2$  compounds. As water contaminants, these materials could plausibly originate from environmental sources, such as the erosion of rocky soil and mineral deposits by flooding, or man-made sources, such as industrial wastewater discharges, the corrosion of plumbing systems, or land development.

$\text{Al}_2\text{O}_3$ ,  $\text{CaCO}_3$ ,  $\text{MgO}$ , and  $\text{SiO}_2$  were selected to represent contaminants commonly found in nature from rock and mineral sources.  $\text{CaCO}_3$  and  $\text{MgO}$  impurities are also the primary components of hard water.  $\text{CuO}$  and  $\text{FeO}$  are common industrial pollutants and can also result from the corrosion of piping and plumbing fixtures [1].  $\text{NaCl}$  contaminants were investigated to characterize the salinity of a water source, where salt concentrations vary up to approximately five percent.

## **1.8 Organization of this Dissertation**

Chapter Two will briefly review the physical principles on which development of the plasma spectroscopic platform will be based, including plasma physics, the physics of light and matter interactions, and the identification of atomic and molecular compounds by the plasma emission spectroscopy technique.

Chapter Three will discuss the design, fabrication, and testing of two first generation prototypes of the plasma spectroscopic sensing platform. Two configurations of a combined thin film plasma electrode microheater circuit will be explored as a water sample preconcentration and excitation element.  $\text{Al}_2\text{O}_3$ ,  $\text{CaCO}_3$ ,  $\text{CuO}$ ,  $\text{FeO}$ ,  $\text{MgO}$ , and  $\text{NaCl}$  water contaminants will be analyzed with prototypes fabricated using both preconcentration circuit designs at three concentration levels.

Chapter Four will briefly review the relevant electromagnetic principles necessary for the development of the capacitive sensing platform, including basic capacitor physics and circuits. This chapter will also discuss the leading theoretical models for simulating the dielectric properties of composite materials, which will be an integral component in the development of the mathematical contaminant concentration-to-capacitance model.

Chapter Five will discuss the design, fabrication, and testing of the first generation capacitive sensing prototype. This prototype will feature a mechanism to vary the plate separation distance in order to investigate the compromise between analysis chamber and sample size volume and the range of the sensor's capacitive output for an optimal signal-to-noise ratio. This chapter will also describe the application of the composite dielectric models discussed in Chapter Four toward the development of preliminary water contaminant concentration-to-capacitance models representing water samples containing single and multiple contaminant species.  $\text{Al}_2\text{O}_3$ ,  $\text{SiO}_2$ , and  $\text{NaCl}$  water contaminants will be investigated singly at five concentration levels to characterize the single contaminant concentration model and in four mixture ratios at three concentration levels to characterize the multi-contaminant concentration model.

Finally, Chapter Six will discuss the design, fabrication, and testing of an integrated water diagnostic system that incorporates revised embodiments of the plasma spectroscopic and capacitive sensing platforms as a single system. This chapter will also describe modifications made to the original plasma spectroscopic and capacitive analysis procedures, as well as the single contaminant concentration-to-capacitance model, to improve contaminant detection sensitivity and accuracy. The integrated water diagnostic system will then be used to evaluate the chemical composition and concentration of  $\text{MgO}$ ,  $\text{CaCO}_3$ , and  $\text{NaCl}$  contaminants at six concentration levels.

## **CHAPTER 2**

### **PLASMA SPECTROSCOPY PRINCIPLES**

This chapter briefly describes the physical principles governing chemical analysis by plasma spectroscopy and provides a theoretical basis for interpreting spectral data generated by the plasma spectroscopic sensor prototypes in later chapters.

Chemical analysis by plasma spectroscopy presents several attractive features toward the development of a miniaturized water diagnostic system. First, comprehensive emission spectral data is documented for essentially any water contaminant likely to be encountered in an environmental testing scenario and contaminant spectra can be recorded with one of the many miniaturized spectrometers commercially available at relatively low cost. Second, compact DC plasma sources utilized to provide excitation energy to a contaminant particle to stimulate spectral emissions can be purchased cheaply or constructed from a few simple and inexpensive components (see Section 6.6). Finally, the spectroscopic analysis can be performed in air and at atmospheric pressure, if a compromise between signal-to-noise ratio and device size can be accommodated.

#### **2.1 Plasma Physics**

All gases are composed of electrically neutral particles (atoms and molecules) and charged particles (ions and free electrons) [36]. The distinction between an ordinary gas and plasma lies in the proportion of neutral particles to charged particles. While an

ordinary gas is composed almost exclusively of neutral particles, plasmas are composed of a substantial but approximately equal number of charged particles. Plasmas exhibit high electrical conductivity and can be influenced by external electromagnetic forces due to the high density of charged particles. In this regard, the properties of plasma are sufficiently different from those the three classical states of ordinary matter (solids, liquids, and gases) for plasma to be considered a fourth state of matter.

It is helpful to first consider the behavior of plasma as a special case of an ordinary ideal gas, as shown in **Figure 2-1**. Here, the gas particles are assumed to be point particles whose size is negligible compared to the average interparticle distance and the volume of the gas and move in straight lines in random directions (**Figure 2-1a**). In the absence of an external electric field, the vast majority of gas particles remains neutral and only occasionally collides elastically with each other.

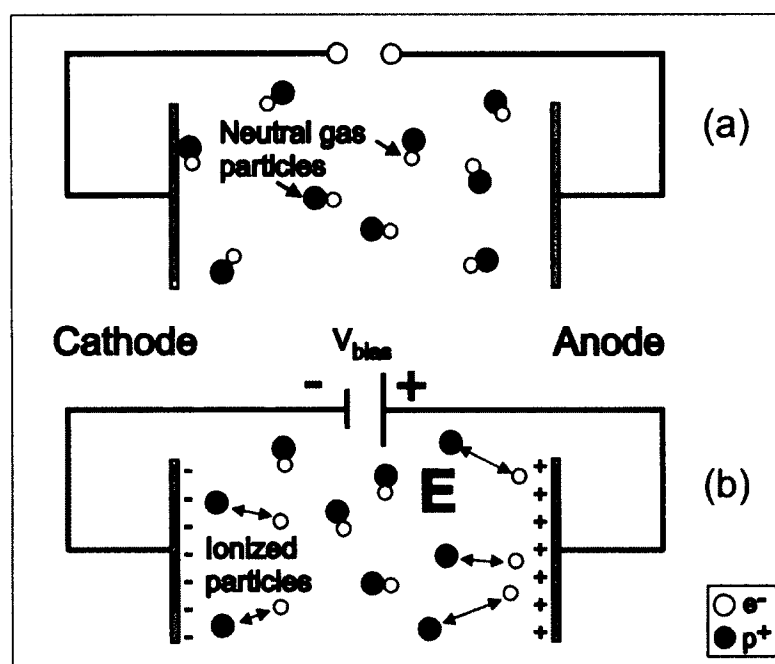


**Figure 2-1:** Plasma behavior modeled with a simple monatomic gas.

However, if a sufficiently strong electric field is applied across the gas, the charged particle density will increase and approach that of the neutral particles (**Figure 2-1b**). The gas can properly be called a plasma when the charged particle density alters the physical behavior of the gas, such as being influenced by a magnetic field or conducting electrical current. This transition occurs due to the electron “avalanche effect,” where a free electron is accelerated by the applied electric field and collides with a neutral particle in an inelastic (or ionizing) collision, creating an ion and a new free electron. This new electron is also accelerated by the electric field, resulting in new inelastic collisions with other neutral particles, and so on, until the charged particle density is comparable to the plasma’s total particle population. In this work, ionizing collisions by accelerated electrons provide the excitation energy needed to stimulate contaminant particle electron transitions, which release spectral lines through which the contaminant can be identified.

## 2.2 Emission Spectroscopy Physics

Consider a contaminant particle film that rests between two metal plasma discharge electrodes in air at atmospheric pressure. A high voltage DC applied between the electrodes instigates the electron avalanche effect, creating a plasma discharge where contaminant particles are ionized by accelerated electrons. The ionized contaminant particles may eventually recombine with other free electrons in the plasma (whose velocities are lower than that of the ionizing electrons) to form neutral particles once again. It is also possible for the ions to remain in a charged state (*i.e.* unequal quantities of protons and electrons), provided no recombination events occur.



In either case, electrons bound to the contaminant particle (neutral or ionized) can only occupy discrete energy levels, which are dependent on the particle's nuclear structure. If the contaminant particle absorbs energy during a collision with a free electron in the plasma, its bound electrons can transition to a discrete excited energy level, provided the level is not already occupied by another electron. If the excited electron then transitions from the excited energy level to a lower energy level, the difference in energy lost by the electron during this transition can be emitted from the particle as a photon according to:

$$E_2 - E_1 = \Delta E_{21} = h\nu_{21} \quad \text{Eq. 2-1}$$

where  $E_2$  and  $E_1$  are the energy (J) of the electron in its excited and lower energy states, respectively,  $h$  is Planck's constant ( $6.626 \times 10^{-34}$  J·s),  $\nu_{21}$  is the transitioning photon's frequency ( $\text{s}^{-1}$ ), and  $c$  is the speed of light in a vacuum ( $2.998 \cdot 10^8 \text{ m}\cdot\text{s}^{-1}$ ) [37]. For the spectroscopic analysis purposes used in this work, photons are measured by their wavelength  $\lambda$  (nm), according to:

$$\lambda = \frac{c}{\nu} \quad \text{Eq. 2-2}$$

Simple atoms (such as Ca or Na) and relatively complex molecules (such as CaO or MgOH) have numerous energy levels through which a bound electron can transition between, resulting in the emission of photons. In this work, an on-chip plasma discharge provides the excitation mechanism needed to ionize particles in the porous contaminant film and stimulate photon-emitting transitions between energy levels in electrons bound to the particles, as illustrated schematically in **Figure 2-2**. The wavelengths (or “colors”) of light that can be emitted from a given particle are diverse but also specific to the

particular type of contaminant particle that emits the photon. For example, the spectral lines that could be emitted by electrons transitioning in a Na atom will be distinct from those of a Mg atom or a CaO molecule. This concept forms the basis for the spectroscopic identification of a contaminant's chemical structure used in this work.

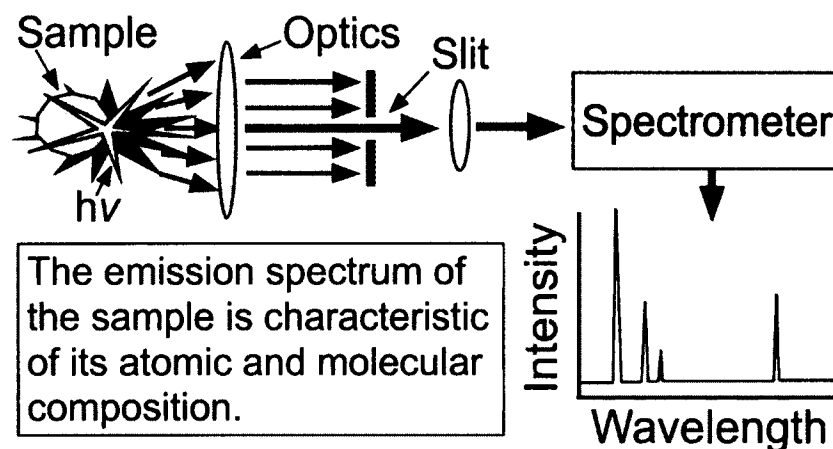


**Figure 2-2:** Overview of plasma emission spectroscopy procedure.

As a practical matter for this work, all wavelengths of light that can be emitted by a given contaminant particle in the porous film when excited by a plasma discharge could be observed in a single spectroscopic analysis (provided certain experimental conditions are satisfactorily met) due to the vast number of contaminant particles in the film. When represented collectively in graphical form, this data can be used as the contaminant's spectral "fingerprint" by which it can be identified. The diversity of spectral lines from a single contaminant species is illustrated in **Figure 2-3**, showing the emission spectrum of a Hg calibration source between 200 and 800 nm. The wavelength (or frequency or wavenumber) of a photon is represented on the x-axis and the units of the y-axis represent the intensity of the spectrum, here in terms of photon counts per unit wavelength. The intensity at which spectral lines are observed will again depend on the

contaminant's nuclear structure, but will also be limited by the design of the spectrometer and fiber optics used to collect the spectra and the orientation of the fiber's aperture with respect to the plasma discharge [38,26,26].

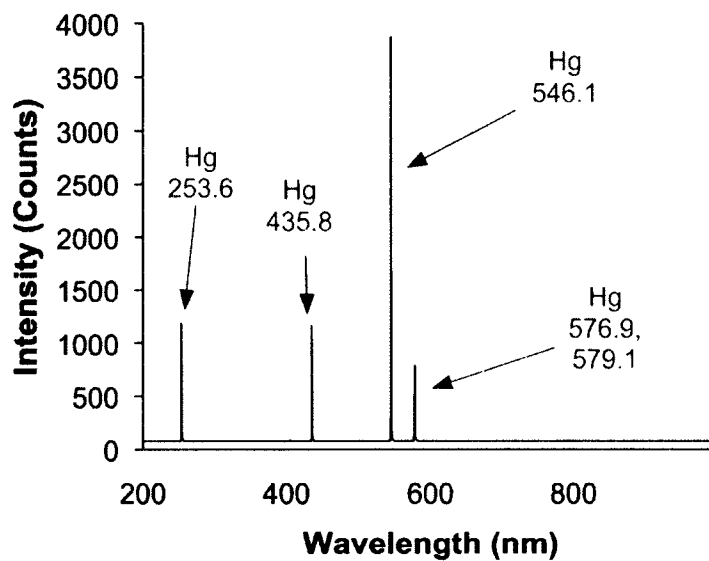


**Figure 2-3:** Sample emission spectrum of Hg.

## **CHAPTER 3**

### **PLASMA SPECTROSCOPIC SENSING PLATFORM**

#### **3.1 Research Objectives**

This chapter discusses the design, fabrication, and testing of two first generation prototypes of the plasma spectroscopic sensing platform<sup>1</sup>. Within the integrated water diagnostic device, this sensing platform will be utilized to spectroscopically identify a water contaminant's chemical composition. An updated embodiment of this device, based on performance and experimental procedure issues uncovered during this initial development stage, will then be incorporated into the final integrated water diagnostic system discussed in Chapter 6.

Three major objectives governed the development of the plasma spectroscopic sensing platform, including:

- (1) Investigation of a water sample preconcentration stage to streamline the spectroscopic analysis and prepare the sample for a capacitance-based contaminant concentration analysis in a later step (see Sections 5.3, 6.3, and 6.4);
- (2) Minimization of the device's mass, volume, and external hardware requirements to promote field portability; and

---

<sup>1</sup> Portions of this work were published in conference form in [68,67].

- (3) Development of an essentially disposable construction that favors inexpensive materials and batch fabrication techniques, where possible.

### 3.2 Design Considerations

To support the field portability of the final integrated diagnostic system, the plasma spectroscopic sensing platform was designed to operate in an air ambient at atmospheric pressure. This arrangement provided two significant benefits. First, the plasma spectroscopic sensor could utilize a simpler design with fewer on-chip components suitable for simple microfabrication processes. In-air operation eliminates the need to fabricate intricate microchannel networks to deliver and mix an inert plasma flow gas with contaminant particles, as well as hermetic sealing requirements, which are both commonly reported features in analytical microdevice literature. Secondly, atmospheric pressure operation eliminates the need for cumbersome external vacuum hardware and allows the sensor to be constructed from less rigid and more easily machined materials, as the sensor's structure will not experience the low pressure induced stresses common to vacuum operated devices.

It should be noted that performing the spectroscopic analysis in air and at atmospheric pressure could be expected to increase spectral "noise" in the form of emission lines from ionized air molecules, particularly N and O-based compounds. However, contaminants commonly monitored in water diagnostic applications generally have distinct and robust spectral lines that do not overlap with air background lines. Overall, this arrangement will support development of a simpler, field portable, and inexpensive embodiment of the final integrated water diagnostic system.

### 3.3 Plasma Spectroscopic Sensor Design

In previous work, an optical microdevice (LEd-SpEC) was developed to spectroscopically detect metallic water impurities sputtered from a liquid water sample cathode electrode into an on-chip microplasma discharge [30] [39]. Fabrication of the LEd-SpEC device required a relatively complex four-mask photolithography process and utilized polyimide microchannels to transport the water sample from a sample reservoir to a plasma discharge site. However, the polyimide structures proved to not be as robust or unreactive as desired for sensing applications, leading to polyimide contamination issues and a limited device lifetime [31].

The plasma spectroscopic platform developed here improves on the LEd-SpEC device by introducing a water sample preconcentration stage prior to plasma excitation and spectroscopic analysis. Here, the liquid water sample is converted into a dry and porous contaminant film by evaporating the water solution with an on-chip heating element. This arrangement improves the plasma spectroscopic analysis in three meaningful ways. First, the high concentration of contaminant particles in the residual film ensures the contaminant's spectral signature will be observed with maximum intensity. Second, by eliminating the liquid water solution and its spectral signature, the contaminant's spectral lines will be easier to distinguish against that of the air background. Finally, the dry particle film will be unlikely to extinguish the plasma discharge during the spectroscopic analysis, as often occurs with spectroscopic devices utilizing liquid samples. Fabrication of this device also improves on the LEd-SpEC device by requiring fewer photolithography steps (one mask versus four) and utilizing more robust and non-reactive materials (glass and ceramic versus polyimide).

### 3.3.1 Sample Preconcentration Overview

Conventional laboratory-scale inductively coupled plasma atomic emission spectrometers (ICP-AES) utilize a nebulizing mechanism to convert liquid samples to a fine mist that is then sprayed into a macroscale plasma discharge to ionize and excite the analyte particles. Spectral lines emitted by the analytes are measured spectroscopically to identify the analyte's chemical composition. In this setup, distinguishing the spectral signature of the analyte from that of its solution can be problematic, particularly for samples with low analyte concentrations.

Efforts to enhance the detection sensitivity of traditional ICP-AES systems have explored vaporization of liquid and solid samples prior to spectroscopic analysis to increase plasma analyte density [34]. ICP-AES systems utilizing in-torch vaporization (ITV) mechanisms house a sample in a hollow probe containing a coiled metal filament. Electrical current is applied to the filament to heat the sample, resulting in a dense analyte vapor. For solid samples, the coiled filament heats the sample until vaporization by charring. For liquid samples, this "preconcentration" stage can be used to separate the analyte from its solution before vaporizing the analyte residue. In both cases, the analyte dense vapor is mixed with an inert carrier gas prior to plasma spectroscopic analysis. The higher analyte concentration within the vapor generally increases its spectral intensity, allowing greater detection sensitivity. The path from the ITV probe to the plasma discharge is also minimized to reduce transport effects, such as the loss of analyte particles via adsorption to chamber walls.

Applications of this ITV-based preconcentration concept to microdevices have been limited. In one report, a separate macroscale ITV apparatus based on work in [33]

and [34] was coupled to a microchannel device for spectral detection of Na analytes by an on-chip microplasma discharge [35]. Here, microplasma devices were under investigation to optimize the spectroscopic analysis by reducing the flow rate of costly inert gases used in traditional ICP-AES systems. The high density analyte vapor generated by the off-chip ITV apparatus was then guided through microfluidic channels within the microdevice via a He flow gas towards a microplasma excitation region. Introduction of the analyte into the microplasma as a vapor was also shown to prevent the extinction of the plasma discharge, in contrast to microplasmas coupled with traditional liquid sample nebulizers.

### 3.3.2 Water Sample Contaminant Preconcentration

The plasma spectroscopic platform reported here capitalizes on the ITV preconcentration concept in two ways. First, rather than utilizing an off-chip ITV-type mechanism, water samples are preconcentrated on-chip by a thin film microheater patterned to the base of a sample reservoir. Plasma discharge electrodes integrated within the microheater allow in-situ spectroscopic analysis of the preconcentrated water sample residue, effectively eliminating the loss of analyte particles by transport effects as well as flow gas requirements. This arrangement also allows the overall size of the analytical system to be significantly reduced compared to ITV-based systems.

Secondly, the preconcentration stage prepares the water sample for a capacitance-based contaminant concentration analysis, to be developed in a later step (see Section 5.3). Here, the preconcentration stage isolates and arranges the contaminant particles as a thin porous film of uniform dimensions and density, such that the particle film now resembles a rectangular parallel-plate capacitor's dielectric material. Removal of the



high-dielectric water solution also allows a more sensitive measurement of the residual contaminant particles' capacitance, which generally have substantially lower permittivities than water. This concentration-to-capacitance analysis is discussed more thoroughly in Sections 5.4, 6.3, and 6.4.

### 3.3.3 Plasma Spectroscopic Analysis

First generation prototypes of the plasma spectroscopic sensing platform are used to identify a water contaminant's chemical composition in a three-step analysis, as illustrated in **Figure 3-1**.

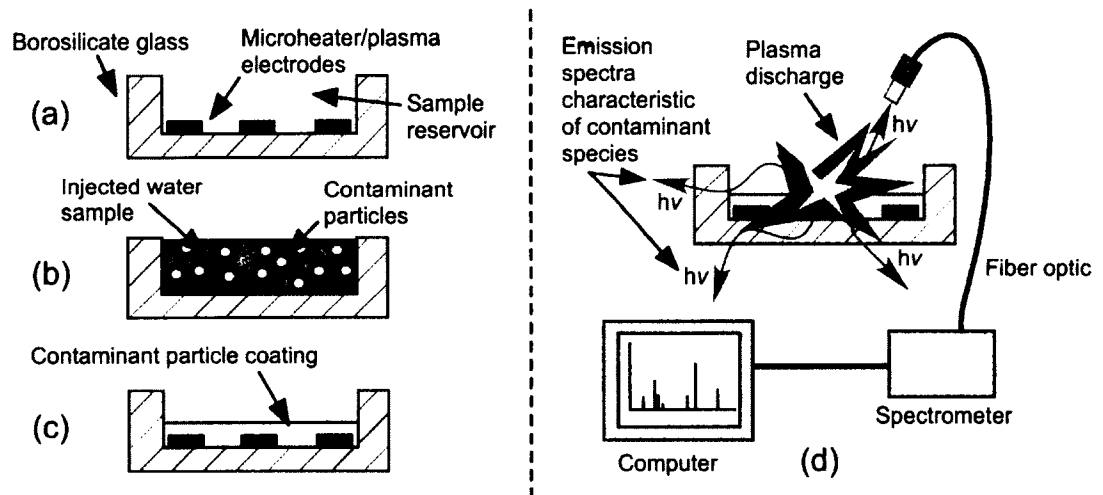


**Figure 3-1:** Plasma spectroscopic analysis procedure.

Spectroscopic analysis is performed in a combined water sample reservoir and capacitive analysis chamber, where an integrated microheater and plasma discharge electrode circuit is patterned to a thin metal film deposited to the base of the reservoir (**Figure 3-1a**). A 100  $\mu\text{L}$  water sample is then injected into the sample reservoir (**Figure 3-1b**) and preconcentrated via evaporation into a porous contaminant particle film of uniform height and density by applying current to the microheater circuit from an off-chip current source (**Figure 3-1c**).

Next, a DC bias voltage (ranging from two to three kV) is applied to the discharge electrodes to create a plasma discharge within the reservoir (**Figure 3-1d**). Contaminant particles in the preconcentrated film are sputtered into the discharge and ionized into atomic and molecular fragments. Light emitted from the plasma discharge is the result of electronic transitions in atomic and molecular ions from the air and contaminant particles. Each ionic species emits light at specific wavelengths that are characteristic of the emitting species. Emission spectra are collected and processed with an off-chip spectrometer and laptop computer where contaminant lines are detected by comparing prerecorded background and contaminant spectral data. The contaminant is identified by comparing the wavelength and relative line intensity of its spectral lines against known spectral data documented in atomic [40] and molecular [41] reference texts.

### 3.4 Device Fabrication

Spectroscopic sensor prototypes were fabricated from borosilicate glass and glass-mica ceramic substrates with Cr serving as the microheater/electrode circuit material. Cr is a suitable material for thin film electrode and heating elements due to its general chemical and mechanical robustness, adhesion to a variety of substrate materials, and suitability for photolithographic patterning. Borosilicate glass and glass-mica ceramic materials are electrically insulating, easily machined, mechanically robust, and bond well with Cr films without an adhesion layer. Borosilicate glass, however, proved to be a better overall substrate material due to its significantly lower cost.

Two mask patterns for the plasma spectroscopic sensor's combined microheater and plasma discharge electrode circuit were explored for this work, labeled pattern A and pattern B circuits, as shown in **Figure 3-2**. MEMS devices requiring on-chip heating

elements often capitalize on thin film-based structures for their low profile and amenability to simple photolithographic batch fabrication methods [42]. By consolidating the plasma discharge electrodes and microheater element into a single thin film structure, fabrication of the sample preconcentration and spectroscopic analysis circuitry could be reduced to a single-mask process with standard photolithography techniques.

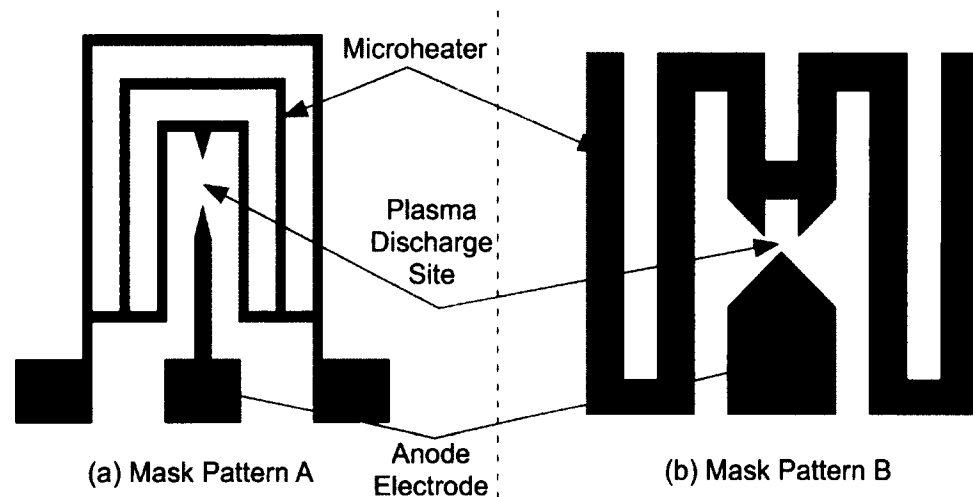


**Figure 3-2:** Microheater/electrode mask patterns used for the first generation device.

Prototypes fabricated from borosilicate glass substrates utilized the pattern A circuit design (**Figure 3-2a**), which featured three thin parallel-connected heater coils, where the innermost coil included a point at its center to serve as the plasma discharge cathode terminal. Ceramic-based prototypes utilized the pattern B circuit design (**Figure 3-2b**), which featured a single, wide heater coil and two cathode terminals to increase device lifetime against the erosion of the terminal material by sputtering after repeated plasma discharge/spectroscopic testing cycles.

The first generation spectroscopic platform's three-step fabrication process is illustrated in **Figure 3-3**, for both pattern A and B circuit designs. The prototype's structure comprised two layers that were machined and patterned with their respective

components separately before being stacked and bonded. Each 50.8 mm × 50.8 mm × 3.175 mm substrate was first thoroughly cleaned in 90% isopropyl alcohol and acetone baths and dried with compressed nitrogen and hotplate heating for ten minutes at 250 °C. This step insured any residual dirt or oil impurities on the substrate surface were removed to maximize adhesion of the Cr thin film and epoxy binder/sealant.

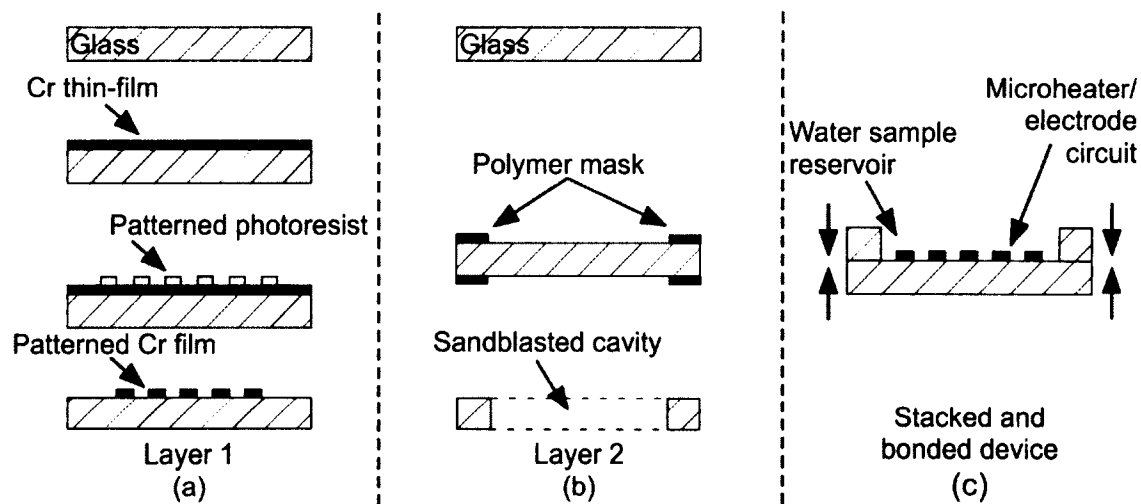


**Figure 3-3:** Fabrication process for the first generation plasma spectroscopic sensor.

The first substrate layer contained the microheater and plasma electrode circuit (**Figure 3-3a**). Cr films were deposited to the entire substrate surface by electron beam sputtering. Devices fabricated from borosilicate glass substrates utilized the pattern A (**Figure 3-2a**) microheater/electrode circuit with 200 nm films while glass-mica-based devices utilized the pattern B (**Figure 3-2b**) microheater/electrode circuit with 100 and 50 nm films. Patterning the microheater/electrode circuit began by first depositing S1813 photoresist to the Cr film and spinning at 2250 rpm for 45 seconds to form a uniform one  $\mu\text{m}$  photoresist film. The photoresist film was then annealed (soft baked) at 90 °C for 180 seconds and allowed to cool to room temperature before exposure with the appropriate

mask pattern under a UV lamp for 150 seconds. Each mask featured a matrix of microheater/electrode circuit patterns to batch fabricate multiple devices per substrate in a single lithography run. The exposed photoresist was annealed again (hard baked) at 110 °C for 150 seconds before developing in an MF319 developer bath. The substrate was then placed in a Cr etchant bath to pattern the microheater/electrode features.

Electrical feed-through channels were machined into each substrate by drilling to provide a uniform diameter power conduit to the microheater/electrode circuit. However, drilling often induces significant frictional heat stresses that can fracture the substrate. To prevent fracture, the electrical conduit channels were etched in a two-part process, consisting of sandblasting and drilling steps. First, a polymer mask was patterned to the top and bottom side of each substrate to define the electrical feed-through channel aperture over the electrode pads. Next, a pilot channel for each conduit was etched by sandblasting each side of the substrate. Finally, the conduit channels were machined with a 1 mm diamond carbide bit and a drill press to a uniform diameter. Wiring was then inserted into the feed-through channel and connected to the cathode and anode pads. While soldering provides a better electrical connection, the focused heat often damages thin films. For this application, applying a two-part Ag solder paste and curing on a hotplate provided a reliable electrical connection without damaging the thin film.

The second device layer consisted solely of a square cavity to function as the water sample reservoir when bonded on top of the first device layer (**Figure 3-3c**). An array of 12 mm × 12 mm sample reservoir cavities were etched into each substrate by patterning a polymer mask on the substrate surface to define the reservoir cavity dimensions and sandblasting. The two device layers were then stacked with the

microheater/electrode circuit centered in the reservoir base, bonded, and water sealed with epoxy. A finalized array of devices, fabricated with each substrate material and microheater/electrode pattern, is shown in **Figure 3-4**. The area of the microheater coil region in the Pattern A circuit is  $9 \text{ mm}^2$  ( $3 \text{ mm} \times 3 \text{ mm}$ ), where each coil is  $600 \mu\text{m}$  wide and the cathode and anode terminals are separated by  $400 \mu\text{m}$  at the plasma discharge site (**Figure 3-4a**). The area of the cathode and anode electrode pads is  $3.375 \text{ mm}^2$  ( $1.5 \text{ mm} \times 2.25 \text{ mm}$ ) and the entire pattern's area is  $99.75 \text{ mm}^2$  ( $9.5 \text{ mm} \times 10.5 \text{ mm}$ ). For the Pattern B circuit, the total circuit area is  $115.5 \text{ mm}^2$  ( $10.5 \text{ mm} \times 11.0 \text{ mm}$ ), where the single heater coil is  $1.5 \text{ mm}$  wide and the twin cathode terminals are separated from the anode terminal by  $200 \mu\text{m}$  (**Figure 3-4b**). The anode electrode pad is  $9 \text{ mm}^2$  ( $3 \text{ mm} \times 3 \text{ mm}$ ). The material cost for the glass-based device with the Pattern A circuit was estimated to be approximately \$8 USD per unit while the ceramic-based device with the Pattern B circuitry was estimated to be approximately \$80 per unit, due to the high cost of the ceramic substrate material.

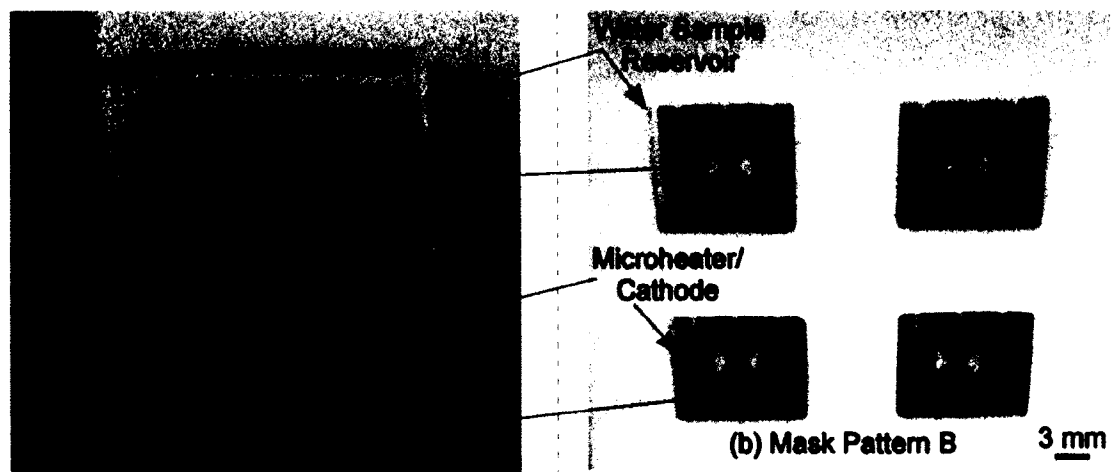


**Figure 3-4:** Finalized plasma spectroscopic prototypes for each mask pattern.

### 3.5 Experimental Setup

All spectra were recorded in a dark and light-sealed room with an Ocean Optics HR2000 UV/VIS spectrometer (200-1100 nm bandwidth) [43] [44], a laptop computer, and Ocean Optics' SpectraSuite software. Spectra were collected with Ocean Optics' laboratory-grade 50-micron (P50-2-UV-VIS) and 1000 micron (P1000-2-VIS-NIR) fiber optic cables, which both feature a 300-1100 nm peak bandwidth. The 1000 micron fiber was preferred for measuring contaminants whose fragments emit weaker spectral lines, such as Cu in CuO and AlO from Al<sub>2</sub>O<sub>3</sub>, while the 50 micron fiber was favored for contaminants with more robust fragment spectral lines, such as Mg<sup>+</sup> in MgO and Fe in FeO. Two commercial power supplies were used to power the microheater/electrode circuit, including a 5A current source to power the microheater circuit for sample preconcentration and a high-voltage (0-3.5 kV) power supply to provide the plasma discharge bias voltage.

A "dark" spectrum of the entire measurement system was recorded before testing began and subtracted from all spectral data. The fiber optic cables were oriented over the device's plasma discharge site in multiple configurations, varying the measurement angle and separation distance (approximately 1 to 5 mm) to maximize the contaminant's spectral line intensity. A spectrum of the ambient air background was recorded at the beginning of each testing session to establish a reference spectrum which all contaminant spectral data would be compared against to distinguish contaminant-exclusive lines.

Two recurring sampling issues were excessive background spectral noise and the inconsistent capture of weak and short-lived contaminant lines. To minimize background noise, each spectrum was recorded with an integration time of 300 ms. To ensure weaker

and shorter persistence lines were recorded, multiple spectra samples were collected during each contaminant test by utilizing SpectraSuite's high-speed acquisition mode with an acquisition interval of five seconds. Previously, spectra were recorded individually as instantaneous "snapshots" when a contaminant line was observed, leading to many contaminant lines not being recorded due to poor timing and coordination between the user and the software. The high-speed acquisition mode simplified the spectral collection process by allowing multiple spectra samples to be recorded during a test and replayed as a "film." When a potential contaminant line was observed during replay, the spectral film could be paused to capture and more closely examine the line.

### 3.6 Results

$\text{Al}_2\text{O}_3$ ,  $\text{CaCO}_3$ ,  $\text{CuO}$ ,  $\text{FeO}$ ,  $\text{MgO}$ , and  $\text{NaCl}$  contaminants were investigated to characterize the spectroscopic sensor's performance. Solutions for each contaminant were prepared by mixing high-purity contaminant powders in distilled water at concentrations of 100, 10, and 1 parts-per-million (ppm). Contaminants were analyzed in two testing sessions using sensor prototypes fabricated with one of the two microheater/electrode designs. For the first session, borosilicate glass-based prototypes utilizing the pattern A microheater/electrode circuit (**Figure 3-2a**) were used to analyze  $\text{CaCO}_3$ ,  $\text{CuO}$ ,  $\text{FeO}$ , and  $\text{MgO}$  contaminants. For the second testing session, ceramic-based prototypes featuring the pattern B circuit (**Figure 3-2b**) were used to analyze  $\text{Al}_2\text{O}_3$  and  $\text{NaCl}$  contaminants.

#### 3.6.1 Background Spectral Data

The background spectrum recorded at the beginning of each testing session was assumed to represent a typical ambient air spectral profile for that session. The first session background spectrum is illustrated in **Figure 3-5** and **Figure 3-6**.



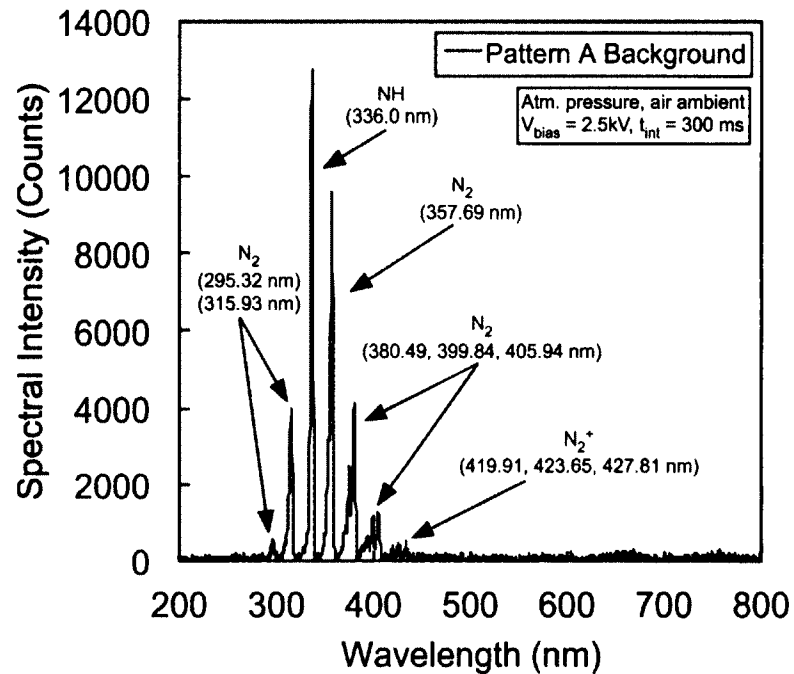


**Figure 3-5:** Air background spectrum of the first testing session.

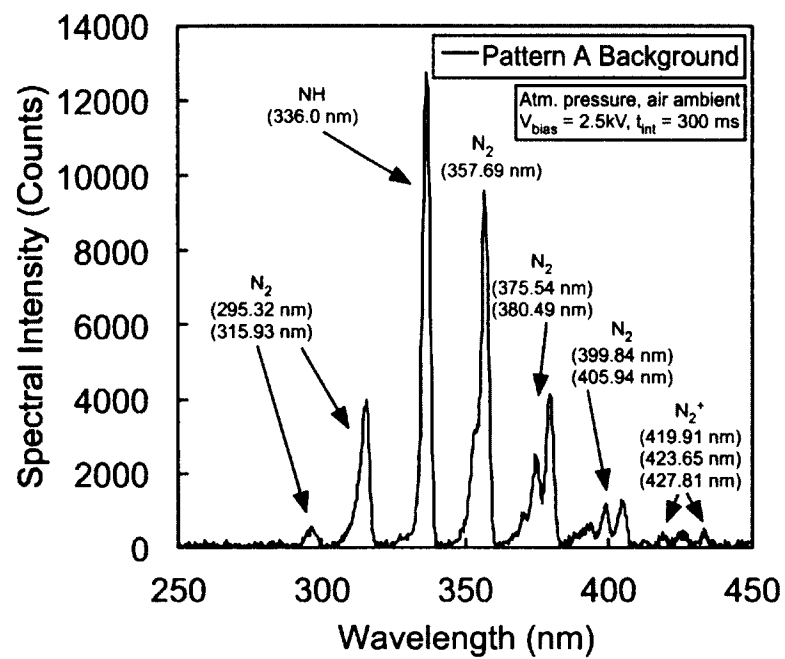


**Figure 3-6:** Close-up of the first session air background spectrum.

The spectral lines of ionized air molecules were concentrated within a 200 nm bandwidth between 250 and 450 nm. Because contaminants investigated in this work also emit spectral lines within this bandwidth, a close-up of the 250 to 450 nm region is shown in **Figure 3-6** as a reference. N-based spectra dominate this region, with the strongest lines corresponding to NH (336.0 nm) and N<sub>2</sub> (315.93, 357.69, and 380.49 nm). Where possible, **Figure 3-6** will be superimposed onto first session contaminant spectra to clearly distinguish contaminant-exclusive lines. Because the fiber/sensor orientation was not fixed during this work, the scale of background and contaminant spectral lines was often incompatible. In this case, the two data sets were not superimposed, as no meaningful comparison of the background and contaminant line intensities was possible.

The second testing session air background spectrum is illustrated in **Figure 3-7**. As before, N-based spectra dominate the background spectral profile, but now the relative ratios of N<sub>2</sub> (357.69 nm) and NH (336.0nm) have reversed. A new peak line is observed at 391.4 nm corresponding to O<sub>2</sub> and new O<sub>2</sub> line is observed at 777.9 nm. The shifting line intensity ratios between background spectra (and also background versus contaminant data) are likely due to fluctuations in the ambient air N and O ratios surrounding the sensor, particularly after a plasma discharge event. While the composition of air is generally constant, fluctuations in its major components can be expected with time, especially as the spectroscopic analysis session proceeds and the plasma discharge disturbs the local ratio of each component by ionization. As observed in **Figure 3-7**, the air background lines from the second session occupy a relatively smaller bandwidth, now between approximately 350 and 400 nm. As before, a close-up of the 300-450 nm band is shown in **Figure 3-8** as a reference.

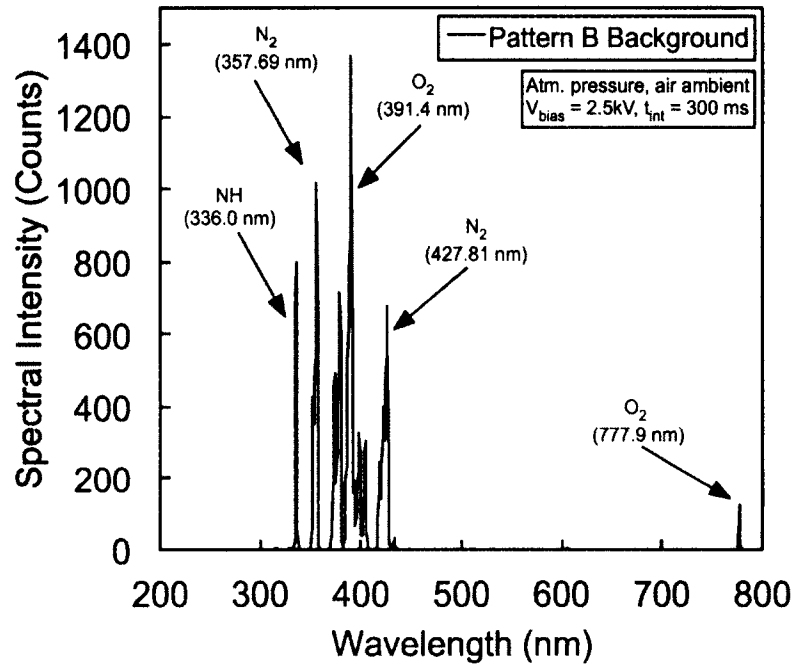


**Figure 3-7:** Air background spectrum of second testing session.

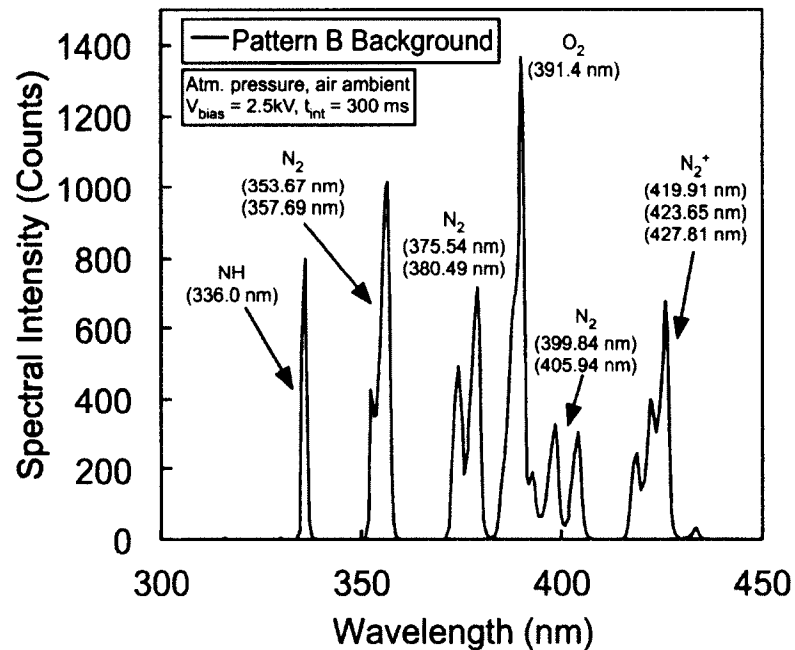


**Figure 3-8:** Close-up of the second session air background spectrum.

By comparing **Figure 3-6** and **Figure 3-8**, it can be seen that the background spectrum for each session contains many of the same molecular species of ionized air. The exceptions are the N<sub>2</sub> spectral group at 294.95 nm and 315.31 nm exclusive to **Figure 3-6** and the 391.64 nm O<sub>2</sub> line exclusive to **Figure 3-8**. The lack of this N<sub>2</sub> UV spectral group in the second session background is possibly due to differences in the orientation of the fiber optic during this session combined with the weaker sensitivity of the spectrometer and fiber optic to photons in the UVB region. While the spectral line intensities common to each session fluctuate, the overall shape of each background spectral profile is similar.

The most striking difference between the background spectra is the scale of the photon counts for each line. It can be seen that the spectra line intensities between the first (**Figure 3-6**) and second (**Figure 3-8**) sessions vary by an order of magnitude. Again, this difference is most likely due to variations in the orientation of the fiber optic cable with respect to the sensor during each session and between each test. For example, where the line intensities are greater, the optical fiber was likely closer to the plasma discharge and farther away where the line intensities are lower.

### 3.6.2 Al<sub>2</sub>O<sub>3</sub> Spectral Data

While Al<sub>2</sub>O<sub>3</sub> contaminants were analyzed at all concentrations, a potential spectral signature of the contaminant's atomic and molecular fragments was only observed at 100 ppm. Overall, these putative Al<sub>2</sub>O<sub>3</sub> atomic and molecular fragment lines were relatively weak and could not be unambiguously distinguished from the air background. For this test, the spectral line scale between the contaminant and second session background spectra were comparable, allowing their superposition as shown in

**Figure 3-9.** An effort was made to spectroscopically account for all atomic components of the  $\text{Al}_2\text{O}_3$  contaminant by identifying three spectral lines at 334.36 nm, 360.16 nm, and 396.1 nm potentially due to Al ions and two lines at 437.37 nm and 439.38 nm, possibly due to AlO molecules. (In **Figure 3-9** and all other spectral data in this work, ambiguous spectral lines are denoted with blue lines and unambiguous spectral lines are denoted with red lines.) The origin of the O component in the supposed AlO group also remains ambiguous as both lines could result from three different reactions, including:

- AlO released by the ionization of  $\text{Al}_2\text{O}_3$  contaminant particles;
- Recombination of Al and O released by ionized  $\text{Al}_2\text{O}_3$  particles; or
- Al released by ionized  $\text{Al}_2\text{O}_3$  particles recombining with atmospheric O.

Because it is plausible that all three reactions occur in the plasma discharge, the O component of the  $\text{Al}_2\text{O}_3$  contaminant cannot be entirely accounted for in this data set.

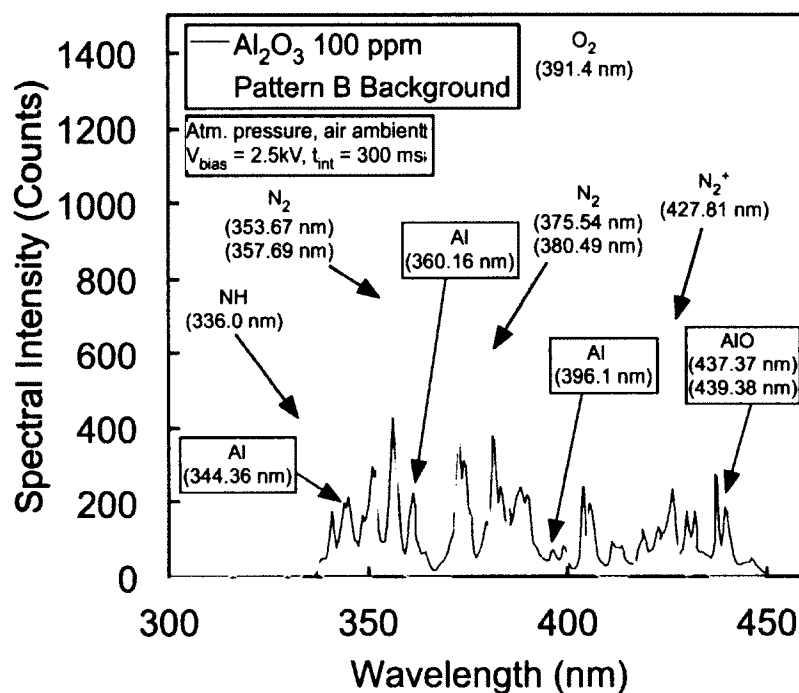


**Figure 3-9:**  $\text{Al}_2\text{O}_3$  atomic and molecular fragment spectrum at 100 ppm.

### 3.6.3 CaCO<sub>3</sub> Spectral Data

Similar to the Al<sub>2</sub>O<sub>3</sub> contaminant data, CaCO<sub>3</sub> contaminants were analyzed at all concentrations but the spectral signature of its atomic and (ambiguous) molecular fragments were observed only at 100 ppm, as shown in **Figure 3-10**. Unlike the Al<sub>2</sub>O<sub>3</sub> data set, however, the scale of spectral lines between the first session air background and the 100 ppm data set varied by an order of magnitude and the two spectra were not superimposed in **Figure 3-10**. However, CaCO<sub>3</sub> contaminants could still be partially identified by observing three relatively weak but unambiguous spectral lines corresponding to Ca ions at 393.37 nm and 396.85 nm and a single ambiguous line at 422.6 nm, which could be due to Ca ions or a CaO molecule.

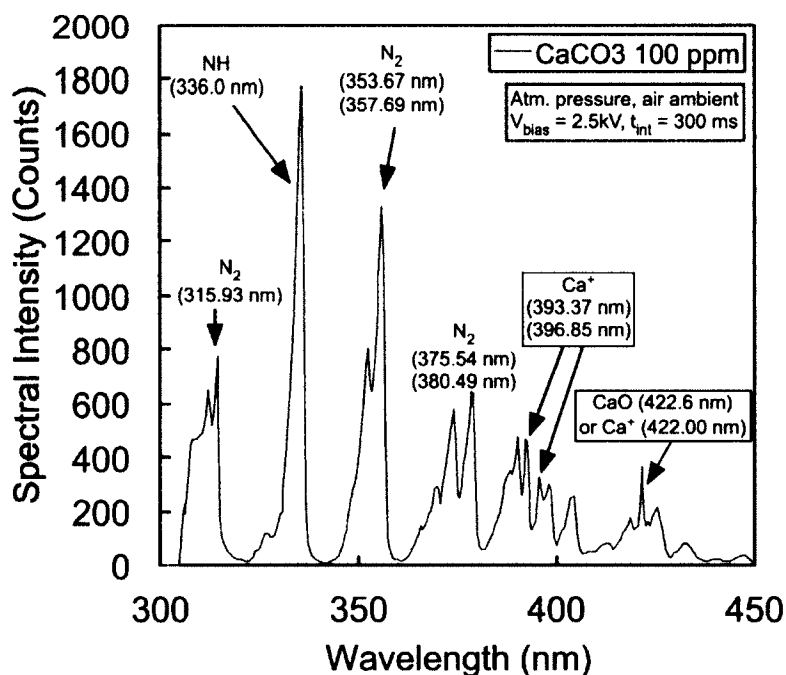


**Figure 3-10:** CaCO<sub>3</sub> atomic and molecular fragment spectrum at 100 ppm.

The ambiguity regarding the origin of the 422.6 nm spectral line is due to the line's relative weakness compared to the Ca lines in **Figure 3-10**. As with the supposed

AlO group in **Figure 3-9**, whether the O component of a putative CaO line at 422.6 nm in **Figure 3-10** originates from the CaCO<sub>3</sub> contaminant particles or the air background also remains unclear. In this case, the CaO line could result from three possible reactions:

- CaO released from ionized CaCO<sub>3</sub> contaminant particles;
- Recombination of Ca and O released from ionized CaCO<sub>3</sub> particles; or
- Recombination of Ca released from ionized CaCO<sub>3</sub> with atmospheric O.

Here again, it is very likely that each reaction could occur in the plasma and could contribute some portion of the photons giving rise to a CaO 422.6 nm line. However, without knowing the proportion of each reaction, the O component of the original CaCO<sub>3</sub> contaminant particles also cannot be completely accounted for this data set.

#### 3.6.4 CuO Spectral Data

The putative spectral signature of CuO fragments were potentially observed at 100 and 10 ppm but remained undetectable at 1 ppm. Unlike the previous two data sets, no molecular spectra resulting from the recombination of Cu with any air component was observed and the original CuO O component could not be accounted for in this data set. As with the CaCO<sub>3</sub> contaminant data, the spectral line scale between the first session air background and the 100 and 10 ppm CuO data sets were not compatible and the two spectra were not superimposed to distinguish the putative CuO fragment lines.

**Figure 3-11** illustrates the spectral profile of CuO contaminant particles observed at 10 ppm, where only two weak and ambiguous lines possibly due to Cu ions were observed at 324.7 nm and 327.3 nm. The ambiguity of these lines was due to their relative weakness compared to line intensity estimates given in spectral reference texts. The putative Cu lines were also observed to decrease with concentration (**Figure 3-12**).

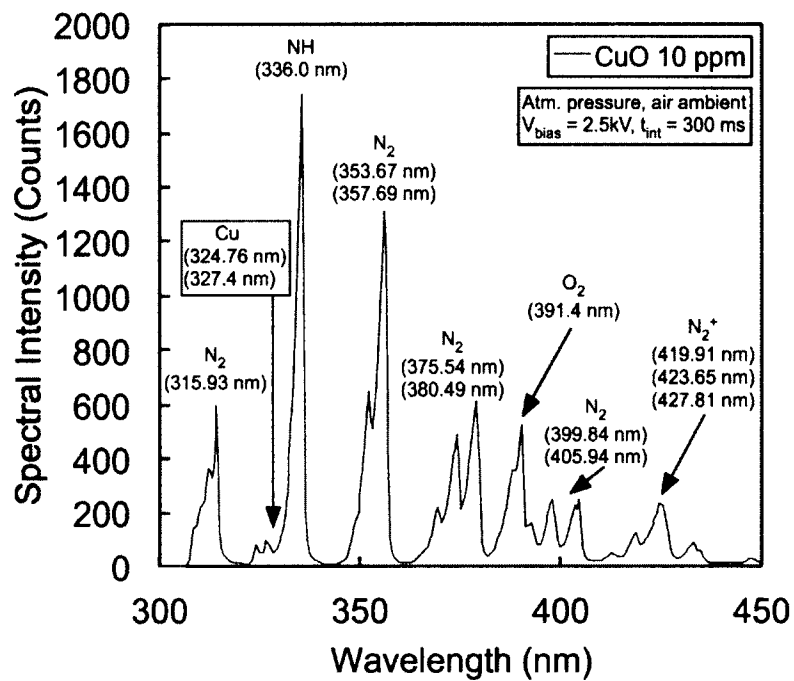


Figure 3-11: CuO atomic fragment spectrum at 10 ppm.

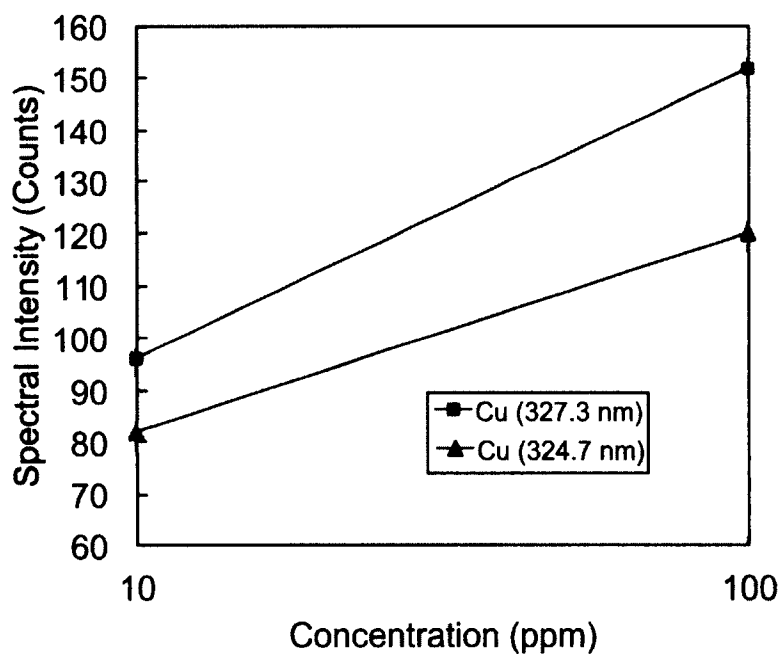
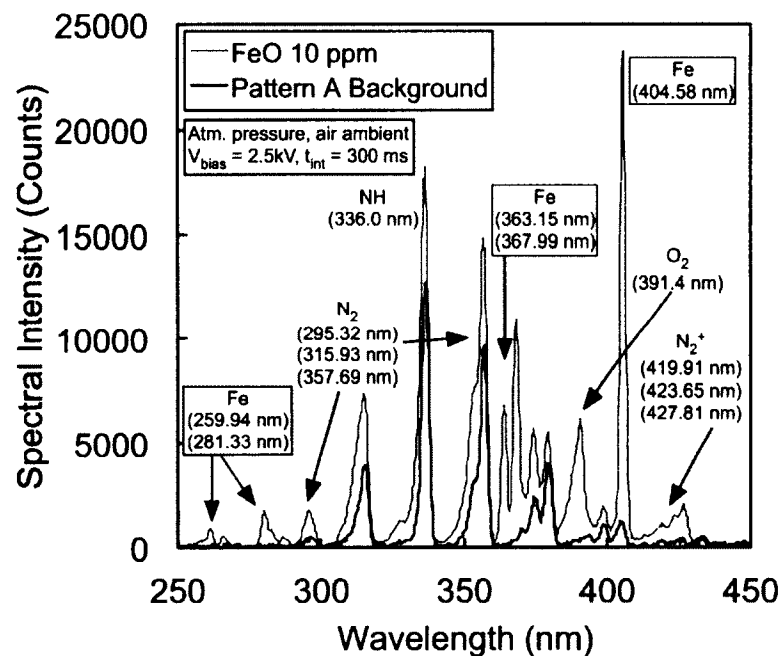


Figure 3-12: Cu ion spectral line intensity versus concentration.



### 3.6.5 FeO Spectral Data

The spectral signature of FeO contaminants was observed only at the 100 and 10 ppm concentration levels. For this contaminant test, the first session background, 100 ppm, and 10 ppm FeO spectral line scales were comparable, allowing the spectra to be superimposed in order to clearly distinguish the Fe contaminant fragment lines, as shown in the 10 ppm FeO spectrum in **Figure 3-13**.



**Figure 3-13:** FeO atomic fragment spectrum at 10 ppm.

FeO contaminants can be partially identified by observing four lines corresponding to Fe ions at 259.94 nm, 281.33 nm, 363.15 nm, and 404.58 nm. An atomic spectra reference text lists the relative spectral line intensity of Fe at 259.94 nm and 281.33 nm as being stronger than those at 363.15 nm and 404.58 nm (2000 and 2500 versus 1200 and 1500, respectively) [40]. Here, the significantly lower intensities for the 259.94 nm and 281.33 nm lines may be the result of the fiber optic orientation issue

discussed earlier, coupled with the reduced UV sensitivity of the spectrometer and fiber optic cables. The intensity of each Fe line in **Figure 3-13** was observed to decrease with contaminant concentration, as illustrated in **Figure 3-14**.

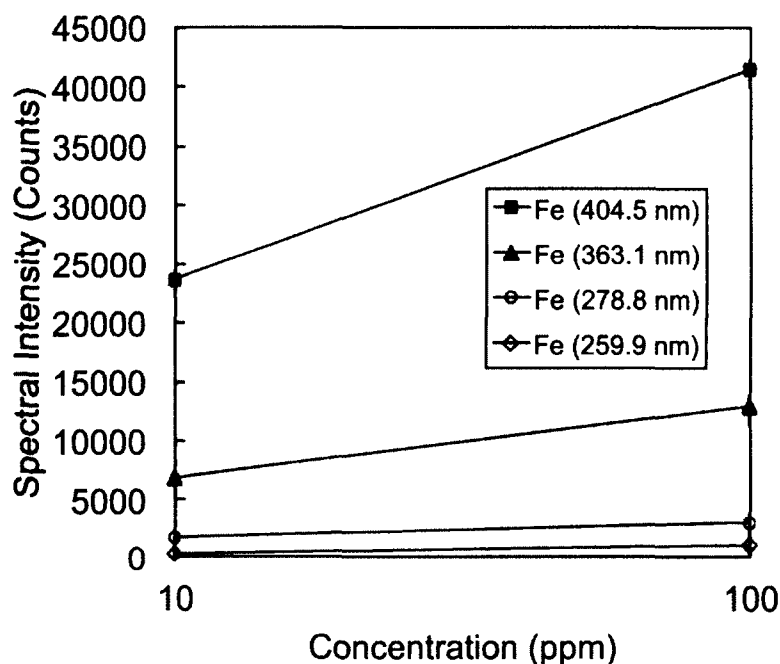


**Figure 3-14:** Fe ion spectral line intensity versus concentration.

Similar to the CuO data set, no spectra corresponding to the recombination of Fe with O or any other air component were detected. However, the diatomic O line at 391.4 nm in **Figure 3-13** was observed to be substantially higher in the FeO contaminant spectrum compared to that in the background, suggesting a potential but speculative means of accounting for the O content in the FeO contaminant particles.

#### 3.6.6 MgO Spectral Data

While MgO contaminants were tested at all concentration levels, the spectral signature of atomic and (ambiguous) molecular fragments was detected only at the 100 ppm concentration level, as shown in **Figure 3-15**.

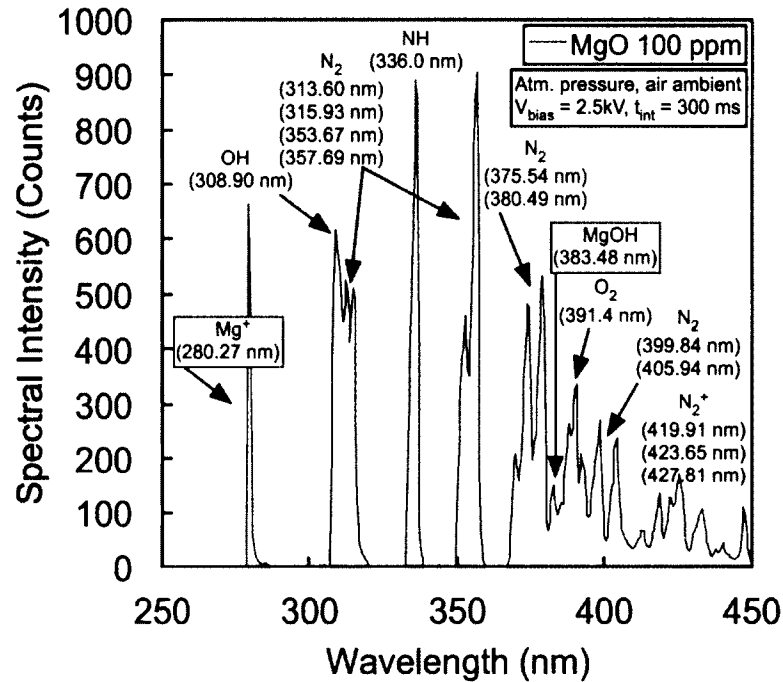


**Figure 3-15:** MgO atomic and molecular fragment spectrum at 100 ppm.

The spectral line scale of the first session air background was not comparable with that of the 100 ppm MgO data set and the two spectra were not superimposed in **Figure 3-15**. MgO impurities can be partially identified by observing a robust and unambiguous Mg ion line at 280.27 nm and a weaker, and therefore ambiguous, line at 383.48 nm, perhaps due to MgOH molecules. Similar to the putative AlO and CaO lines discussed earlier, the origin of the O in the putative MgOH line could have resulted from three different reactions in the plasma, including:

- MgO contaminant particles combining with atmospheric H;
- Mg and O released from ionized MgO combining with atmospheric H; or
- Mg released from ionized MgO combining with atmospheric O and H.

The robust OH line at 308.90 nm, which was not present in either background spectra, suggests a possible fourth reaction where contaminant Mg ions recombine with OH

produced in the plasma discharge from atmospheric H and O from the air or contaminant. However, as with previous data sets, this ambiguity prevents a full accounting of all atomic components in the original MgO contaminant particles.

### 3.6.7 NaCl Spectral Data

The spectral signature of NaCl contaminants was observed at 100, 10, and 1 ppm. However, the contaminant/background spectral line intensity scales were not comparable and were not superimposed in the 10 ppm data set shown in **Figure 3-16**. NaCl contaminants were partially identified by observing the robust Na spectral line at 589.00 nm and a significantly weaker and therefore ambiguous line at 465.51 nm, shown magnified in the **Figure 3-16** inset, which could possibly be due to a  $\text{Cl}_2^+$  molecule. The spectral intensity of the 589.00 nm Na line was observed to decrease as a function of NaCl concentration, as shown in **Figure 3-17**.

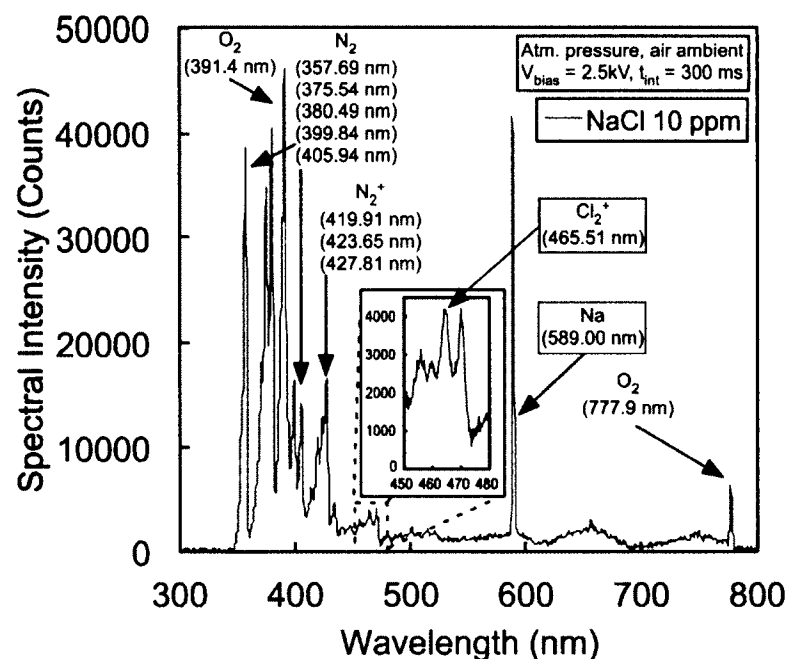


**Figure 3-16:** NaCl atomic fragment spectrum at 10 ppm.

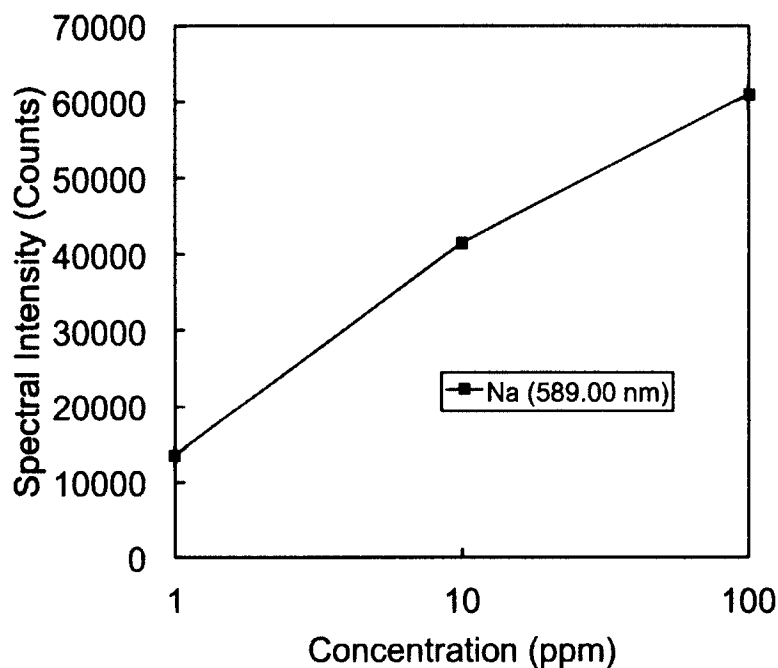


**Figure 3-17:** Na ion spectral line intensity versus concentration.

### 3.6.8 Microheater Performance

The thermal performance of the 200 nm pattern A and 100 nm and 50 nm pattern B Cr microheater elements were evaluated according to their maximum temperature change per unit of current. The microheaters' maximum temperature change was observed to decrease with decreasing Cr film thickness. This can be seen as a result of the total microheater resistance increasing with decreasing Cr film thickness.

The 200 nm pattern A microheater produced a maximum temperature change of 96 °C when supplied with 100 mA of current. For the 100 nm and 50 nm pattern B microheaters, temperature changes of 47 °C and 14 °C were recorded when supplied with 60 mA and 30 mA of current, respectively. The thermal performance of each microheater is summarized in **Figure 3-18**, as a function of supplied current.

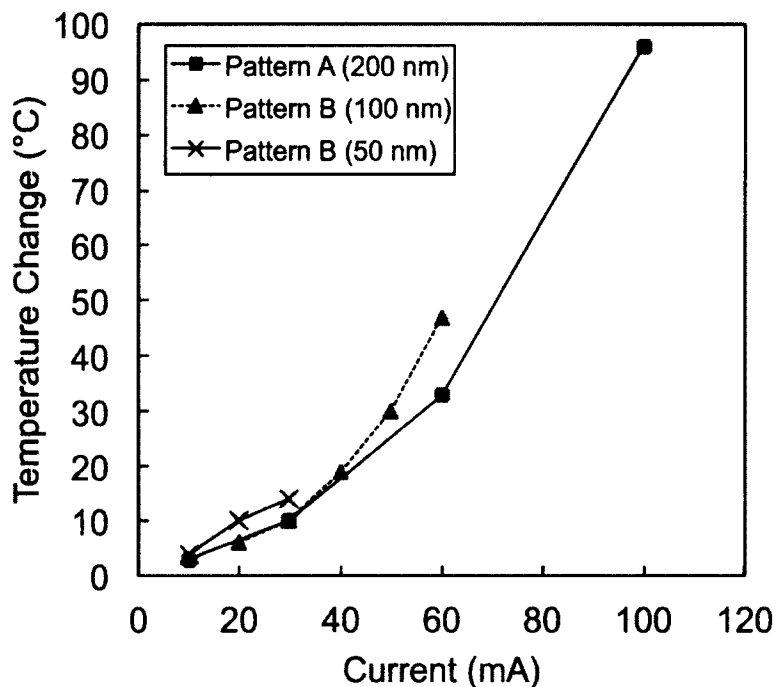


**Figure 3-18:** Thermal performance of pattern A and B thin-film heater prototypes.

### 3.7 Discussion

The major performance obstacles encountered in this work can be broadly categorized as issues related to the plasma spectroscopic platform's design and the experimental setup used to record the spectral data. The solutions to each issue proposed below will be incorporated into the design and experimental setup for the integrated water diagnostic device's plasma spectroscopic sensing element in Chapter 6.

#### 3.7.1 Design Issues

The primary device issue with the plasma spectroscopic sensor prototypes was the use of thin films to construct the microheater/electrode circuitry. While thin films proved suitable for the microheater element, sputtering of the thin electrode material during plasma spectroscopic analysis significantly limited the useful lifetime of individual devices. For pattern A devices, only three to five tests could be performed before the

electrode terminal was completely eroded due to sputtering. In this case, increasing the DC bias voltage could often still produce a plasma discharge, but this would simultaneously increase the rate of erosion of the remaining electrode material. This issue was considered during the design of the pattern B circuit by including two cathode electrode terminals. However, this solution would only increase the useful device lifetime of pattern B devices by one to three more tests.

After the electrode terminal was sufficiently eroded, the plasma was also observed to discharge randomly in locations along the heater coils not intended in the design of the device, causing limited or no contaminant spectral lines to be observed for that test and the erosion of material in the heater coil. Due to its integrated electrode and heater design, random sputtering of heater coil material would often result in a broken circuit, rendering the entire device inoperable.

From this initial investigation, it was concluded that thin films are not an ideal substrate for plasma electrodes, unless the spectral analysis procedure were perfected to ensure a successful collection of contaminant spectral data in a single test. While this level of operational consistency would be expected for a commercial device, it would be better at this stage in the sensor's development to utilize bulk metal filaments for the electrode material to minimize erosion by sputtering and maximize the device's useful lifetime. However, the heating element could still be constructed from thin films, as the microheaters did not exhibit any significant performance issues.

For future work, it would also be advantageous to increase the sample volume size by an order of magnitude to 1 mL to increase the density of particles in the contaminant film. Doing so could increase contaminant line intensities and improve

detection sensitivity. A greater density of contaminant particles would also allow a more sensitive capacitive analysis of contaminant concentration. Increasing the sample volume size to 1 mL would not drastically increase the size of the sample reservoir or compromise the device's field portability. In this case, the microheater design would have to be modified to increase its thermal output to compensate for the larger sample volume.

### 3.7.2 Experimental Issues

The primary issues related to the experimental setup were the fiber optic setup and the data collection procedure. First, a consistent fiber optic orientation with respect to the device should have been established before experiments began. By not doing so, the scale of spectral line intensities between the background spectra and contaminant spectra were often mismatched and the two spectra could not be superimposed to simplify the discrimination of contaminant spectral lines from the background. Collecting spectra from two fibers with significantly different aperture sizes compounded this issue. For future work, a consistent spectra collection setup will be used, including a fixed fiber optic orientation with respect to the device with a single fiber optic cable.

The second issue concerns the spectral collection and analysis procedure. Rather than recording a single spectrum sample, multiple spectra for each background and contaminant test should have been collected in order to statistically analyze the spectral data and gain more confidence in concluding whether a contaminant fragment line was detected or not. In future work, ten samples of each background and contaminant spectral data set will be collected to allow the average, maximum, and minimum intensities of a given line to be computed. Here, the average background photon counts at a wavelength suspected to contain a contaminant fragment line could be subtracted to give a total



number of photon counts exclusive to that particular line in the contaminant spectrum. The total number of contaminant-exclusive counts could then be compared with documented spectral lines found in spectra reference texts to more accurately determine whether the line in question results from the presence of the suspected contaminant or is a constituent of the air background.

### 3.8 Conclusion

Two prototypes of a miniaturized plasma spectroscopic platform were developed utilizing a water sample preconcentration stage to prepare for plasma spectroscopic, and in future work, capacitive analysis of water contaminants. The spectroscopic sensing platform was designed to operate in air at atmospheric pressure to simplify the analysis procedure and support development of a low cost and field portable integrated system. Two designs for the water sample preconcentration element, comprising a combined thin film Cr microheater and plasma electrode circuit, were explored on borosilicate glass and glass-mica ceramic substrates. Prototypes were used to observe the spectral signatures of  $\text{CaCO}_3$  and  $\text{MgO}$  contaminants at 100 ppm,  $\text{CuO}$  and  $\text{FeO}$  contaminants at 100 and 10 ppm concentrations, and  $\text{NaCl}$  contaminants at 100, 10, and 1 ppm. Microheaters fabricated from 200 nm Cr films produced a temperature change of 96 °C when supplied with 100 mA and 100 and 50 nm microheaters produced temperature changes of 47 °C and 14 °C when supplied with 60 mA and 30 mA, respectively. Multiple sensors were fabricated on each substrate using a single-mask photolithography process.

## CHAPTER 4

### CAPACITIVE SENSING PRINCIPLES

This chapter briefly describes the physical principles governing the capacitive sensing platform developed in this work. As described in Section 1.7, the capacitive sensing element is based on the parallel-plate capacitor geometry and so this discussion will be limited to that capacitor design.

#### 4.1 Capacitor Physics

Consider a device comprised of two flat and rectangular metal sheets of height  $h$  (m) and length  $l$  (m), separated by at a distance  $d$  (m) in a vacuum. If a positive charge  $+Q$  (C) is placed on the top plate of the device and a negative charge  $-Q$  (C) on the bottom plate, the electric field between the plates (ignoring fringe effects) is constant:

$$E = \frac{Q}{\epsilon_0 hl}, \quad \text{Eq. 4-1}$$

where  $E$  (V/m) is the electric field and  $\epsilon_0$  is the permittivity of free space ( $8.854 \times 10^{-12}$  F/m) [45]. The potential difference across the plates is also constant according to:

$$V = Ed \quad \text{Eq. 4-2}$$

The variables  $Q$  and  $V$  are related according to:

$$C = \frac{Q}{V} = \frac{Q}{Ed} = \frac{\epsilon_0 hl}{d}, \quad \text{Eq. 4-3}$$

where  $C$  (F) is the device's capacitance. (In general, capacitance is dependent on the frequency of the voltage source. However, because the capacitance measurement device used in this work utilizes a stable DC voltage, this frequency dependence can be ignored.) If a rectangular dielectric material is placed between the plates, filling the entire volume bounded by the  $h$ ,  $l$ , and  $d$  dimensions, the device's capacitance in Eq. 4-3 becomes:

$$C = \frac{\epsilon_0 \epsilon_r hl}{d}, \quad \text{Eq. 4-4}$$

where  $\epsilon_r$  is the unitless permittivity of the dielectric material. In this work, the dielectric material variable  $\epsilon_r$  introduced in Eq. 4-4 will be used to model the porous contaminant particle films housed in the rectangular capacitive analysis chamber, where two opposing chamber walls are patterned with metal plates to serve as the parallel-plate capacitor electrodes. Here, the permittivities of both the contaminant particles and the air-filled interparticle voids in the film have an effect on the film's total capacitance and must be considered in Eq. 4-4 for the most accurate estimate of the device's output capacitance. The methods for accounting for both variables in a single permittivity value are briefly summarized in Section 4.3.

## 4.2 Capacitor Circuits

Multiple dielectric configurations will be investigated in this work whose total circuit capacitance must be considered. A capacitor circuit with multiple dielectrics connected in parallel is illustrated in Figure 4-1. Here, the total capacitance  $C$  of each discrete capacitor device is described mathematically according to:

$$C = C_1 + C_2 + C_3 + \dots + C_n, \quad \text{Eq. 4-5}$$

where  $C_n$  (F) is the capacitance of the  $n^{\text{th}}$  capacitor in the network.

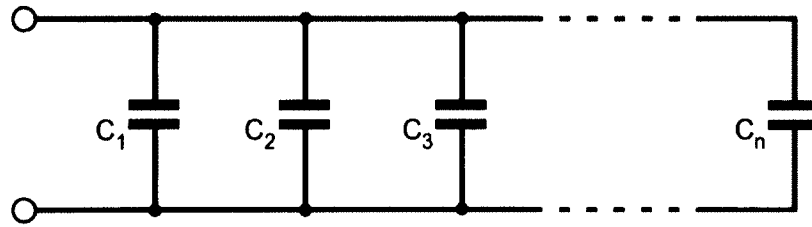


**Figure 4-1:** Parallel-connected capacitor network.

Similarly, multiple capacitor devices in a series-connected circuit are illustrated in **Figure 4-2**. Here, the total capacitance of the series-connected capacitor network is:

$$\frac{1}{C} = \frac{1}{C_1} + \frac{1}{C_2} + \frac{1}{C_3} + \dots + \frac{1}{C_n} \quad \text{Eq. 4-6}$$

Solving **Eq. 4-3** for  $C$  yields a more convenient representation of the circuit capacitance:

$$C = \frac{1}{\frac{1}{C_1} + \frac{1}{C_2} + \frac{1}{C_3} + \dots + \frac{1}{C_n}} \quad \text{Eq. 4-7}$$

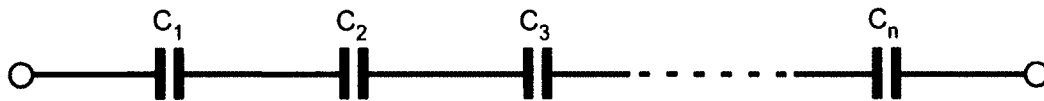


**Figure 4-2:** Series-connected capacitor network.

### 4.3 Dielectric Properties of Composite Materials

As described in Section 1.7, the contaminant particle films being investigated in this work are porous materials comprised of contaminant particles separated by interparticle voids filled with air. In this scenario, the capacitance of the contaminant film cannot be modeled in **Eq. 4-4** with a simple permittivity variable  $\epsilon_r$ , as this variable is

specific to a single material. The density of particles in the film will also change the film's dielectric properties, which  $\epsilon_r$  does not consider.

Considerable efforts have been made in the last several decades toward developing mathematical models to estimate the relative permittivity of homogeneously mixed, multi-component materials, such as the porous contaminant particles films under investigation in this work. The following three sections briefly outline the composite permittivity model research relevant to this work.

#### 4.3.1 Weiner's Limits

Weiner's upper limit  $\epsilon_U$  (unitless) describes the upper bound of a two-part composite material's effective permittivity by:

$$\epsilon_U = \phi_1 \epsilon_1 + \phi_2 \epsilon_2, \quad \text{Eq. 4-8}$$

where  $\phi_1$  and  $\phi_2$  are the unitless volume fractions of the first and second components in the composite material, respectively, and  $\epsilon_1$  and  $\epsilon_2$  are their respective permittivities [46].

Similarly, the lower bound  $\epsilon_L$  for the composite permittivity is described by:

$$\epsilon_L = \left[ \frac{\phi_1}{\epsilon_1} + \frac{\phi_2}{\epsilon_2} \right]^{-1}. \quad \text{Eq. 4-9}$$

#### 4.3.2 Lichtenecker's Mixture Formulation

Lichtenecker's logarithmic mixture equation has been demonstrated to give reliable estimates of a multi-part composite material's effective permittivity. As a leading composite permittivity model, it has been effectively applied to composite mineral [47] and polymer materials [48]. Furthermore, Lichtenecker's mixture equation has been shown to result from an application of charge conservation to Maxwell's equations [49].

For a homogeneous, multi-component material, its effective permittivity according to Lichtenecker's logarithmic mixture formula is:

$$\ln \varepsilon_{eff} = \sum_{n=1}^N \phi_n \ln \varepsilon_n, \quad \text{Eq. 4-10}$$

where  $\phi_n$  is the volume fraction occupied by the  $n^{th}$  material in the composite and  $\varepsilon_n$  is the ordinary relative dielectric constant of the  $n^{th}$  material [50] [51] [52] [53] [54].

#### 4.3.3 Modified Lichtenecker Mixture Formulation

While the original Lichtenecker composite permittivity formulation has been demonstrated to yield accurate composite permittivity estimates, two of the original assumptions on which it was based were shown in [55] and [56] to be false. The efforts in these two reports were focused on correcting the original formulation to achieve even greater composite permittivity accuracy. Their new formulation is rather complex, with multiple equations required for the application in this work spread over both papers. The unitless particle volume fraction  $\phi_1$  is described by:

$$\phi_1 = \frac{1}{2} - \frac{1}{2} \sqrt{1 - 4t}, \quad \text{Eq. 4-11}$$

where  $t$  is a place-holder variable, described by:

$$t = \frac{\varepsilon_1 + \varepsilon_2}{2(\varepsilon_1 - \varepsilon_2) \ln \left( \frac{\varepsilon_1}{\varepsilon_2} \right)} - \frac{\varepsilon_1 \varepsilon_2}{(\varepsilon_1 - \varepsilon_2)^2}, \quad \text{Eq. 4-12}$$

and  $\varepsilon_1$  and  $\varepsilon_2$  are the particle and air permittivities, respectively. The air volume fraction  $\phi_2$  is then defined according to:

$$\phi_2 = 1 - \phi_1. \quad \text{Eq. 4-13}$$

For  $\varepsilon_1 > \varepsilon_2$  and  $\phi_1 \leq \phi \leq \phi_2$ , the effective permittivity  $\varepsilon_{eff}$  of the two-component composite material is described by:

$$\varepsilon_{eff} = \frac{1}{2} \left[ \frac{A(\phi_1)}{2C(\phi_1)} + \frac{B(\phi_2)}{2C(\phi_2)} \right] C(\phi) Z(\phi) \quad \text{Eq. 4-14}$$

$A(\phi_1)$  is described by:

$$A(\phi_1) = 1 + \frac{1}{(\varepsilon_U)^n (\varepsilon_L)^n} \quad \text{Eq. 4-15}$$

$B(\phi)$  is described by:

$$B(\phi) = 1 + \frac{1}{(\varepsilon_U)^{n-1} (\varepsilon_L)^{n-1}} \quad \text{Eq. 4-16}$$

$C(\phi)$  is described by:

$$C(\phi) = \sqrt{\frac{\varepsilon_L(\phi)}{\varepsilon_U(\phi)}} \varepsilon_1^\phi \varepsilon_2^{1-\phi} \quad \text{Eq. 4-17}$$

$Z(\phi)$  is described by:

$$Z(\phi) = \frac{\varepsilon_U^n(\phi)}{\varepsilon_L^{n-1}(\phi)} \quad \text{Eq. 4-18}$$

For  $\varepsilon_1 > \varepsilon_2$ ,  $n$  is defined in [55] by:

$$n = \frac{5-M}{4} \quad \text{Eq. 4-19}$$

where  $M$  is defined by:

$$M = \frac{2}{m-1} \quad \text{Eq. 4-20}$$

and  $m$  is a function of the unitless eccentricity  $e$  of the particles according to:

$$m = e^2 \left[ 1 - \sqrt{1 - e^2} \frac{\sin^{-1} e}{e} \right]^{-1} \quad \text{Eq. 4-21}$$

Spherical particles have an eccentricity of zero while ellipse-shaped inclusions vary from  $0 \leq e \leq 1$ . For this work, the contaminant particles were assumed to be spherical ( $e=0$ ).



## **CHAPTER 5**

### **CAPACITIVE SENSING PLATFORM**

#### **5.1 Research Objectives**

This chapter discusses the design, fabrication, and testing of the first generation capacitive sensing platform and the development of a mathematical concentration-to-capacitance model to interpret the sensor's output<sup>1</sup>. Within the integrated water diagnostic device, this system will be used to identify the concentration of a water contaminant by comparing the capacitive output of the capacitive sensor against that simulated by the numerical model for a given contaminant concentration. An updated embodiment of each component (sensor and model), based on performance and experimental procedure issues uncovered in this initial development effort, will be incorporated into the integrated water diagnostic system discussed in Chapter 6.

The primary objective of this work was to evaluate the feasibility of the capacitance-based contaminant concentration analysis concept. As with the plasma spectroscopic platform in Chapter 3, secondary objectives included minimization of the capacitive sensor's mass, volume, and external hardware requirements to support the final integrated system's field portability and development of a fabrication process that favored inexpensive materials amenable to batch-fabrication, where possible.

---

<sup>1</sup> Portions of this work were applied toward a Master's Degree Practicum in Applied Physics.

## 5.2 Design Considerations

The concentration-to-capacitance model derived in this chapter requires the water contaminant's chemical composition to be known so that its physical properties—including density, bulk (powdered) density, and relative permittivity—can be incorporated into the numerical model in order to yield the most accurate capacitance estimate. As discussed in Section 1.6 regarding the final integrated diagnostic system's intended operation, the preconcentrated film's capacitance will be measured first to preserve its original dielectric properties before ionization during the plasma spectroscopic analysis. After spectroscopically identifying the contaminant, the numerical model will be updated with the contaminant's relevant physical parameters and a theoretical capacitance estimate will be calculated to compare against the preconcentrated film's experimental capacitance. Development of the capacitive sensing platform and contaminant concentration-to-capacitance model described in this chapter will therefore assume a complete and accurate plasma spectroscopic identification of the water contaminants under investigation. In a later section, this assumption will be expanded to include water samples containing multiple contaminant species, whose relative ratios in the sample, by mass, are assumed to be calculable from spectroscopic data.

While the EPA's water quality regulations regarding impurity concentration vary with the water source's location, use, and the contaminant species in question, maximum contaminant concentration limits in the range of 0.01 to 0.1 g/L are typical [7]. This concentration range was therefore used as the lower bound of the contaminant concentrations to be investigated in this work in order to characterize the sensor's performance within EPA regulation limits.

### 5.3 Capacitive Sensor Design

The capacitive sensing platform utilizes the same preconcentration process developed in Chapter 3 to convert the water sample into a dry and porous contaminant particle film, which now serves as one of two dielectric materials in a parallel-plate capacitor (air is the second dielectric material). Here, the dimensions of the sample analysis chamber housing the contaminant film correspond to the dimensional variables in the general parallel-plate capacitor formula (Eq. 4-4), which serves as the foundation for the numerical capacitance-to-concentration model.

The idealized capacitive sensor embodiment consists of a rectangular parallel-plate capacitive sensing element and a thin film microheater, as illustrated in Figure 5-1.

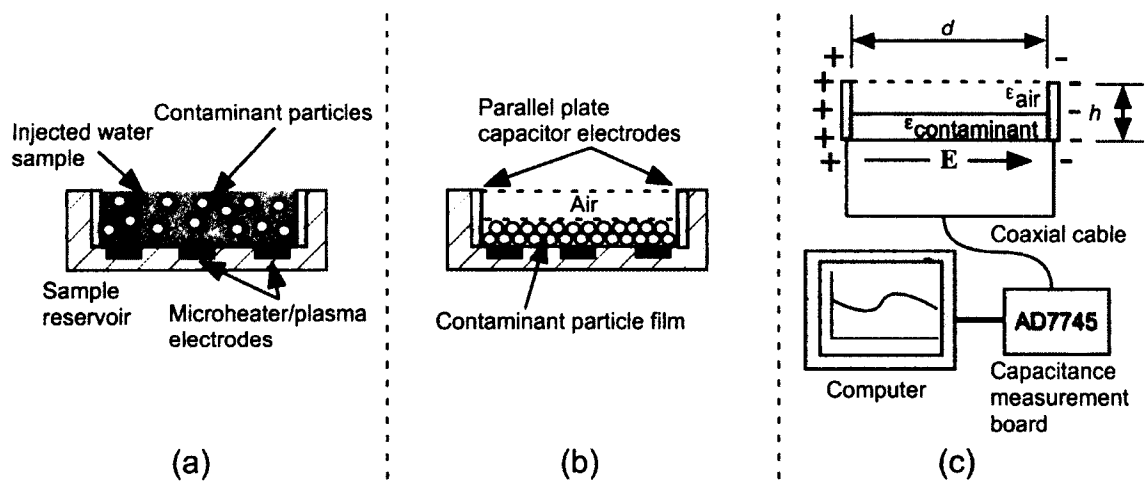


**Figure 5-1:** Capacitive analysis of water contaminant concentration.

A rectangular cavity functions as a combined water sample reservoir and capacitive analysis chamber, where two opposing cavity walls are patterned with metal to serve as the plates of a parallel-plate capacitor (Figure 5-1a). A water sample injected into the reservoir is preconcentrated into a contaminant particle film with uniform dimensions and density by applying current to an on-chip microheater patterned to the

reservoir base (**Figure 5-1b**). Contaminant particles and the air filling both the interparticle voids in the porous film and the remainder of the reservoir volume now function as two dielectric materials in a parallel-plate capacitor (**Figure 5-1c**). In this arrangement, the total capacitance between the plates can be represented as the combined capacitance of the contaminant particle film and air capacitors connected in parallel. This combined capacitance of all materials occupying the reservoir chamber is then recorded with an off-chip capacitance measurement board via coaxial leads soldered to each plate.

The numerical concentration model is used to simulate this combined capacitance, where the water contaminant's concentration was treated as a known variable. The numerical model's accuracy is evaluated by comparing its theoretical capacitance values for a contaminant at a given concentration against those capacitance values measured experimentally with the capacitive sensor. To simulate real-world environmental testing scenarios as closely as possible and to more fully characterize the feasibility of the concentration-to-capacitance analysis concept, numerical models for water samples containing single and multiple contaminant species were developed and tested.

### 5.3.1 Design Modifications

The first generation capacitive sensor design incorporated three design modifications to the idealized embodiment described above in order to accelerate the concept's feasibility study. The principal design modification included a mechanism to vary the capacitor plate electrode spacing. This feature was investigated to determine the ideal plate electrode separation distance for optimum capacitive sensitivity. Initially, it was assumed that smaller electrode separation distances would be preferable, as this configuration would result in a higher baseline capacitance (*i.e.* capacitance of only air in

the analysis chamber, no contaminants) and a more favorable signal-to-noise ratio, according to the generalized formula for a rectangular parallel-plate capacitor:

$$C = \frac{\epsilon_r \epsilon_0 x l}{d}, \quad \text{Eq. 5-1}$$

where  $C$  is the capacitance of the parallel-plate capacitor (F),  $\epsilon_r$  is the permittivity of the dielectric material,  $\epsilon_0$  is the vacuum permittivity (F/m),  $x$  and  $l$  are the height and length of the dielectric material (m), respectively, and  $d$  is the plate separation distance (m).

According to Eq. 5-1, the total chamber capacitance is inversely proportional to the plate spacing, which should be minimized for a maximum capacitive signal-to-noise ratio.

Because the permittivity of the contaminants under investigation are greater than that of air, the addition of contaminant particles to the analysis chamber will increase the total capacitance above the baseline level. However, the volume between the electrodes simultaneously functions as the water sample reservoir and smaller electrode separation distances would limit the quantity of contaminant particles that could occupy the reservoir volume. As the quantity of contaminant particles decreases, their total capacitance and the sensor's signal-to-noise ratio will also decrease. Selecting the sample reservoir and analysis chamber dimensions then represented a compromise between minimizing the chamber volume (and water sample volume) for field portability and maximizing the sensor's baseline capacitance to obtain a favorable signal-to-noise ratio.

Two secondary design modifications followed as a consequence of utilizing variable plate spacings. As the water sample reservoir volume would also be variable, water sealing the reservoir chamber to prevent leaks and contain the contaminant particles would be problematic. For this reason, rather than prepare liquid water samples during the experimental testing phase, a universal water sample size was selected and the

mass of contaminant particles that would be contained in a sample for each contaminant concentration were calculated and manually added to the analysis chamber. Second, as it would not be necessary to preconcentrate liquid water samples, the first generation capacitive sensor prototype did not include an on-chip microheater element.

### 5.3.2 Device Parameters

The minimum resolvable capacitance of the capacitance measurement board used in this work was 4 fF with a resolution of 4 aF (see Section 5.6). Therefore, the analysis chamber dimensions would be required to produce a baseline capacitance value that met, but ideally exceeded, this value. To that end, a preliminary concentration-to-capacitance model based on Eq. 5-1 was developed to simulate the baseline capacitance for a variety of analysis chamber dimensions, plate spacings, water sample volumes, and contaminant concentrations. The goal of this initial study was to determine the optimum values for each variable that would support both a miniaturized device and a satisfactorily high baseline capacitance and signal-to-noise ratio.

The water sample volume variable was given precedence in this optimization process because this variable would have the greatest effect on the quantity of contaminant particles being analyzed by both sensing platforms. Increasing the original 100  $\mu\text{L}$  water sample volume to 1 mL was proposed in Section 3.7.2 as a means to improve the detection capabilities of both sensing platforms by increasing the contaminant particle film mass by an order of magnitude. With 1 mL water samples, the minimum concentration range to be investigated (0.1 g/L) was estimated to result in a small but appreciable contaminant film mass ( $\sim 100 \mu\text{g}$ ) with capacitance values well above the noise floor of the measurement board. Further experimentation with the values

for each analysis chamber dimension showed that 1 mL samples would also yield particle film volumes compatible with analysis chamber dimensions on the order of 0.5 to 10 millimeters. 1 mL was then selected as the universal water sample volume from which contaminant masses at each concentration level would be calculated and tested.

Next, the height and length of the analysis chamber were selected to be 1 mm and 10 mm, respectively, with a minimum plate spacing of 0.59<sup>2</sup> mm, resulting in a minimum analysis chamber volume of 5.9 mm<sup>3</sup> (0.0059 mL). In all, seven plate spacing were investigated, including 0.59, 1.0, 1.59, 2.0, 2.59, 3.0, and 3.59 mm. Theoretical baseline capacitances (simulated with Eq. 5-1) for an empty capacitive analysis chamber filled with only air at each plate spacing are shown in Table 5-1. Here, it can be seen that the baseline capacitance for each plate spacing is well above the 4 fF (0.004 pF) limit of the measurement board, with 1.00 and 0.59 mm spacings yielding the greatest minimum capacitance values (highlighted in blue). These calculations also do not include the fringe capacitance estimates of the real capacitor device, which will increase the baseline capacitance further (see Section 5.6).

**Table 5-1:** Theoretical baseline capacitances as a function of plate spacing.

| Capacitor Plate Spacing, $d$ (mm) | Theoretical Baseline Capacitance, $C$ (pF) |
|-----------------------------------|--|
| 1.59                              | 0.055716                                   |
| 2.00                              | 0.044294                                   |
| 2.59                              | 0.034204                                   |
| 3.00                              | 0.029529                                   |
| 3.59                              | 0.024676                                   |

<sup>2</sup> Plate spacings were originally intended to vary at 0.50 mm increments. The reference spacer used to set each 0.50 mm increment was found to be 0.59 mm after testing was concluded. All calculations reflect the true 0.59 mm width.

## 5.4 Contaminant Concentration Models

To effectively model the total capacitance of the contents of the analysis chamber, the dielectric properties of both the porous contaminant particle film and the air occupying the remainder of the chamber volume must be considered. Furthermore, the dielectric properties of the air occupying interparticle voids in the porous contaminant film must also be incorporated into the model. Based on these considerations, three assumptions simplified the concentration-to-capacitance model derivation, including:

- (1) Contaminant particles do not adhere to the sample reservoir and analysis chamber walls during the preconcentration stage;
- (2) Contaminant particles accumulate at the base of the analysis chamber as a porous film with a uniform thickness (height), width, length, and density; and
- (3) A practical estimate of the contaminant film's porosity can be calculated from the contaminant material's density and experimentally measured bulk density.

The first two assumptions provide a means of separating the capacitance of the contaminant particle film from that of the ambient air space filling the remainder of the analysis chamber volume. Here, the particle film and air space can be modeled as two distinct rectangular dielectrics with uniform height, width, length, and density. Because the two materials are also stacked and bounded on two sides by the capacitor plates, the total capacitance of these two dielectrics can be modeled as two capacitors connected in parallel. The third assumption regarding the air content of the porous film will be addressed in the derivation of the numerical model in the following section.

Once a contaminant's chemical composition has been identified in the plasma spectroscopic analysis phase, the total capacitance of the analysis chamber can be



modeled as a function of the contaminant material's density, bulk density, and permittivity, the permittivity of air, and the physical dimensions of the analysis chamber, as illustrated in **Figure 5-2**. The capacitor plate height and length are defined by  $h$  (m) and  $l$  (m), respectively, and the capacitor plate separation is defined by  $d$  (m) (**Figure 5-2a**). The height of the uniform contaminant particle film is  $x_p$  (m) and the height of the volume of air space occupying the remainder of the reservoir volume is represented by  $h - x_p$  (m) (**Figure 5-2b**). The length of the analysis chamber and both dielectrics is defined by  $l$  (m), normal to the page. Therefore, the volume occupied by the particle film and air space dielectrics can be calculated as  $x_p \times l \times d$  and  $(h - x_p) \times l \times d$ , respectively.

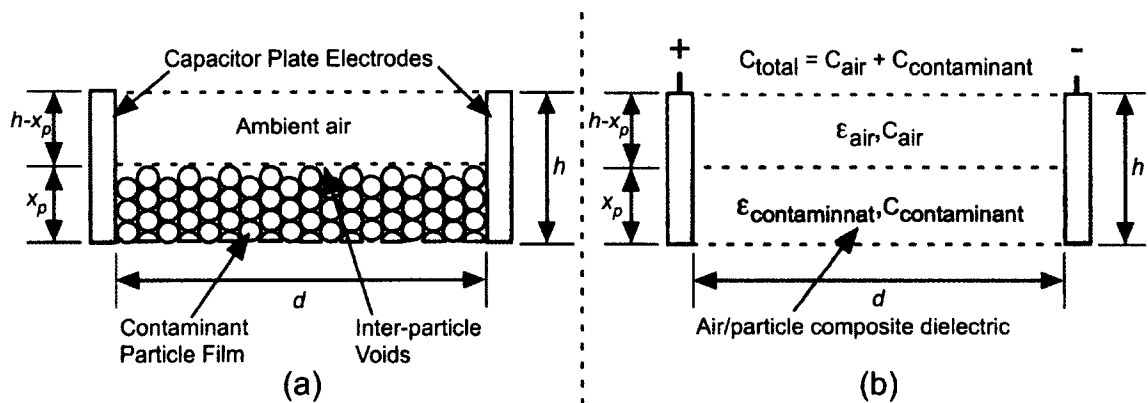


**Figure 5-2:** Parallel dielectric layers of the contaminant particle film and air space.

#### 5.4.1 Single Contaminant Concentration Model

The concentration of a single contaminant species in a water sample is defined by:

$$\beta_p = \frac{m_p}{v_s}, \quad \text{Eq. 5-2}$$

where  $\beta_p$  is the contaminant particle concentration (g/L),  $m_p$  is the total contaminant mass in the sample (g), and  $v_s$  is the original volume of the water sample (L). The subscripts  $p$  and  $s$  used in the derivation of the numerical models and the MATLAB m-file codes used

to simulate them stand for particle (contaminant) and sample (original water sample volume), respectively. Eq. 5-2 can then be rearranged to describe the total mass of contaminant particles in the sample for a given concentration as:

$$m_p = \beta_p v_s \quad \text{Eq. 5-3}$$

If the contaminant particle film is assumed to resemble a rectangle whose base dimensions are equal to that of the sample reservoir and analysis chamber, the height,  $x_p$ , of the contaminant particle film can be calculated according to:

$$x_p = \frac{m_p}{\eta_p dl} \quad \text{Eq. 5-4}$$

where  $\eta_p$  is the contaminant material's bulk density ( $\text{g}/\text{m}^3$ ), which is the density of the material in powdered form. In reality, however, the contaminant particle film is porous and more closely resembles an aggregate of particles separated by interparticle air voids bounded by the dimensions  $x_p$ ,  $d$ , and  $l$ . The interparticle void volume can then be separated from the contaminant particle volume as shown schematically in Figure 5-3.

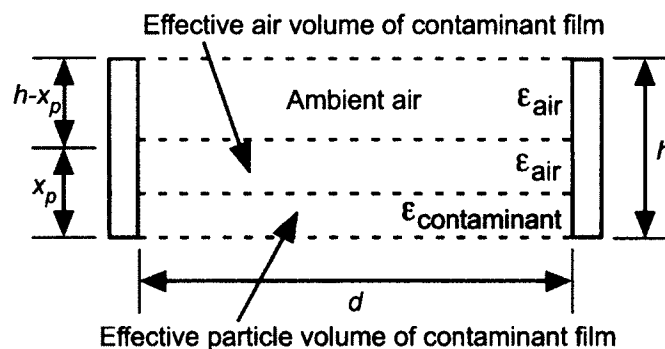


**Figure 5-3:** Effective volume of contaminant particles and voids in the porous film.

Here, the porous contaminant particle film then is effectively a composite dielectric material whose composite permittivity cannot be assumed to be a linear

combination of its components' ordinary relative permittivities. The composite film's effective relative permittivity must therefore be calculated to also include the dielectric properties of the air occupying the interparticle voids. By doing so, it will then be possible to calculate the composite capacitance of the entire porous contaminant particle film, as a function of the dielectric properties of each material in the composite and the total volume that each material occupies.

For a two-part composite material comprised of particles of a single contaminant species separated by interparticle voids filled with air, Lichtenecker's mixture equation (Eq. 4-10), discussed in Section 4.3.2, can then be expanded to calculate the effective permittivity  $\epsilon_{eff}$ , of the porous contaminant particle film by:

$$\ln \epsilon_{eff} = \phi_{air} \ln \epsilon_{air} + \phi_p \ln \epsilon_p, \quad \text{Eq. 5-5}$$

where  $\phi_{air}$  and  $\phi_p$  are the unitless volume fractions of the air occupying the interparticle voids in the porous contaminant film and the contaminant particles, respectively, and  $\epsilon_p$  is the relative permittivity of the contaminant particle material. Moreover, Eq. 5-5 can be expanded further to calculate the effective dielectric constant of a porous contaminant film with multiple contaminant species, provided the ordinary relative dielectric constants and volume fractions occupied by each contaminant species and the interparticle air voids contained in the film are known or can be estimated numerically.

Next, the volume fractions occupied by the contaminant particles and interparticle air voids in the contaminant film must be calculated. In general, the unitless porosity  $n$  of a powdered material is defined by:

$$n = 1 - \frac{W_s}{G\gamma_{H_2O}V}, \quad \text{Eq. 5-6}$$

where  $W_s$  is the weight of the material's solid particles in pounds (lb),  $V$  is the total volume occupied by the material (ft<sup>3</sup>),  $\gamma_{H_2O}$  is the density of water (62.4 lb/ft<sup>3</sup>), and  $G$  is the specific gravity of the material according to:

$$G = \frac{W_s}{V_p \gamma_{H_2O}}, \quad \text{Eq. 5-7}$$

where  $V_p$  is the volume occupied by the material's solid particles (ft<sup>3</sup>). Combining Eq. 5-6 and Eq. 5-7 then simplifies to:

$$n = 1 - \frac{V_p}{V}. \quad \text{Eq. 5-8}$$

The volume occupied by the porous materials solid particles can be estimated by dividing the film's mass by the material's solid density according to:

$$V_p = \frac{m_p}{\rho_p} \quad \text{Eq. 5-9}$$

and the total porous film volume can be estimated with the material's bulk density by:

$$V = \frac{m_p}{\eta_p}. \quad \text{Eq. 5-10}$$

If the porous contaminant particle film's volume is assumed to be bounded by the sample reservoir base dimensions  $l$  and  $d$  and the contaminant height  $x_p$ , the fractional volume of air voids and contaminant particles filling this volume can be estimated by calculating the volume difference between the contaminant particle film as a solid material (no interparticle voids) with dimensions  $x_p$ ,  $l$ , and  $d$  and the porous contaminant film (with interparticle voids) using the same dimensions [57]. Therefore, the fractional volume of contaminant particles filling the porous film volume defined by  $l$ ,  $d$ , and  $x_p$ , can be estimated according to:

$$\phi_p = V_p = \frac{\eta_p}{\rho_p}, \quad \text{Eq. 5-11}$$

where  $\phi_p$  is the unitless volume fraction occupied by the contaminant particles and  $\rho_p$  is the density of the contaminant material as a solid ( $\text{g/m}^3$ ). From **Eq. 5-11**, the volume fraction of air in the porous contaminant film,  $\phi_{air}$ , can then be calculated according to:

$$\phi_{air} = 1 - \phi_p. \quad \text{Eq. 5-12}$$

The composite permittivity of the porous contaminant particle film can then be calculated by inserting  $\phi_p$  and  $\phi_{air}$  into **Eq. 5-5** and solving for  $\epsilon_{eff}$ :

$$\epsilon_{eff} = e^{\phi_{air} \ln \epsilon_{air} + \phi_p \ln \epsilon_p}. \quad \text{Eq. 5-13}$$

The capacitance contribution of the contaminant particle film  $C_p$  (F) to the total sample reservoir/analysis chamber capacitance can then be calculated from the general formula for a parallel plate capacitor by inserting  $x_p$ ,  $\epsilon_{eff}$ , and the dimensions of the contaminant dielectric into **Eq. 5-1**:

$$C_p = \frac{\epsilon_{eff} \epsilon_0 x_p l}{d}. \quad \text{Eq. 5-14}$$

Similarly, the capacitance  $C_{air}$  (F) of the air filling the unoccupied volume of the sample reservoir bounded by  $(h-x_p)$ ,  $l$ , and  $d$  can then be calculated with **Eq. 5-1** by:

$$C_{air} = \frac{\epsilon_{air} \epsilon_0 (h - x_p) l}{d}. \quad \text{Eq. 5-15}$$

The total capacitance of the rectangular particle film and air dielectrics can then be computed as two separate capacitors connected in parallel according to:

$$C = C_p + C_{air}. \quad \text{Eq. 5-16}$$

Finally, the total capacitance  $C$  (F) of the sample reservoir/capacitive analysis chamber can be calculated by inserting Eq. 5-14 and Eq. 5-15 into Eq. 5-16, yielding:

$$C = \frac{\epsilon_{eff}\epsilon_0 x_p l}{d} + \frac{\epsilon_{air}\epsilon_0 (h-x_p)l}{d} \quad \text{Eq. 5-17}$$

#### 5.4.2 Multiple Contaminant Concentration Model

In a typical environmental testing scenario, it is very unlikely that a polluted water source would contain only one contaminant species. While it is certainly possible for a single contaminant species to dominate the water source's impurity profile, other contaminant species will likely be present, to some degree. To represent this environmental testing reality more accurately and attempt to characterize the performance of the capacitive sensing platform and numerical model in this context, the single contaminant numerical concentration-to-capacitance model derived in the previous section was modified to accommodate water samples with multiple contaminant species.

As with the single contaminant model, the multi-contaminant concentration-to-capacitance model also relies on an assumed complete and accurate plasma spectroscopic analysis of the contaminant particles' chemical composition. Additionally, the multi-contaminant concentration-to-capacitance model capitalizes on a secondary assumption regarding the spectroscopic analysis phase, namely that the relative ratios of each contaminant species in the film can be accurately deduced in the spectroscopic analysis. For example, the line intensities of each contaminant's atomic and molecular fragments could be compared to that of a background reference line, such as sputtered metal electrode material, to spectroscopically determine each contaminant's relative proportion in the sample. This concept was originally proposed in [30] but has yet to be fully

explored in a MEMS-scale device. Furthermore, the author's discussion of this concept did not include a means to calculate the water contaminant's concentration in standard environmental testing units, such as grams-per-liter or parts-per-million.

The primary challenge of calculating the theoretical capacitance of a multi-contaminant film lies in estimating the height of the contaminant particle film  $x_p$ . To determine  $x_p$  (in a manner similar to **Eq. 5-4**), the bulk density the multi-component film must be calculated first, as a function of the total particle mass in the film and the sum of the volumes occupied by each contaminant species' particles. As before, the multi-contaminant model regards the total contaminant concentration  $\beta_p$  as a known variable, so that the total mass of contaminant particles  $m_p$  can be calculated according to **Eq. 5-3**.

The spectroscopically-deduced relative ratios of each contaminant species in the sample are described by the variable  $a_n$ , where:

$$\sum_{n=1}^{\infty} a_n = a_1 + a_2 + a_3 + \dots + a_n = 1 \quad \text{Eq. 5-18}$$

and  $a_n$  represents the relative proportion of the  $n^{\text{th}}$  contaminant species in the film, by mass. The mass of the  $n^{\text{th}}$  contaminant species' particles in the film is then:

$$m_n = m_p a_n, \quad \text{Eq. 5-19}$$

where  $m_n$  (g) is the mass of the  $n^{\text{th}}$  contaminant particles in the porous film.

Next, the volume occupied by each contaminant species' particles and the air-filled interparticle voids must be estimated. The volume occupied by each contaminant particle mass  $m_n$  as a solid, which will be required in a later step, can be calculated by:

$$v_n = \frac{m_n}{\rho_n}, \quad \text{Eq. 5-20}$$

where  $v_n$  is the volume occupied by the  $n^{\text{th}}$  contaminant species as a solid ( $\text{m}^3$ ) and  $\rho_n$  is the solid density of the  $n^{\text{th}}$  contaminant species ( $\text{g}/\text{m}^3$ ). The porous volume occupied by each contaminant species  $v_n'$  ( $\text{m}^3$ ), including air-filled interparticle voids, can then be calculated according to:

$$v_n' = \frac{m_n}{\eta_n}, \quad \text{Eq. 5-21}$$

where  $\eta_n$  is the  $n^{\text{th}}$  contaminant species' bulk density ( $\text{g}/\text{m}^3$ ). The porous volume occupied by the entire multi-contaminant film can then be estimated by summing all the porous volumes occupied by each contaminant species, according to:

$$V_T' = \sum_{n=1}^N v_n' = \sum_{n=1}^N \frac{m_n}{\eta_n}, \quad \text{Eq. 5-22}$$

where  $V_T'$  is the total film volume ( $\text{m}^3$ ) occupied by all contaminant species in powdered form, including their air-filled interparticle voids. The bulk density of the composite film  $\eta_T$  ( $\text{g}/\text{m}^3$ ) is required to estimate the height of the composite contaminant film,  $x_p$  (m), and can be estimated by dividing the total film's porous film mass by its porous volume:

$$\eta_T = \frac{m_p}{V_T'} = \frac{\sum_{n=1}^N m_n}{\sum_{n=1}^N v_n'}. \quad \text{Eq. 5-23}$$

The composite contaminant film height  $x_p$  (m) can then be estimated similar to **Eq. 5-4**:

$$x_p = \frac{m_p}{\eta_T dl}. \quad \text{Eq. 5-24}$$

Estimating the composite permittivity of the multi-contaminant film with Lichtenecker's mixture formula will again require each contaminant species' volume



fraction in the porous film as well as that of the air in the interparticle voids. The unitless volume fraction of particles in the  $n^{\text{th}}$  contaminant group  $\phi_n$  can be approximated by:

$$\phi_n = \frac{v_n}{V'_T} \quad \text{Eq. 5-25}$$

and the unitless volume fraction of air  $\phi_{air}$  in the porous multi-contaminant film can be found in a manner similar to Eq. 5-7:

$$\phi_{air} = 1 - \sum_{n=1}^N \phi_n = 1 - \sum_{n=1}^N \frac{v_n}{V'_T} \quad \text{Eq. 5-26}$$

such that the total porous contaminant film volume is unity, according to:

$$\phi_{air} + \sum_{n=1}^N \phi_n = \phi_{air} + \sum_{n=1}^N \frac{v_n}{V'_T} = 1 \quad \text{Eq. 5-27}$$

The effective permittivity of the multi-contaminant film can then be estimated with Lichtenecker's equation by inserting  $\phi_{air}$ , the volume fractions of each contaminant  $\phi_n$  and their respective permittivities  $\epsilon_n$  into Eq. 5-5 and again solving for  $\epsilon_{eff}$ .

$$\epsilon_{eff} = e^{\phi_{air} \ln \epsilon_{air}} \prod_{n=1}^N e^{\phi_n \ln \epsilon_n} \quad \text{Eq. 5-28}$$

Finally, the total capacitance  $C$  (F) of all material occupying the analysis chamber volume can be calculated by inserting  $x_p$  and  $\epsilon_{eff}$  into Eq. 5-17.

## 5.5 Device Fabrication

Like the plasma spectroscopic sensor developed in Chapter 3, the capacitive sensor is intended to be a field portable device whose packaging materials must be suited to the variety of conditions likely to be experienced in environmental testing situations. The sensor's substrate and electrode materials must be mechanically robust and ideally

corrosion resistant for optimal performance and reliability. Furthermore, inexpensive and easily machinable materials and simple, low cost fabrication processes are preferable.

For these reasons, borosilicate glass and copper foil were selected for the substrate and capacitor plate electrode materials, respectively. As described Section 3.4, borosilicate glass is an idea substrate for prototyping electronic sensing devices due to its machinability, low cost, insulating properties, and compatibility with most adhesives. While copper is a moderately expensive material and can be expected to corrode slowly over time, it is also ductile, machinable, features a high electrical conductivity, and can be soldered to for excellent electrical connections. Additionally, the degree of corrosion likely to be experienced with copper foils used in water diagnostic applications is expected to be negligible and unlikely to significantly impede capacitive analysis.

The fabrication process flow used to construct the first generation capacitive sensor prototype is described in **Figure 5-4**. First, the capacitor plate electrodes' glass substrates were cut to size and polished with a water saw and glass faceting machine, respectively (**Figure 5-4a**). The static and variable capacitor plate electrode dimensions were  $10.0\text{ mm} \times 15.0\text{ mm} \times 1.0\text{ mm}$  and  $10.0\text{ mm} \times 35.0\text{ mm} \times 1.0\text{ mm}$ , respectively. Next,  $4\text{ mm}^2$  square channels were etched into one end of each plate electrode by polymer masking and sandblasting. These channels served as a feedthrough conduit through which coaxial cabling connecting the device's capacitor plate electrodes and the capacitance measurement board could be established and secured. Mounting the coaxial cable wires within each electrode channel was found to provide a more secure and reliable electrical connection between the capacitor plate material and the capacitance measurement board, as opposed to soldering free-floating wires to each electrode.

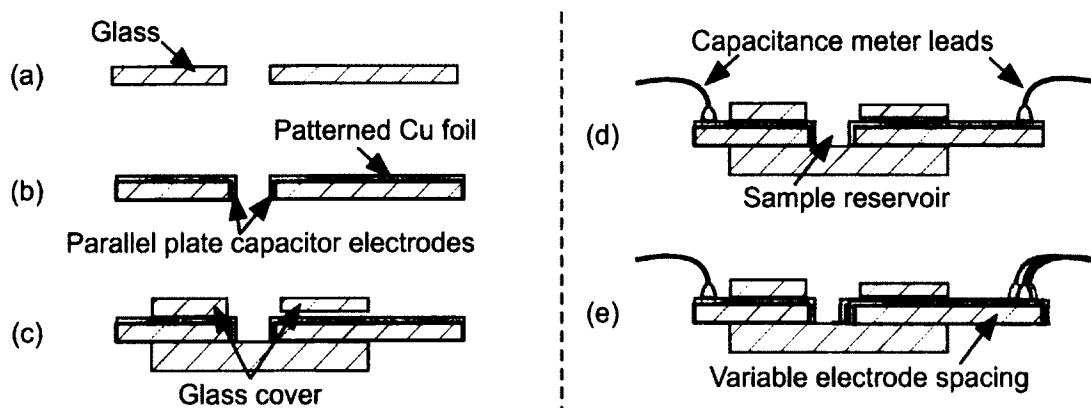


**Figure 5-4:** Fabrication process for the first generation capacitive sensor.

Next, a sheet of copper foil was then patterned over one of the front faces and the top surface of each electrode to function as the “plate” of a parallel plate capacitor (**Figure 5-4b**). After adhering the patterned copper foil to the electrode substrate with epoxy, a 4 mm wide channel was cut into the foil on the electrode’s top surface and the excess copper material was removed to minimize the plate electrode’s fringe capacitance contribution between the plate face and the capacitance board connection. Then, one electrode was positioned between two rectangular glass sheets that were adhered to the sensor’s substrate to function as a channel for the movable electrode and secured with epoxy (**Figure 5-4c**). Two additional rectangular glass sheets, functioning as covers to secure both electrodes to the device, were positioned and secured with epoxy.

Finally, the signal channel leads of two miniature SMB cables were stripped and connected to each plate electrode (via the 4 mm<sup>2</sup> channel) with solder and secured with an additional coating of epoxy (**Figure 5-4d**). Each SMB cables’ ground channel wires were connected and soldered to a jumper wire that was then connected to the ground terminal of an electrical wall outlet during capacitive analysis. In this arrangement, the capacitor plate electrode was not secured to the substrate and allowed to be moved in and

out of its glass channel housing, to vary the device's baseline capacitance (**Figure 5-4e**). The total material cost for the first generation capacitive sensing device was estimated to be approximately \$5.00.

## 5.6 Experimental Setup

All capacitance measurements were made with an off-chip AD7745/46EBZ 24-bit capacitance-to-digital evaluation board (Analog Devices, Inc., Norwood, MA), a laptop computer, and the proprietary interface software included with the evaluation board. The experimental setup consisting of the first generation capacitive sensor prototype, capacitance measurement board, and cabling, is shown in **Figure 5-5**.

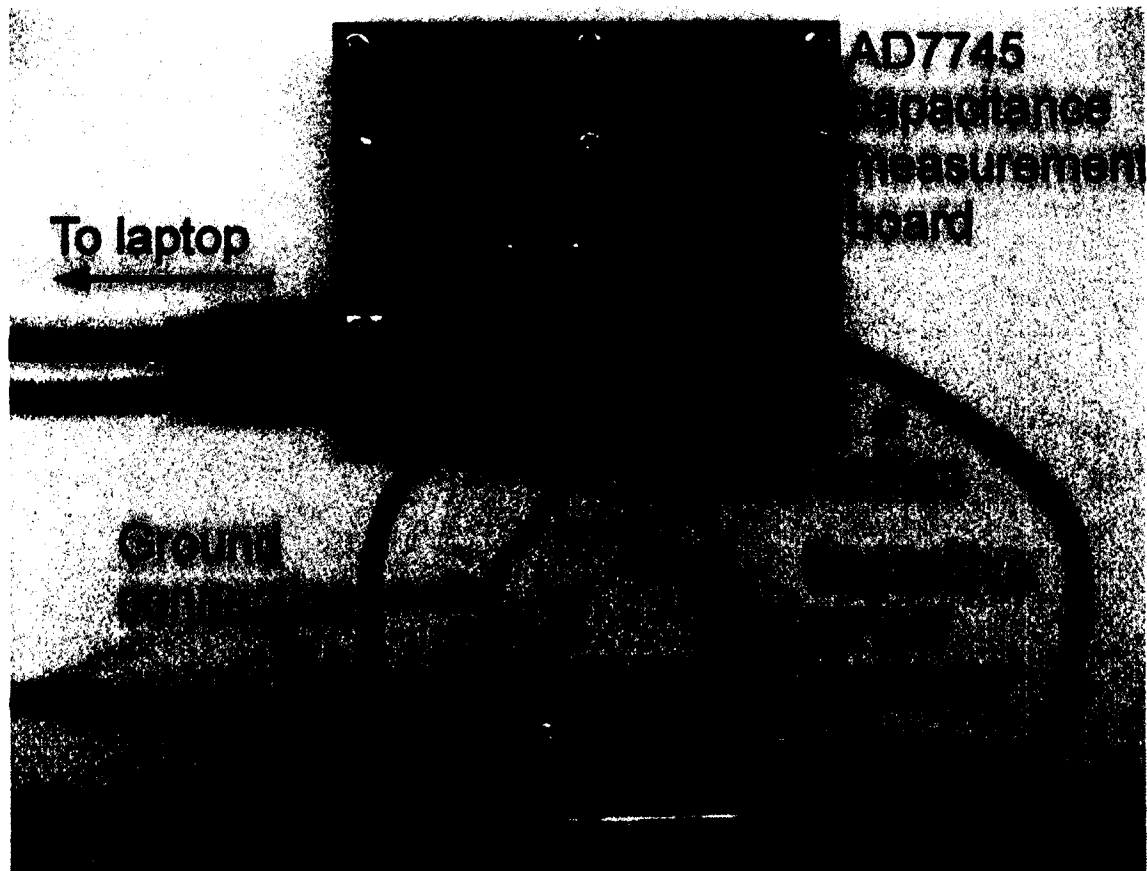


**Figure 5-5:** Experimental setup used to calibrate and test the capacitive sensor.

The AD7745/46EBZ evaluation board features a maximum common-mode (unchanging) capacitance measurement of up to 17 pF with a resolution of 4 aF (minimum measurable capacitance value), an accuracy of 4 fF, and linearity of 0.01% [58]. User-defined software parameters for each capacitive measurement included a 11.0 ms conversion time for the single-ended channel (*i.e.* only one capacitor device was connected to the board) with a capacitance sampling rate of 90 Hz. All experimental capacitance values reported in this work were averaged from 100 capacitance samples of a single contaminant film sample.

#### 5.6.1 Sensor Calibration

The numerical concentration models do not account for the device's fringe capacitance, which all real capacitors exhibit due to the electric field lines extending around the sensor's plate faces. Therefore, the experimental baseline capacitances were anticipated to be greater than those predicted by the numerical model and the difference between each value was assumed to represent the fringe capacitance of the device for a given plate spacing. Calibration of the capacitive sensor prototype's output consisted of measuring this fringe capacitance offset for each spacing distance and adding this value as a correction factor within the numerical model.

The first step in calibrating the prototype was to model the sensor's theoretical baseline capacitance at each plate spacing (0.59, 1.0, 1.59, 2.0, 2.59, 3.0, and 3.59 mm). To do so, the single contaminant numerical concentration-to-capacitance model was configured to simulate the capacitance of a generic contaminant with a concentration of zero. In this manner, the model simulated the capacitance of the analysis chamber when filled with air only. This arrangement represented the device's baseline capacitance

output as a function of each plate separation distance and the lowest capacitance measurement possible for each spacing configuration. Next, a set of 0.59 and 1.00 mm glass spacers were selected to set the proper electrode distance for calibration and testing.

The baseline capacitance of the sensor with no contaminants was then measured at each electrode spacing with the AD7745 evaluation board. These results were then compared with measurements taken with a Keithley electrical probe and capacitance measurement station, located in Louisiana Tech's Institute for Micromanufacturing characterization laboratory. All experimental capacitance values measured with the Keithley system were averaged from 41 samples. The simulated and experimental capacitances recorded with each measurement device are illustrated in **Figure 5-6**.

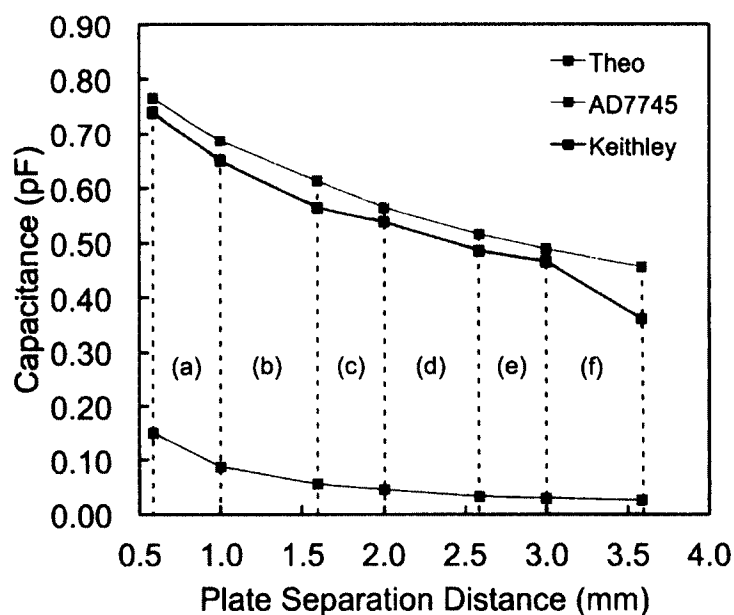


**Figure 5-6:** Calibration results for each plate spacing.

The capacitance values measured with the Keithley and AD7745 devices were found to be in close agreement and their capacitances, as a function of plate spacing, matched the general capacitance trend predicted by the numerical model. The

unexpectedly lower capacitance value measured by the Keithley station at  $d=3.59$  mm is likely due to the prototype's baseline capacitance at this spacing approaching or falling below the minimum capacitance measurement value of the Keithley machine, as evidenced by the high variance between the minimum/maximum values recorded at this capacitor plate separation distance.

Initially, the fringe capacitance contribution to the total measured capacitance was expected to be approximately equal for each electrode separation distance. In reality, however, the fringe offset between the capacitance predicted by the numerical model and the capacitance experimentally measured with the AD7745 board ranged from 0.615735 pF for the 0.59 mm spacing to 0.430931 pF for the 3.59 mm spacing, with an average offset of 0.523597 pF. The capacitance offset between the theoretical model and that measured by the Keithley electrical probe station was slightly lower, ranging from 0.562388 pF for the 0.59 mm spacing to 0.335812 pF for the 3.59 mm spacing, with an average offset of 0.465092 pF.

The data from this calibration experiment was also useful for determining the ideal electrode separation for optimal agreement between the theoretical model and the capacitive sensor prototype/AD7745 board output. By comparing the slopes of lines connecting each point in the AD7745 and theoretical data sets in **Figure 5-6**, it was possible to identify which electrode spacing region had the greatest linearity, and therefore greatest agreement, between the numerical model and experimental results, as summarized in **Table 5-2**. The electrode spacing region between 0.59 and 1.00 mm (highlighted in blue in **Table 5-2** and region "a" in **Figure 5-6**) provided the greatest agreement between the slopes of the theoretically predicted and experimental measured

baseline capacitance trend lines, with a difference of 0.043541 pF/mm. The region with the second-best theoretical/experimental agreement was the 2.59/3.00 mm spacing, varying by 0.047286 pF/mm. However, because the 0.59/1.00 mm region provided both the greatest theoretical/experimental capacitance agreement *and* the highest baseline capacitance, these two plate spacings were selected for characterizing the prototype's performance. Relevant theoretical and experimental capacitance data for the 0.59 and 1.00 mm plate spacing regions are highlighted in blue in **Table 5-3**.

**Table 5-2:** Calibration results used to determine optimal plate separation distance.

| Region | Plate Spacing,<br>$d$ (mm) | Theoretical Slope<br>(pF/mm) | Experimental Slope<br>(pF/mm) | Difference (Abs)<br>(pF/mm) |
|--------|----------------------------|------------------------------|-------------------------------|-----------------------------|
| b      | 1.00/1.59                  | -0.055715                    | -0.121887                     | 0.066172                    |
| c      | 1.59/2.00                  | -0.027859                    | -0.121259                     | 0.0934                      |
| d      | 2.00/2.59                  | -0.017102                    | -0.085299                     | 0.068197                    |
| e      | 2.59/3.00                  | -0.011402                    | -0.058688                     | 0.047286                    |
| f      | 3.00/3.59                  | -0.008226                    | -0.059061                     | 0.050835                    |

**Table 5-3:** Calibration/fringe capacitance results for each plate separation distance.

| Plate Spacing,<br>$d$ (mm) | Theoretical Capacitance (pF) | Experimental Capacitance (pF) | Fringe Capacitance (pF) |
|----------------------------|------------------------------|-------------------------------|-------------------------|
| 1.59                       | 0.055716                     | 0.614558                      | 0.558842                |
| 2.00                       | 0.044294                     | 0.564842                      | 0.520548                |
| 2.59                       | 0.034204                     | 0.514516                      | 0.480312                |
| 3.00                       | 0.029529                     | 0.490454                      | 0.460924                |
| 3.59                       | 0.024676                     | 0.455607                      | 0.430931                |

Finally, the fringe capacitance value for each plate separation distance could be added to **Eq. 5-16** and **Eq. 5-17** in the numerical concentration-to-capacitance model as a



correction factor to maximize agreement between model-simulated and experimentally measured results. This yielded a new total capacitance  $C$  equation for the capacitive analysis chamber volume defined by:

$$C = \frac{\epsilon_{eff} \epsilon_0 x_p l}{d} + \frac{\epsilon_{air} \epsilon_0 (h - x_p) l}{d} + C_{fringe}, \quad \text{Eq. 5-29}$$

where  $C_{fringe}$  (F) is the sensor prototype's fringe capacitance for a given plate spacing  $d$ . A fringe capacitance correction value of 0.615735 pF and 0.597883 pF were then added to Eq. 5-29 when modeling the capacitive sensor prototype's output at the 0.59 and 1.00 mm plate spacings, respectively.

## 5.7 Results

$\text{Al}_2\text{O}_3$ ,  $\text{SiO}_2$ , and  $\text{NaCl}$  contaminants were used to characterize the performance of the capacitive sensor prototype against theoretical capacitances predicted by the single and multi-contaminant versions of the numerical concentration model. The single contaminant model was evaluated at of 10, 5, 1, 0.5, and 0.1 g/L contaminant concentration levels. The multi-contaminant model was evaluated at contaminant concentrations of 10, 5, and 1 g/L, where four contaminant ratios (by mass) were investigated. Here, the ratio of each contaminant in the mixture is denoted by ( $A:N:S$ ), where  $A$  represents  $\text{Al}_2\text{O}_3$ ,  $N$  represents  $\text{NaCl}$ , and  $S$  represents  $\text{SiO}_2$ . The dominant contaminant species in a mixture is denoted in data figures with an asterisk (\*). For example, the  $\text{Al}_2\text{O}_3$  dominant ( $\text{Al}_2\text{O}_3^*$ ) mixture ratio is denoted as 2:1:1.

To begin testing, high purity powdered samples of each contaminant material and at each concentration level were prepared to contain the appropriate mass of particles that would be contained in a 1 mL liquid water sample for a given contaminant concentration.

The powdered samples were then manually added to the capacitive analysis chamber with the device's plate separation distance set to 1.00 mm using the glass spacers. Efforts were made to arrange the contaminant sample particles in the analysis chamber base as a film with a uniform height and density, in order for the film's geometry to match the rectangular profile simulated by the numerical concentration-to-capacitance model.

After measuring the device's capacitance in the  $d=1.00$  mm configuration, the device's plate spacing was then set to the 0.59 mm configuration while the contaminant particles remained in the analysis chamber. In doing so, slight downward pressure was applied to the variable plate electrode to prevent contaminant particles from accumulating under the electrode as it moved. After reconfiguring the plate separation distance, the contaminant particles were again arranged to match the numerical model's idealized film with uniform height and density, as closely as possible.

The contaminant films were also prepared for each capacitance measurement with minimal particle compaction, in order to mimic the contaminant material's experimentally measured bulk density as closely as possible. The capacitance of the sample-loaded device was then measured with the sample reservoir/analysis chamber left exposed to the ambient air. No mechanism to shield ambient electromagnetic radiation was used for these tests.

The solid densities for all contaminants were obtained from their manufacturer's Material Safety Data Sheets [59] [44] [60] (Alfa Aesar, Ward Hill, MA) and their bulk densities were measured experimentally. Each contaminant material's relative permittivity value was obtained from a compilation paper published by the United States' National Bureau of Standards [61].

### 5.7.1 Single Contaminant Theoretical Predictions

The single contaminant concentration-to-capacitance model was simulated in MATLAB for each contaminant species, at each contaminant concentration level, and for each capacitor plate separation distance. The relevant physical parameters entered into the numerical concentration-to-capacitance model for each contaminant species are summarized in the first three data columns of **Table 5-4**. The model's simulated physical parameters of the air/contaminant composite film are listed in the last three data columns of **Table 5-4**. As shown in the last column, the air-filled voids comprised the majority of the simulated volume occupied by each contaminant film, with air content approaching approximately  $\frac{2}{3}$  of the  $\text{Al}_2\text{O}_3$  and  $\text{SiO}_2$  film volume and over  $\frac{1}{2}$  of the NaCl film volume. The model's porosity estimates were observed to be comparable to those measured in sand and clay soils reported in [62], where porosity estimates ranged from 41 to 92% for loosely packed materials. The relatively high volume fraction of air in each film also served to significantly reduce the effective permittivity of each composite material (**Eq. 5-8**), driving each composite film's permittivity toward the lower permittivity of air (1.00054) [45].

**Table 5-4:** Physical parameters of single contaminant porous films.

|                         | Density<br>$\rho_p$ (g/L) | Bulk<br>Density<br>$\eta_p$ (g/L) | Ordinary<br>Permittivity<br>$\epsilon_R$ | Effective<br>Permittivity<br>$\epsilon_{eff}$ | Particle<br>Volume<br>Fraction<br>$\phi_p$ | Air<br>Volume<br>Fraction<br>$\phi_{air}$ |
|-------------------------|---------------------------|-----------------------------------|--|---|--|---|
| $\text{Al}_2\text{O}_3$ | 3.97                      | 1.32                              | 10.07                                    | 2.16  | 0.333                                      | 0.667                                     |
| $\text{SiO}_2$          | 2.65                      | 0.91                              | 4.53                                     | 1.67  | 0.343                                      | 0.657                                     |
| NaCl                    | 2.17                      | 0.92                              | 5.9                                      | 1.12  | 0.422                                      | 0.578                                     |

The numerical model's effective permittivity predictions for each composite film were also observed to remain constant as a function of impurity concentration. This can

be explained as a consequence of the application of Lichtenecker's effective permittivity calculation (Eq. 5-8) to films containing only one contaminant species and air. Here, each material's intrinsic permittivity is constant, as is the volume fraction occupied by each material, which is calculated as a function of the contaminant material's fixed density and bulk density, according to Eq. 5-6 and Eq. 5-7. As all of the parameters used to calculate the porous materials effective permittivity are fixed,  $\epsilon_{eff}$  is independent concentration. Simulated single contaminant capacitance results for each contaminant, at each concentration, and each electrode spacing are illustrated graphically in Figure 5-7. As would be expected for a numerical model based on linear equations, the capacitance values for each data set predicted by Eq. 5-29 are linear and are proportional to its only independent variable  $x_p$ , which is in turn a function of the contaminant's concentration  $\beta_p$ , according to Eq. 5-3 and Eq. 5-4.

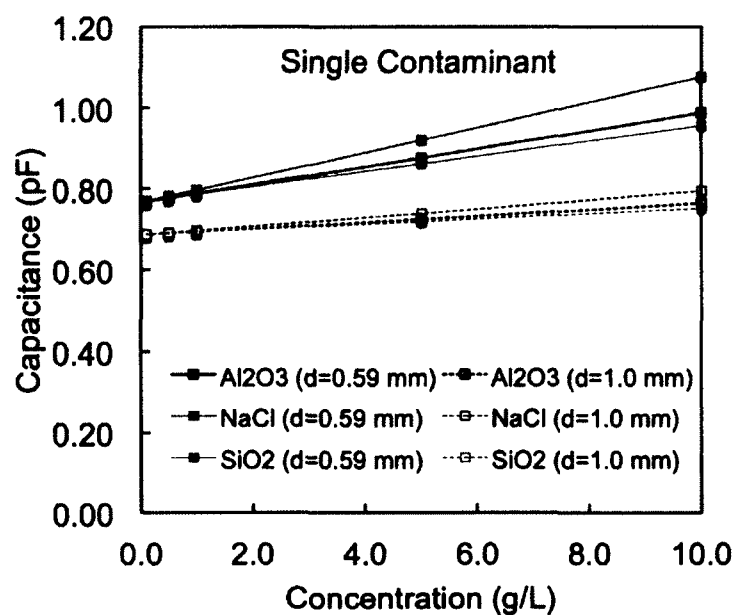


**Figure 5-7:** Simulated single contaminant capacitances for each electrode spacing.

The  $d=0.59$  mm data set also exhibits a greater capacitance range as a consequence of the reduced  $d$  value in Eq. 5-29. In general, a greater capacitance range would be favorable because a greater range requires less precise measurements to experimentally distinguish between the capacitance of one contaminant concentration and another. The 0.59 mm data set range spans 0.307804 pF, with maximum/minimum capacitances of 1.075588 and 0.767784 pF, respectively, while the 1.00 mm data sets projected a more limited range of 0.107147 pF, with maximum/minimum capacitances of 0.794279 and 0.687133 pF, respectively.

Specific theoretical capacitance values for each contaminant, concentration, and plate spacing are given in their respective sections. A MATLAB template representing the single contaminant numerical model is provided in Appendix B.

### 5.7.2 Al<sub>2</sub>O<sub>3</sub> Capacitance Data

The theoretical capacitances and physical parameters of porous Al<sub>2</sub>O<sub>3</sub> contaminant films predicted by the numerical model are summarized in Table 5-5.

**Table 5-5:** Theoretical parameters of the Al<sub>2</sub>O<sub>3</sub> contaminant particle films.

|                  | Contaminant Concentration, $\beta_p$ (g/L) | Total Capacitance, $C$ (pF) | Film Capacitance, $C_p$ (pF) | Air Capacitance, $C_{air}$ (pF) | Film Thickness, $x_p$ ( $\mu$ m) |
|------------------|--|-----------------------------|------------------------------|---------------------------------|----------------------------------|
| <b>d=0.59 mm</b> | 10   | 0.372875                    | 0.41523                      | -0.042355                       | 1282.08                          |
|                  | 5  | 0.261512                    | 0.207615                     | 0.053897                        | 641.042                          |
|                  | 1  | 0.172421                    | 0.041523                     | 0.130898                        | 128.208                          |
|                  | 0.5  | 0.161285                    | 0.020762                     | 0.140524                        | 64.1042                          |
|                  | 0.1  | 0.152376                    | 0.004152                     | 0.148224                        | 12.8208                          |
| <b>d=1.0 mm</b>  | 10   | 0.166119                    | 0.144541                     | 0.021577                        | 756.43                           |
|                  | 5  | 0.127353                    | 0.072271                     | 0.055083                        | 378.215                          |
|                  | 1  | 0.096341                    | 0.014454                     | 0.081887                        | 75.643                           |
|                  | 0.5  | 0.092464                    | 0.007227                     | 0.085237                        | 37.8215                          |
|                  | 0.1  | 0.089363                    | 0.001445                     | 0.087918                        | 7.5643                           |

For the  $d=0.59$  mm capacitor plate separation distance and the  $\beta_p=10$  g/L contaminant concentration, the simulated capacitance of the rectangular air dielectric was observed to be negative, which is physically impossible and represents an error in the numerical concentration-to-capacitance model's predictions for this spacing and concentration configuration. This discrepancy indicates that the simulated contaminant film height,  $x_p$ , exceeds the height  $h$  of the real capacitive device's sample reservoir/parallel-plate capacitor at the 10 g/L concentration, when utilizing the experimentally measured  $\text{Al}_2\text{O}_3$  bulk density  $\eta_{\text{Al}_2\text{O}_3}$ . Stated differently, the model predicts that the rectangular  $\text{Al}_2\text{O}_3$  contaminant dielectric volume to be larger than the volume of the sample analysis chamber housing it and that the capacitance of the rectangular air dielectric is improperly accounted for. Because the capacitance of the air dielectric  $C_{air}$  in the twin capacitor parallel network (Eq. 5-16) is a function of its height,  $h-x_p$ , when  $x_p$  exceeds  $h$ ,  $C_{air}$  becomes negative.

For the  $d=0.59$  mm and  $\beta_p=10$  g/L configuration, the concentration-to-capacitance model overestimated the contaminant film height  $x_p$  by 282 microns, resulting in a capacitive error of approximately 42 fF for the air dielectric. This discrepancy was observed for both plate spacings in all other single contaminant data sets at the 10 g/L concentration except here, where it was limited to the 0.59 mm separation distance only. A similar discrepancy was observed in the multiple contaminant simulations at the 10 g/L concentration for all  $d=0.59$  mm data sets and all but one  $d=1.00$  mm data set.

Theoretical and experimental capacitance values for  $\text{Al}_2\text{O}_3$  contaminant films at each concentration level and at the 0.59 and 1.00 mm plate spacings are illustrated graphically in **Figure 5-8** and **Figure 5-9**, respectively.

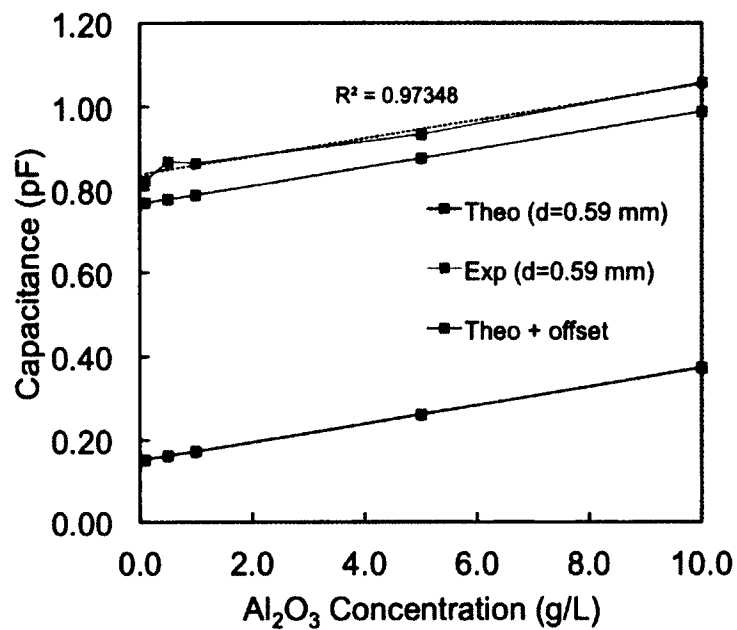


**Figure 5-8:** Theoretical and experimental results for Al<sub>2</sub>O<sub>3</sub> films,  $d=0.59$  mm.

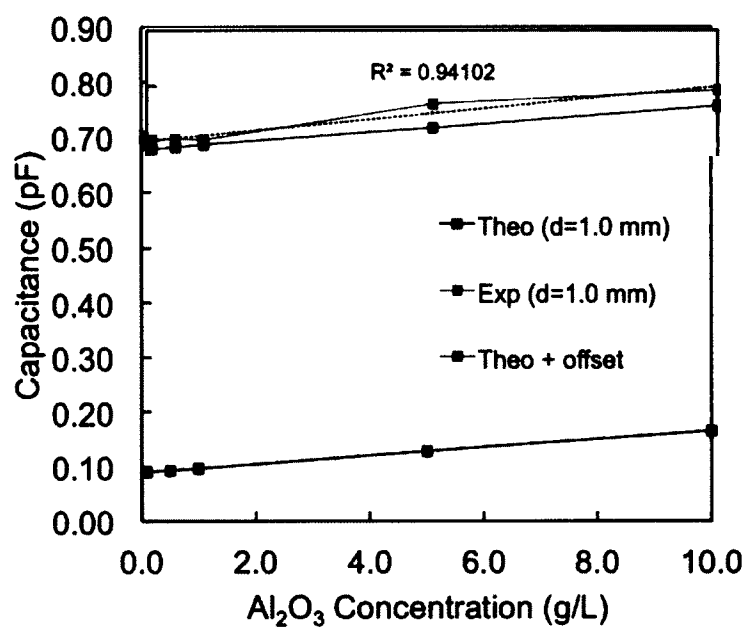


**Figure 5-9:** Theoretical and experimental results for Al<sub>2</sub>O<sub>3</sub> films,  $d=1.0$  mm.

Both experimental data sets exhibited a high degree of linearity with contaminant concentration, with the 0.59 mm spacing having the greatest linearity between data sets. (The dash line represents the experimental data trendline). As a pollutant's concentration in the sample increases, any errors in the derivation of the numerical model's method of accounting for the contaminant film's dielectric properties will be magnified and the divergence between theoretical and experimental capacitances can also be expected to increase with concentration. For example, in the  $d=1.0$  mm data set, the error between simulated and experimental capacitance values tended to increase with contaminant concentration beginning with the 1.0 g/L concentration. Overall, though, both data sets showed good agreement between the numerical model capacitance predictions and experimentally measured capacitances.

For the  $d=0.59$  mm data set, the error between the simulated concentration-to-capacitance values and experimental capacitances remained approximately equal for all concentrations except 0.5 g/L. Here, the unexpectedly higher experimental capacitance concentration may be due to the plate separation distance  $d$  being slightly less than 0.59 mm, which according to **Eq. 5-29** would increase the device's total capacitance. This kind of discrepancy is possible when utilizing a variable plate spacing mechanism that does not contain an effective "locking" feature to secure its configured position. In fact, for many tests the position of the variable plate electrode was observed to vary slightly after configuring the separation distance. This slight movement was observed to be the result of tension in the SMB cable connecting the plate electrode to the capacitance measurement board. This tension often caused the plate electrode to be either pushed into the device or pulled out of the device, in incremental distances.



**Table 5-6** below summarizes the error analysis results for the theoretical and experimental capacitance values for each of the  $\text{Al}_2\text{O}_3$  contaminant data sets. While both plate spacings showed good agreement between theory and experiment, contaminant concentrations measured with the 1.0 mm electrode spacing gave the lowest overall error. For the 1.0 mm plate separation, the highest and lowest theoretical versus experimental error was found to be 5.90115% for the 5 g/L concentration and 1.30546% for the 1 g/L concentration, respectively, with an average error of 3.00389%. For the 0.59 mm electrode spacing, the highest and lowest theoretical versus experimental error was found to be 11.7746% for the 0.5 g/L concentration and 6.46078% for the 5 g/L concentration, respectively, with an average error of 8.34355%.

**Table 5-6:** Theoretical and experimental data summary for  $\text{Al}_2\text{O}_3$  contaminants.

|                  | Contaminant Concentration, $\beta_p$ (g/L) | Theoretical Capacitance + Offset (pF) | Experimental Capacitance (pF) | Error    |
|------------------|--|---------------------------------------|-------------------------------|----------|
| <b>d=0.59 mm</b> | 10   | 0.988610                              | 1.05768                       | 6.98612% |
|                  | 5  | 0.877247                              | 0.933924                      | 6.46078% |
|                  | 1  | 0.788156                              | 0.863307                      | 9.53495% |
|                  | 0.5  | 0.77702                               | 0.868512                      | 11.7746% |
|                  | 0.1  | 0.768111                              | 0.821582                      | 6.96126% |
| <b>d=1.0 mm</b>  | 10   | 0.7640024                             | 0.7919609                     | 3.65948% |
|                  | 5  | 0.7252364                             | 0.7680337                     | 5.90115% |
|                  | 1  | 0.6942243                             | 0.7032871                     | 1.30546% |
|                  | 0.5  | 0.6903478                             | 0.7037954                     | 1.94795% |
|                  | 0.1  | 0.6872465                             | 0.7024033                     | 2.20544% |

### 5.7.3 NaCl Capacitance Data

The theoretical capacitances and physical parameters of for NaCl contaminant films predicted by the numerical model, as a function of NaCl concentration and all capacitor plate spacings, are summarized in **Table 5-7**.

**Table 5-7:** Theoretical parameters of the NaCl contaminant particle films.

|                                       | Contaminant<br>Concentration,<br>$\beta_p$ (g/L) | Total<br>Capacitance,<br>$C$ (pF) | Film<br>Capacitance,<br>$C_p$ (pF) | Air<br>Capacitance,<br>$C_{air}$ (pF) | Film<br>Thickness,<br>$x_p$ ( $\mu\text{m}$ ) |
|---------------------------------------|--|-----------------------------------|------------------------------------|---------------------------------------|---|
| <b>d=</b><br><b>0.59</b><br><b>mm</b> | 10   | 0.459853                          | 0.587531                           | -0.127678                             | 1850.34                                       |
|                                       | 5  | 0.305001                          | 0.293766                           | 0.011235                              | 925.172                                       |
|                                       | 1  | 0.181119                          | 0.058753                           | 0.122366                              | 185.034                                       |
|                                       | 0.5  | 0.165634                          | 0.029377                           | 0.136257                              | 92.5172                                       |
|                                       | 0.1  | 0.153246                          | 0.005875                           | 0.147371                              | 18.5034                                       |
| <b>d=</b><br><b>1.0</b><br><b>mm</b>  | 10   | 0.196396                          | 0.20452                            | -0.008124                             | 1091.7  |
|                                       | 5  | 0.142492                          | 0.10226                            | 0.040232                              | 545.852                                       |
|                                       | 1  | 0.099369                          | 0.020452                           | 0.078917                              | 109.17  |
|                                       | 0.5  | 0.093978                          | 0.010226                           | 0.083752                              | 54.5852                                       |
|                                       | 0.1  | 0.089666                          | 0.002045                           | 0.087621                              | 10.917  |

As with the  $d=0.59$  mm  $\text{Al}_2\text{O}_3$  data set in the previous section, the numerical model's simulated capacitance of the rectangular air dielectric is negative at the 10 g/L concentration, but now for both capacitor plate spacing data sets. For the 0.59 mm and 1.00 mm plate capacitor spacings, the simulated contaminant film height  $x_p$  was predicted to exceed the 1.00 mm reservoir chamber height  $h$  by 850 and 91 microns, respectively. However, this discrepancy's effect on the  $d=1.0$  mm theoretical results was minimal, as the error accounts for only 8 fF, which is on the order of the minimum measurable capacitance of the AD7745 board. Stated differently, the magnitude of this theoretical error is on the order of the capacitance measurement device's noise floor and, in this case, is can therefore be reasonably ignored. However, the error for  $d=0.59$  mm spacing at 10 g/L is much more significant, accounting for over 0.12 pF.

Theoretical and experimental capacitance values for NaCl contaminant films at each concentration and at 0.59 and 1.00 mm plate spacings are illustrated graphically in **Figure 5-10** and **Figure 5-11**, respectively.

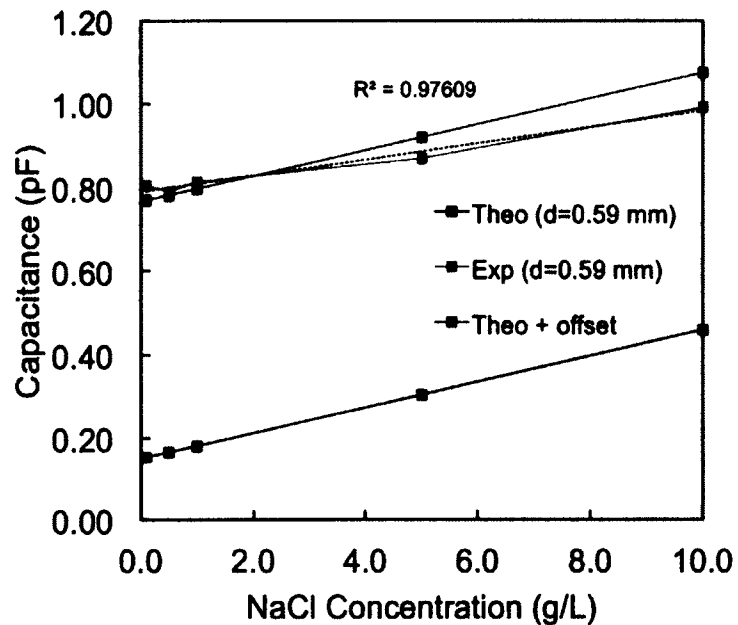


Figure 5-10: Theoretical and experimental results for NaCl films,  $d=0.59$  mm.

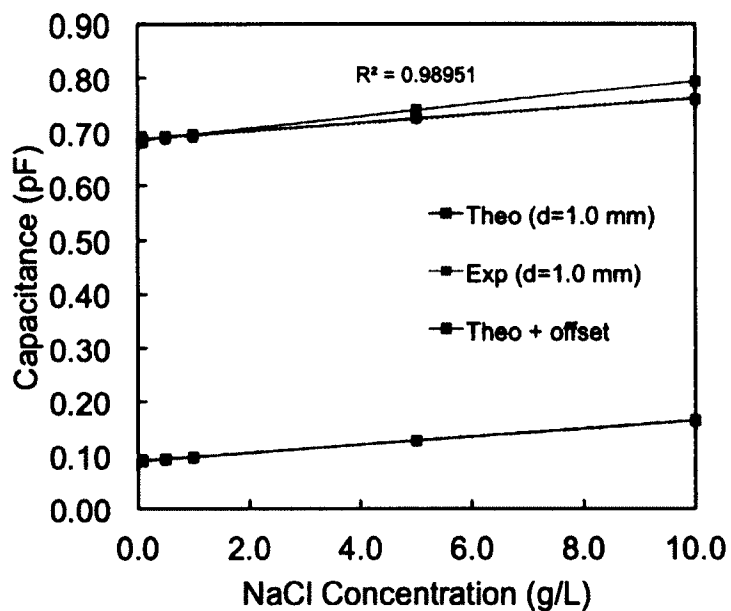


Figure 5-11: Theoretical and experimental results for NaCl films,  $d=1.0$  mm.

Again, both capacitor plate spacing data sets exhibit excellent experimental linearity and display reasonable agreement between theoretical and experimental values, with the  $d=1.0$  mm plate spacing providing the best overall agreement. The  $d=1.0$  mm data set showed excellent agreement in the 0.1 to 1 g/L concentration range, after which the theoretical versus experimental error increased with concentration. The  $d=0.59$  mm data set displayed a less favorable agreement between 0.1 and 1 g/L, which then increased at a greater rate with concentration, compared to the  $d=1.0$  mm data set. **Table 5-8** summarizes the error analysis for the theoretical and experimental results for each of the NaCl contaminant data sets.

**Table 5-8:** Theoretical and experimental data summary for NaCl contaminants.

|                  | Contaminant Concentration, $\beta_p$ (g/L) | Theoretical Capacitance + Offset (pF) | Experimental Capacitance (pF) | Error     |
|------------------|--|---------------------------------------|-------------------------------|-----------|
| <b>d=0.59 mm</b> | 10   | 1.07559                               | 0.991696                      | 7.79964%  |
|                  | 5  | 0.920736                              | 0.869341                      | 5.582%    |
|                  | 1  | 0.796854                              | 0.813368                      | 2.07239%  |
|                  | 0.5  | 0.781369                              | 0.788590                      | 0.924083% |
|                  | 0.1  | 0.768981                              | 0.80435                       | 4.59937%  |
| <b>d=1.0 mm</b>  | 10   | 0.794279                              | 0.760322                      | 4.27521%  |
|                  | 5  | 0.740375                              | 0.727015                      | 1.8046%   |
|                  | 1  | 0.697252                              | 0.695673                      | 0.226417% |
|                  | 0.5  | 0.691862                              | 0.692195                      | 0.048232% |
|                  | 0.1  | 0.687549                              | 0.682115                      | 0.790431% |

For the  $d=1.0$  mm electrode spacing, the highest and lowest theory/experiment error was found to be 4.27521% for the 10 g/L concentration and 0.048232% for the 0.5 g/L concentration, respectively, with an average error of 1.42898%. For the 0.59 mm electrode spacing, the highest and lowest theory/experiment error was found to be

7.79964% for the 10 g/L concentration and 0.924083% for the 0.5 g/L concentration, respectively, with an average error of 4.1955%.

#### 5.7.4 SiO<sub>2</sub> Capacitance Data

Theoretical capacitances and physical parameters for SiO<sub>2</sub> contaminant films, as a function of concentration and for all plate spacings, are summarized in **Table 5-9**. The negative  $C_{air}$  capacitance discrepancy was again observed in the numerical model's predictions for SiO<sub>2</sub> films at both plate spacings for  $\beta_p=10$  g/L. Here, the numerical model overshoot the contaminant film height  $x_p$  by 866 and 101 microns for the 0.59 and 1.00 mm plate separation distances, respectively. Both errors were similar in magnitude to those observed in the NaCl data set, with a minimal error of approximately 9 fF for  $d=1.0$  mm and a much more significant error for  $d=0.59$  mm at over 0.13 pF.

**Table 5-9:** Theoretical parameters of the SiO<sub>2</sub> contaminant particle films.

|                  | Contaminant Concentration, $\beta_p$ (g/L) | Total Capacitance, $C$ (pF) | Film Capacitance, $C_p$ (pF) | Air Capacitance, $C_{air}$ (pF) | Film Thickness, $x_p$ ( $\mu$ m) |
|------------------|--|-----------------------------|------------------------------|---------------------------------|----------------------------------|
| <b>d=0.59 mm</b> | 10   | 0.340208                    | 0.470334                     | -0.130126                       | 1866.65                          |
|                  | 5  | 0.245178                    | 0.235167                     | 0.010011                        | 933.323                          |
|                  | 1  | 0.169155                    | 0.047033                     | 0.122121                        | 186.665                          |
|                  | 0.5  | 0.159652                    | 0.023517                     | 0.136135                        | 93.3323                          |
|                  | 0.1  | 0.152049                    | 0.004703                     | 0.147346                        | 18.6665                          |
| <b>d=1.0 mm</b>  | 10   | 0.154747                    | 0.163723                     | -0.008976                       | 1101.32                          |
|                  | 5  | 0.121668                    | 0.081862                     | 0.039806                        | 550.661                          |
|                  | 1  | 0.095204                    | 0.016372                     | 0.078831                        | 110.132                          |
|                  | 0.5  | 0.091896                    | 0.008186                     | 0.083710                        | 55.0661                          |
|                  | 0.1  | 0.089249                    | 0.001637                     | 0.087612                        | 11.0132                          |

Theoretical and experimental capacitance values for SiO<sub>2</sub> contaminant films, as a function of contaminant concentration, and at all capacitor plate spacings are illustrated in **Figure 5-12** and **Figure 5-13**, respectively.

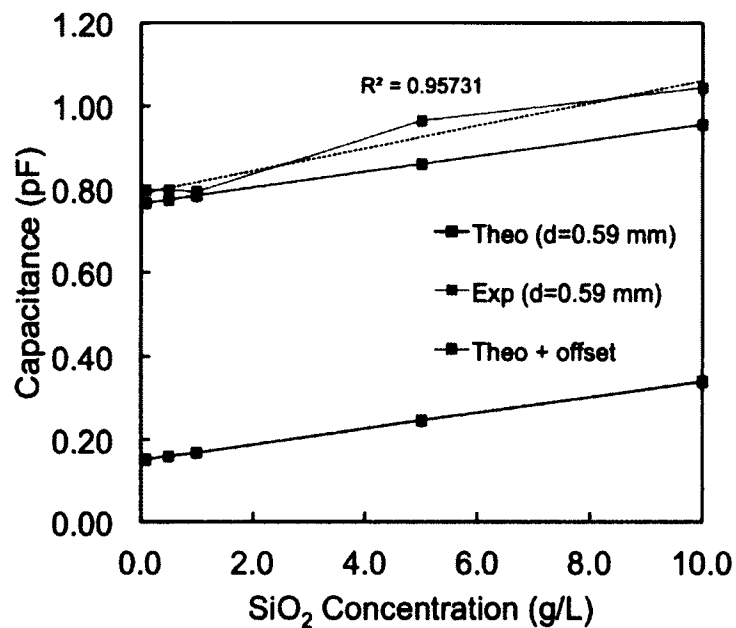


Figure 5-12: Theoretical and experimental results for SiO<sub>2</sub> films,  $d=0.59$  mm.

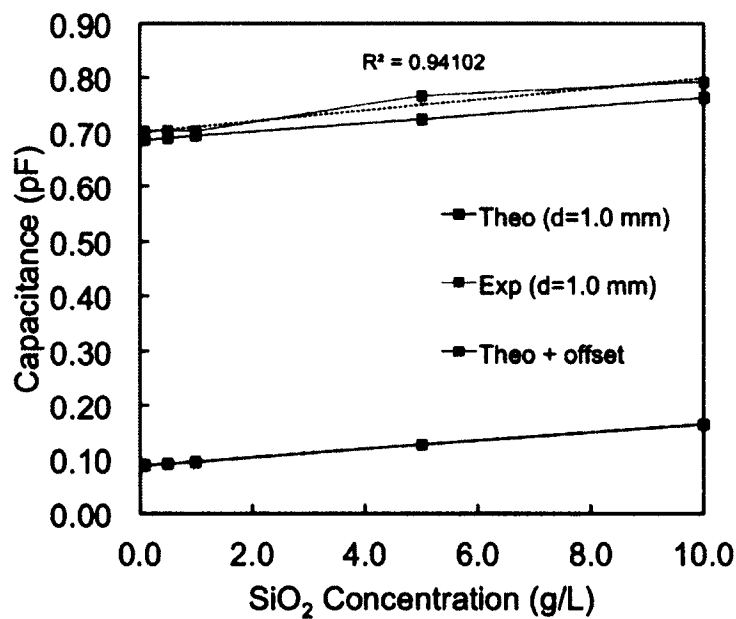


Figure 5-13: Theoretical and experimental results for SiO<sub>2</sub> films,  $d=1.0$  mm.

Both experimental data sets exhibited high linearity. The  $d=1.00$  mm data set demonstrated good agreement between theory and experiment while that of the  $d=0.59$  mm spacing was much poorer. The divergence between the simulated and experimentally measured capacitance values tended to increase with contaminant concentration, with the divergence increasing more rapidly with concentration for the  $d=0.59$  mm data set. **Table 5-10** summarizes the error analysis for the theoretical and experimental capacitance results for the  $\text{SiO}_2$  data sets.

**Table 5-10:** Theoretical and experimental data summary for  $\text{SiO}_2$  contaminants.

|                  | Contaminant Concentration, $\beta_p$ (g/L) | Theoretical Capacitance + Offset (pF) | Experimental Capacitance (pF) | Error     |
|------------------|--|---------------------------------------|-------------------------------|-----------|
| <b>d=0.59 mm</b> | 10   | 0.955943                              | 1.04447                       | 9.26074%  |
|                  | 5  | 0.860913                              | 0.964067                      | 11.9819%  |
|                  | 1  | 0.784890                              | 0.794185                      | 1.18422%  |
|                  | 0.5  | 0.775387                              | 0.799000                      | 3.04528%  |
|                  | 0.1  | 0.767784                              | 0.798206                      | 3.96222%  |
| <b>d=1.0 mm</b>  | 10   | 0.752630                              | 0.795470                      | 5.69201%  |
|                  | 5  | 0.719551                              | 0.770944                      | 7.14228%  |
|                  | 1  | 0.693087                              | 0.690584                      | 0.361239% |
|                  | 0.5  | 0.689779                              | 0.679158                      | 1.53984%  |
|                  | 0.1  | 0.687133                              | 0.706433                      | 2.80874%  |

Once again, contaminant concentrations measured with the 1.0 mm electrode spacing gave the lowest error between theory and experiment. For the 1.0 mm electrode spacing, the highest and lowest theory/experiment error was found to be 7.14228% for the 5 g/L concentration and 0.361239% for the 1 g/L concentration, respectively, with an average error of 3.50882%. For the 0.59 mm electrode spacing, the highest and lowest theory/experiment error was found to be 11.9819% for the 5 g/L concentration and 1.18422% for the 1 g/L concentration, respectively, with an average error of 5.88687%.

### 5.7.5 Multiple Contaminant Theoretical Predictions

As with the single contaminant model, the multi-contaminant concentration-to-capacitance model was simulated in MATLAB for each contaminant mixture and at each capacitor plate spacing for 10, 5, and 1 g/L concentrations. The density, bulk density, and ordinary dielectric constant parameters for each contaminant used in the model were the same as those listed in **Table 5-4**. The simulated volume fractions for each contaminant species in each mixture ratio and each mixture's theoretical composite permittivity values are shown in **Table 5-11**.

**Table 5-11:** Multi-contaminant mixture concentration model parameters.

|  | Equal<br>Contaminant<br>Mixture | Al <sub>2</sub> O <sub>3</sub><br>Dominant<br>Mixture | NaCl<br>Dominant<br>Mixture | SiO <sub>2</sub><br>Dominant<br>Mixture |
|--|---------------------------------|---|-----------------------------|---|
| Al <sub>2</sub> O <sub>3</sub><br>Volume Fraction,<br>$\phi_{Al_2O_3}$ | 0.085402                        | 0.135940  | 0.062331                    | 0.062183                                |
| NaCl<br>Volume Fraction,<br>$\phi_{NaCl}$                              | 0.156242                        | 0.124351  | 0.228068                    | 0.113763                                |
| SiO <sub>2</sub><br>Volume Fraction,<br>$\phi_{SiO_2}$                 | 0.128038                        | 0.101904  | 0.093449                    | 0.186455                                |
| Air<br>Volume Fraction,<br>$\phi_{air}$                                | 0.630317                        | 0.637805  | 0.616152                    | 0.637599                                |
| Effective<br>Permittivity, $\epsilon_{eff}$                            | 1.95098                         | 1.99167   | 1.99427                     | 1.87304                                 |

In a manner similar to the film parameters simulated by the single contaminant model, the theoretical volume fraction of air in each multi-contaminant film approached  $\frac{2}{3}$  of the film's total volume. As with the single contaminant model, the multi-contaminant model's porosity predictions were comparable to that of loosely packed soils



discussed in [62]. However, the volume fractions of each contaminant species and air in the equal contaminant mixture (1:1:1) was observed to *not* add up to unity, as would be expected, but to 0.999999 instead. This data set is highlighted in red font in **Table 5-11**. This volume fraction discrepancy occurred despite the  $A$ ,  $N$ , and  $S$  ratios in the multi-contaminant model (**Eq. 5-18**) for the equal contaminant mixture being set to exactly  $\frac{1}{3}$  in the MATLAB m-file, which employs a repeating decimal for fractional values.

As shown in the last row of **Table 5-11**, the effective composite permittivity  $\epsilon_{eff}$  for each contaminant mixture converged to approximately 1.9. This convergence of composite permittivity values can be seen as the consequence of two factors, including:

- (1) The high simulated volume fraction of air in the films for each mixture ratio; and
- (2) The relatively small variance in each contaminant species' simulated volume fraction over all mixture ratios.

First, as observed with numerical model's simulated single contaminant film parameters in **Table 5-4**, the high volume fraction of air in each mixture resulted in its intrinsically lower permittivity value dominating **Eq. 5-29** over the much higher permittivities of the three contaminant species and, here again, driving down each mixture ratio's composite permittivity value. Secondly, because each contaminant species' theoretical volume fraction changed relatively little between each mixture ratio, the influence of the contaminants' larger permittivity values, such as that of  $\text{Al}_2\text{O}_3$  (10.07), were reduced further in the numerical model's effective permittivity calculation (**Eq. 5-28**).

All theoretical capacitances predicted by the numerical multi-contaminant capacitance-to-concentration model for each capacitor plate spacing, for all contaminant mixture ratios, and for all contaminant concentration levels are shown graphically in

**Figure 5-14.** As before, the numerical model's capacitance values for each data set are linear but now exhibit a capacitance reduced range compared to the capacitance range predicted by the single contaminant model. Here too, the NaCl-dominant mixture was observed to have a slightly greater capacitance range for both plate spacings. The  $d=0.59$  mm data set range spans 0.232883 pF, with a maximum and minimum capacitance of 1.02124 and 0.788358 pF, respectively. The  $d=1.00$  mm data set spans a more limited range of 0.081067 pF, with a maximum and minimum capacitance value of 0.775361 and 0.694294 pF, respectively. In fact, the  $d=1.0$  mm data set capacitances are virtually identical between the 1 and 5 g/L concentrations and show very little variance between 5 and 10 g/L. The near-identical capacitance versus concentration lines for all mixtures in both capacitor plate spacing data sets can be seen as a result of each mixture having a near-identical effective permittivity and similar air and particle volume fractions.

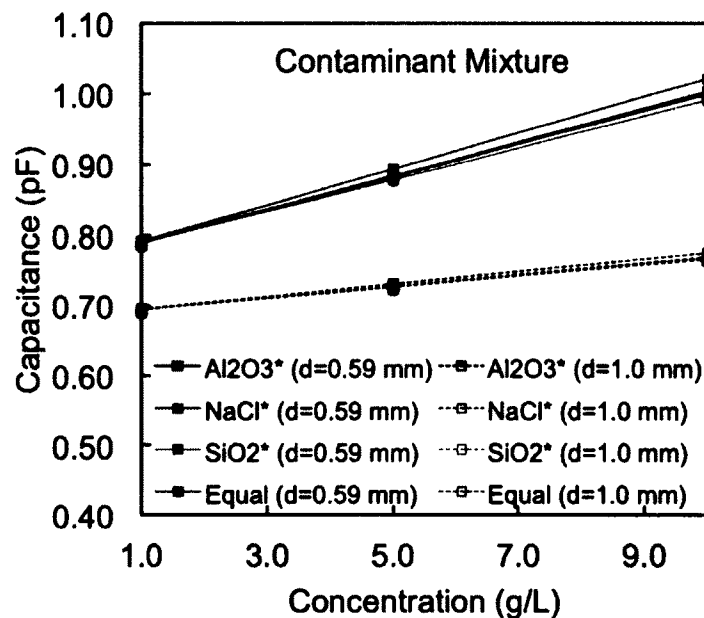


**Figure 5-14:** Multi-contaminant theoretical capacitances for each electrode spacing.

Specific theoretical capacitance values for each contaminant mixture and each capacitor plate spacing are given in their respective sections. A MATLAB template for the multi-contaminant model is provided in Appendix C.

#### 5.7.6 Equal Contaminant Mixture Capacitance Data

The theoretical capacitances and physical parameters simulated by the numerical multi-contaminant model for contaminant films containing an equal proportion of each contaminant species by mass are summarized in **Table 5-12**. As observed in the single contaminant predictions for NaCl and SiO<sub>2</sub> films, the multi-contaminant numerical model's simulated capacitance contribution for the rectangular air dielectric was negative for the 10 g/L concentration at both capacitor plate spacings. For the  $d=0.59$  mm capacitor plate spacing, the numerical model overshoot the contaminant film thickness by 866 microns, leading to a significant error of over 0.13 pF. The  $d=1.0$  mm film thickness error was considerably lower (approximately 1 micron), leading to a minimal capacitance error of approximately 9 fF. Theoretical and experimental capacitance data for the equal contaminant mixture films at each concentration level and capacitor plate spacing are illustrated in **Figure 5-15** and **Figure 5-16**.

**Table 5-12:** Theoretical parameters of the equal contaminant mixture films.

|                                       | Contaminant<br>Concentration,<br>$\beta_p$ (g/L) | Total<br>Capacitance,<br>$C$ (pF) | Film<br>Capacitance,<br>$C_p$ (pF) | Air<br>Capacitance,<br>$C_{air}$ (pF) | Film<br>Thickness,<br>$x_p$ ( $\mu$ m) |
|---------------------------------------|--|-----------------------------------|------------------------------------|---------------------------------------|--|
| <b>d=</b><br><b>0.59</b><br><b>mm</b> | 10   | 0.387824                          | 0.487876                           | -0.100053                             | 1866.65                                |
|                                       | 5  | 0.268986                          | 0.243938                           | 0.025048                              | 933.323                                |
|                                       | 1  | 0.173916                          | 0.048788                           | 0.125129                              | 186.665                                |
| <b>d=</b><br><b>1.0</b><br><b>mm</b>  | 10   | 0.171322                          | 0.16983                            | 0.001493                              | 1101.32                                |
|                                       | 5  | 0.129955                          | 0.084915                           | 0.04504                               | 550.661                                |
|                                       | 1  | 0.096861                          | 0.016983                           | 0.079878                              | 110.132                                |

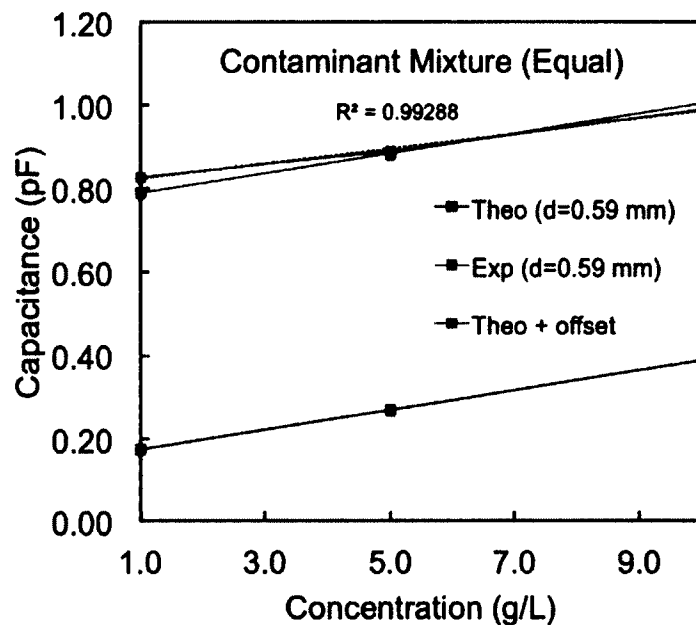


Figure 5-15: Theo/Exp data for equal contaminant mixture films,  $d=0.59$  mm.

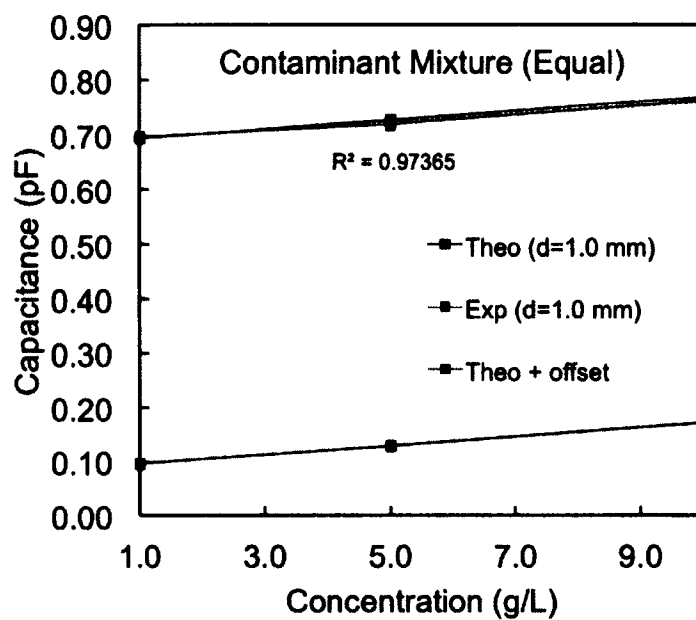


Figure 5-16: Theo/Exp data for equal contaminant mixture films,  $d=1.0$  mm.

Both data sets exhibit excellent experimental data linearity. Somewhat surprisingly, the agreement between simulated and experimentally measured capacitance values was generally much better for all contaminant mixture films than that of the single contaminant films. For the 0.59 mm equal contaminant mixture data set, the theory/experiment error was minimal between 5 and 10 g/L concentrations, with the 1 to 5 g/L concentration range showing a poorer agreement. For the  $d=1.0$  mm equal mixture data set, the simulated and experimentally measured capacitance values were nearly identical throughout the entire concentration range. **Table 5-13** summarizes the capacitive error analysis for the theoretical and experimental results for the equal contaminant mixture data sets.

**Table 5-13:** Theo/Exp data summary for equal mixture contaminants films.

|                  | Contaminant Concentration, $\beta_p$ (g/L) | Theoretical Capacitance + Offset (pF) | Experimental Capacitance (pF) | Error     |
|------------------|--|---------------------------------------|-------------------------------|-----------|
| <b>d=0.59 mm</b> | 10   | 1.00356                               | 0.988999                      | 1.45092%  |
|                  | 5  | 0.884721                              | 0.887889                      | 0.358011% |
|                  | 1  | 0.789651                              | 0.828403                      | 4.90742%  |
| <b>d=1.0 mm</b>  | 10   | 0.769205                              | 0.762773                      | 0.836253% |
|                  | 5  | 0.727838                              | 0.717944                      | 1.35938%  |
|                  | 1  | 0.694745                              | 0.698744                      | 0.575607% |

As with all single contaminant data sets previously discussed, the  $d=1.0$  mm capacitor plate spacing provided the greatest agreement between the numerical model capacitance predictions and experimental capacitance results. For the  $d=1.0$  mm capacitor plate spacing, the highest and lowest theory versus experimental error was found to be 1.35938% for the 5 g/L concentration and 0.575607% for the 1 g/L concentration, respectively, with an average error of 0.923747%. For the  $d=0.59$  mm electrode spacing,

the highest and lowest theory versus experimental error was found to be 4.90742% for the 1 g/L concentration and 0.358011% for the 5 g/L concentration, respectively, with an average error of only 2.23878%.

#### 5.7.7 Al<sub>2</sub>O<sub>3</sub>-Dominant Mixture Capacitance Data

The theoretical capacitances and physical parameters of the porous films simulated by the numerical multi-contaminant model for Al<sub>2</sub>O<sub>3</sub>-dominant (2:1:1) contaminant mixture films, as a function of total contaminant concentration and for all capacitor plate spacings, are summarized in **Table 5-14**.

**Table 5-14:** Theoretical parameters of the Al<sub>2</sub>O<sub>3</sub>-dominant mixture films.

|                  | Contaminant Concentration, $\beta_p$ (g/L) | Total Capacitance, $C$ (pF) | Film Capacitance, $C_p$ (pF) | Air Capacitance, $C_{air}$ (pF) | Film Thickness, $x_p$ ( $\mu\text{m}$ ) |
|------------------|--|-----------------------------|------------------------------|---------------------------------|---|
| <b>d=0.59 mm</b> | 10   | 0.383707                    | 0.469336                     | -0.085628                       | 1570.29                                 |
|                  | 5  | 0.266928                    | 0.234668                     | 0.032260                        | 785.145                                 |
|                  | 1  | 0.173505                    | 0.046934                     | 0.126571                        | 157.029                                 |
| <b>d=1.0 mm</b>  | 10   | 0.169890                    | 0.163376                     | 0.006514                        | 926.471                                 |
|                  | 5  | 0.129239                    | 0.081688                     | 0.047551                        | 463.235                                 |
|                  | 1  | 0.096718                    | 0.016338                     | 0.080380                        | 92.6471                                 |

For this simulation, the theoretical capacitance of the rectangular air dielectric  $C_{air}$  was only observed to be negative for the  $d=0.59$  mm capacitor plate spacing data set at the 10 g/L concentration level. Here, the numerical multi-contaminant model overestimated the Al<sub>2</sub>O<sub>3</sub>-dominant film height  $x_p$  by slightly more than 570 microns, leading to a fairly significant capacitance error of approximately 86 fF. The numerical model's theoretical and experimentally measured capacitance values for the Al<sub>2</sub>O<sub>3</sub>-dominant contaminant mixture films at each concentration and all capacitor plate spacings are illustrated in **Figure 5-17** and **Figure 5-18**, respectively.

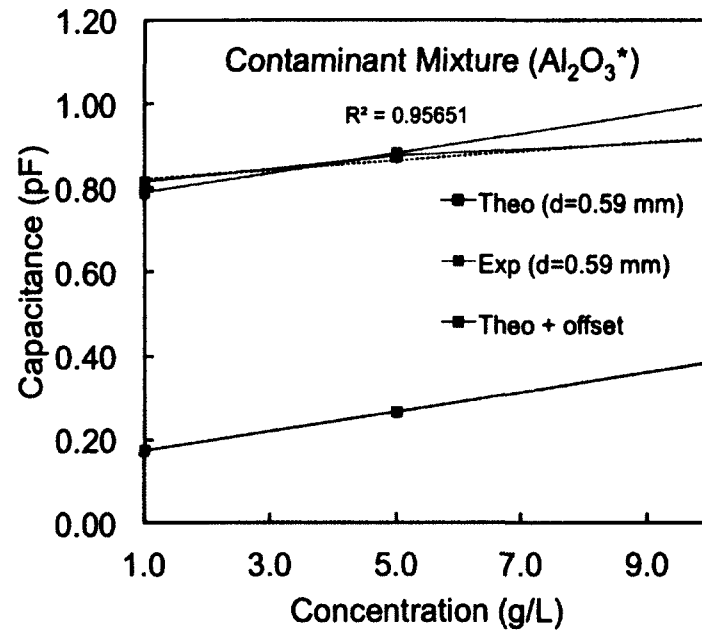


Figure 5-17: Theo/Exp data for  $\text{Al}_2\text{O}_3$ -dominant mixture films,  $d=0.59$  mm.

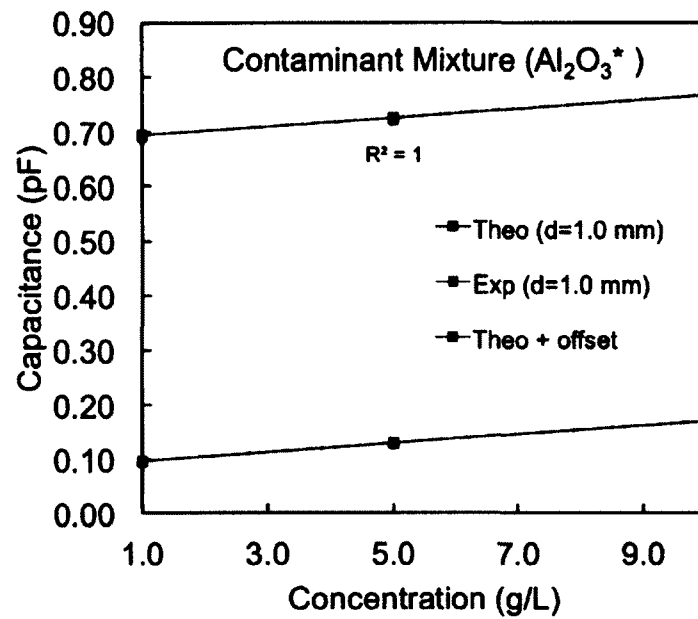


Figure 5-18: Theo/Exp data for  $\text{Al}_2\text{O}_3$ -dominant mixture films,  $d=1.0$  mm.

Here, both experimental data sets show excellent linearity, with the  $d=1.0$  mm capacitor plate spacing data set exhibiting an ideal linearity of 1. The  $d=0.59$  mm capacitor plate spacing data set showed reasonable theoretical versus experimental agreement between 1 and 5 g/L, but diverged rapidly after the 5 g/L concentration, here again, likely due to the variable plate electrode's spacing being compromised by tension in the SMB cabling connecting the capacitive sensor prototype to the measurement board. The  $d=1.0$  mm plate spacing data set, however, showed superior theoretical versus experimental agreement over the entire concentration range, with all model-simulated and experimental capacitance values being virtually indistinguishable. Error analysis results for the theoretically predicted and experimentally measured capacitance values of  $\text{Al}_2\text{O}_3$ -dominant mixture films are summarized in **Table 5-15**.

**Table 5-15:** Theo/Exp data summary for  $\text{Al}_2\text{O}_3$ -dominant mixture films.

|                  | Contaminant<br>Concentration,<br>$\beta_p$ (g/L) | Theoretical<br>Capacitance +<br>Offset (pF) | Experimental<br>Capacitance<br>(pF) | Error     |
|------------------|--|---|-------------------------------------|-----------|
| <b>d=0.59 mm</b> | 10   | 0.999442                                    | 0.913289                            | 8.62013%  |
|                  | 5  | 0.882663                                    | 0.876826                            | 0.661305% |
|                  | 1  | 0.789240                                    | 0.815435                            | 3.31899%  |
| <b>d=1.0 mm</b>  | 10   | 0.767773                                    | 0.767773                            | 3.40937%  |
|                  | 5  | 0.727122                                    | 0.727122                            | 0.819106% |
|                  | 1  | 0.694601                                    | 0.694601                            | 0.940338% |

The  $d=1.0$  mm capacitor plate spacing again provided the greatest agreement between the numerical model predictions and experimental results. Here, the theoretical and experimental results for the  $d=1.0$  mm spacing are nearly identical, as shown in the middle columns of **Table 5-15**. For the  $d=1.0$  mm electrode spacing, the highest and lowest theoretical versus experimental error was found to be 3.40937% for the 10 g/L



concentration and 0.819106% for the 5 g/L concentration, respectively, with an average error of only 1.72294%. For the  $d=0.59$  mm electrode spacing, the highest and lowest theory/experiment error was found to be 8.62013% for the 10 g/L concentration and 0.661305% for the 5 g/L concentration, respectively, with an average error of 4.20014%.

#### 5.7.8 NaCl-Dominant Mixture Capacitance Data

Theoretical capacitances and physical parameters simulated by the multi-contaminant model for the NaCl-dominant (1:2:1) contaminant mixtures, as a function of contaminant concentration and all plate spacings, are summarized in **Table 5-16**. In this simulation, the rectangular air dielectric  $C_{air}$  was observed to be negative at both capacitor plate spacings at the  $\beta_p=10$  g/L contaminant concentration level. For  $d=0.59$  mm, the model overestimated the film's thickness by 712 microns, resulting in a capacitance error of approximately 0.11 pF. For the  $d=1.0$  mm spacing, the model only overshoot the film thickness by 10 microns, leading to a negligible error of 0.9 fF. Theoretical and experimental capacitance values for the NaCl-dominant contaminant mixture films at all contaminant concentration levels and capacitor plate spacings are illustrated in **Figure 5-19** and **Figure 5-20**, respectively.

**Table 5-16:** Theoretical parameters of the NaCl-dominant mixture films.

|                  | Contaminant Concentration, $\beta_p$ (g/L) | Total Capacitance, $C$ (pF) | Film Capacitance, $C_p$ (pF) | Air Capacitance, $C_{air}$ (pF) | Film Thickness, $x_p$ ( $\mu\text{m}$ ) |
|------------------|--|-----------------------------|------------------------------|---------------------------------|---|
| <b>d=0.59 mm</b> | 10   | 0.405506                    | 0.512465                     | -0.106959                       | 1712.35                                 |
|                  | 5  | 0.277827                    | 0.256232                     | 0.021595                        | 856.177                                 |
|                  | 1  | 0.175685                    | 0.051247                     | 0.124438                        | 171.235                                 |
| <b>d=1.0 mm</b>  | 10   | 0.177478                    | 0.178389                     | -0.000912                       | 1010.29                                 |
|                  | 5  | 0.133033                    | 0.089195                     | 0.043838                        | 505.145                                 |
|                  | 1  | 0.097477                    | 0.017839                     | 0.079638                        | 101.029                                 |

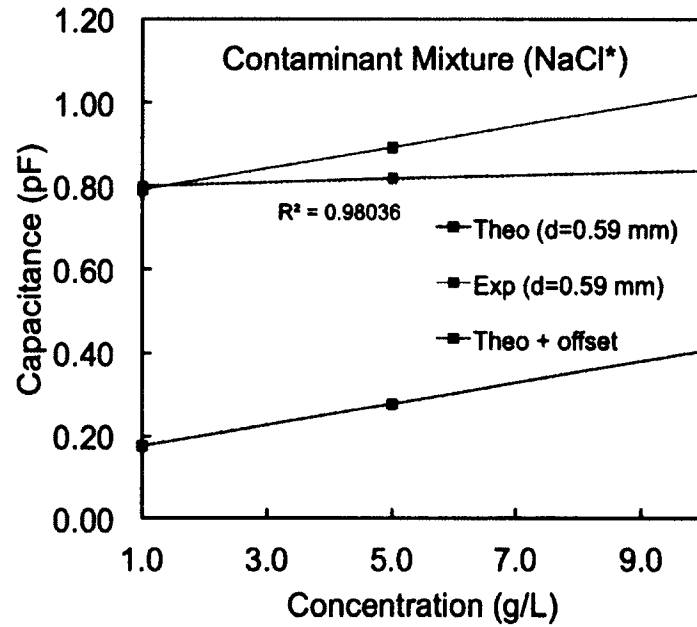


Figure 5-19: Theo/Exp data for NaCl-dominant mixture films,  $d=0.59$  mm.

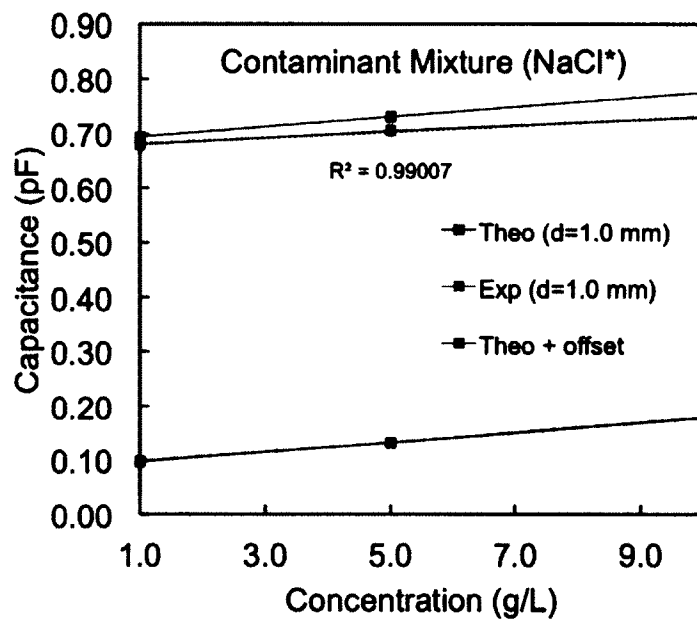


Figure 5-20: Theo/Exp data for NaCl-dominant mixture films,  $d=1.0$  mm.

Once again, both experimental data sets showed excellent linearity. As shown in **Figure 5-19**, the  $d=0.59$  data set only showed good theoretical versus experimental agreement at the 1 g/L concentration level, and rapidly diverged with increasing contaminant concentration. This data set's experimental capacitance range also showed a remarkably low capacitance range of 0.037 pF, which approached the capacitive noise floor of the measurement device. The  $d=1.0$  mm data set illustrated in **Figure 5-20** showed an improved but more modest agreement compared to the previously reported mixture data sets at this spacing. Here, the 1 g/L concentration showed a good theoretical/experimental agreement but diverged between 1 and 10 g/L concentrations. The results of an error analysis for the theoretically predicted and experimentally measured capacitance values for NaCl-dominant mixtures are summarized in **Table 5-17**.

**Table 5-17:** Theo/Exp data summary for NaCl-dominant mixture films.

|                  | Contaminant Concentration, $\beta_p$ (g/L) | Theoretical Capacitance + Offset (pF) | Experimental Capacitance (pF) | Error     |
|------------------|--|---------------------------------------|-------------------------------|-----------|
| <b>d=0.59 mm</b> | 10   | 1.02124                               | 0.835500                      | 18.1878%  |
|                  | 5  | 0.893562                              | 0.819611                      | 8.27598%  |
|                  | 1  | 0.791420                              | 0.798856                      | 0.939539% |
| <b>d=1.0 mm</b>  | 10   | 0.775361                              | 0.729810                      | 5.87485%  |
|                  | 5  | 0.730916                              | 0.706377                      | 3.35735%  |
|                  | 1  | 0.695360                              | 0.679849                      | 2.23066%  |

For the  $d=0.59$  mm capacitor plate spacing, the highest and lowest theoretical versus experimental error was found to be 18.1878% for the 10 g/L concentration (the highest error of all multi-contaminant data sets) and 0.939539% for the 1 g/L concentration, respectively, with an average error of 9.13445%. Theoretical versus experimental capacitance agreement was considerably better for the  $d=1.0$  mm capacitor

plate spacing, where the highest and lowest theory/experiment error was calculated to be 5.87485% for the 10 g/L concentration and 2.23066% for the 1 g/L concentration, respectively, with an average error of 3.82095%.

#### 5.7.9 SiO<sub>2</sub>-Dominant Mixture Capacitance Data

The theoretical capacitances and physical porous film parameters simulated by the numerical multi-contaminant model for the SiO<sub>2</sub>-dominant (1:1:2) mixture films, as a function of contaminant concentration and all plate spacings, are summarized in **Table 5-18**. The multi-contaminant model's capacitance for the rectangular air dielectric was again observed to be negative at 10 g/L, for both plate spacings. For the 0.59 mm spacing, the model overestimated the film thickness by slightly more than 716 microns, leading to an error of approximately 0.11 pF. For the 1.0 mm spacing, the model overestimated the contaminant film thickness by approximately 13 microns, resulting in a negligible error of 1.1 fF (less than the stated resolution of the measurement board). The theoretical and experimental capacitance values for the SiO<sub>2</sub>-dominant mixture films at each contaminant concentration and both capacitor plate spacings are illustrated in **Figure 5-21** and **Figure 5-22**, respectively.

**Table 5-18:** Theoretical parameters of the SiO<sub>2</sub>-dominant mixture films.

|                                       | Contaminant<br>Concentration,<br>$\beta_p$ (g/L) | Total<br>Capacitance,<br>$C$ (pF) | Film<br>Capacitance,<br>$C_p$ (pF) | Air<br>Capacitance,<br>$C_{air}$ (pF) | Film<br>Thickness,<br>$x_p$ ( $\mu$ m) |
|---------------------------------------|--|-----------------------------------|------------------------------------|---------------------------------------|--|
| <b>d=</b><br><b>0.59</b><br><b>mm</b> | 10   | 0.374889                          | 0.482461                           | -0.107571                             | 1716.43                                |
|                                       | 5  | 0.262519                          | 0.241230                           | 0.021289                              | 858.215                                |
|                                       | 1  | 0.172623                          | 0.048246                           | 0.124377                              | 171.643                                |
| <b>d=</b><br><b>1.0</b><br><b>mm</b>  | 10   | 0.166820                          | 0.167945                           | -0.001125                             | 1012.69                                |
|                                       | 5  | 0.127704                          | 0.083972                           | 0.043732                              | 506.347                                |
|                                       | 1  | 0.096411                          | 0.016795                           | 0.079617                              | 101.269                                |

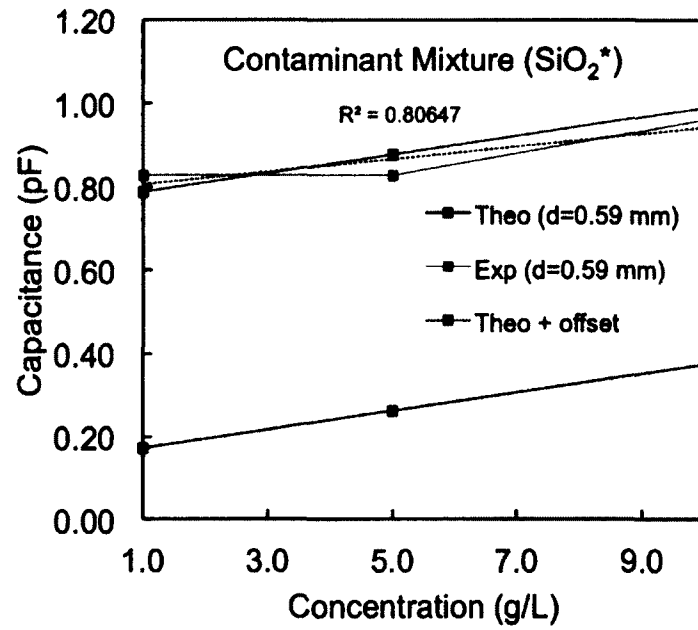


Figure 5-21: Theo/Exp data for SiO<sub>2</sub>-dominant mixture films,  $d=0.59$  mm.

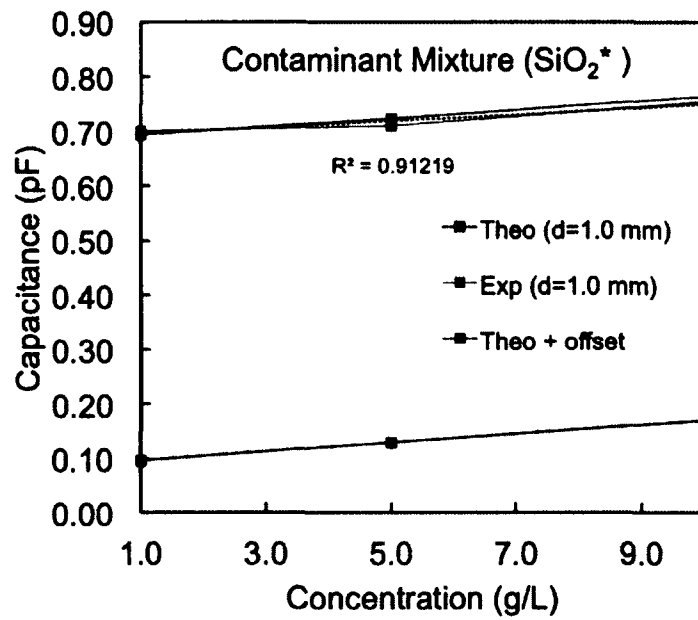


Figure 5-22: Theo/Exp data for SiO<sub>2</sub>-dominant mixture films,  $d=1.0$  mm.

As with the  $d=0.59$  mm data set for NaCl-dominant films, both experimental capacitance data sets in **Figure 5-21** and **Figure 5-22** for SiO<sub>2</sub>-dominant films showed poorer linearity than all other multi-contaminant data sets. In both cases, the non-linearity appears to be focused at the unexpectedly low experimental capacitance values at 5 g/L. This discrepancy could plausibly be the result of the SMB cable tension issue previously discussed, which may have increased the plate electrode's spacing, accounting for the low capacitance values at this concentration. Still, both data sets showed good overall agreement between theoretical and experimental capacitances, with the agreement of the  $d=1.0$  mm data set being significantly better than that of the 0.59 mm data set. Here, the simulated and experimentally measured capacitances were nearly identical at the 1 and 10 g/L concentrations and showed minimal divergence in between. The results of an error analysis for the theoretically predicted and experimentally measured capacitance values for SiO<sub>2</sub>-dominant mixtures are summarized in **Table 5-19**.

**Table 5-19:** Theo/Exp data summary for SiO<sub>2</sub>-dominant mixture films.

|                  | Contaminant Concentration, $\beta_p$ (g/L) | Theoretical Capacitance + Offset (pF) | Experimental Capacitance (pF) | Error    |
|------------------|--|---------------------------------------|-------------------------------|----------|
| <b>d=0.59 mm</b> | 10   | 0.990624                              | 0.959442                      | 3.1477%  |
|                  | 5  | 0.878254                              | 0.828171                      | 5.70255% |
|                  | 1  | 0.788358                              | 0.827559                      | 4.97246% |
| <b>d=1.0 mm</b>  | 10   | 0.764703                              | 0.754211                      | 1.3721%  |
|                  | 5  | 0.725587                              | 0.710286                      | 2.10882% |
|                  | 1  | 0.694294                              | 0.701343                      | 1.01519% |

As before, the  $d=1.0$  mm data set produced superior agreement between theory and experiment, with the highest and lowest error calculated to be 2.10882% for the 5 g/L concentration and 1.01519% for the 1 g/L concentration, respectively, with an average

error of only 1.4987%. For the 0.59 mm electrode spacing, the highest and lowest theory/experiment error was calculated to be 5.70255% for the 5 g/L concentration and 3.1477% for the 10 g/L concentration, respectively, with an average error of 4.60757%.

## 5.8 Discussion

Overall, the degree of agreement between the single and multi-contaminant numerical models and capacitive sensor data was very good, indicating that the capacitance-based impurity concentration measurement concept is a viable platform for analyzing a water contaminant's concentration in a MEMS-scale, field portable system. The following three sections summarize performance and experimental issues with the sensor, numerical concentration-to-capacitance models, and experimental setup and propose solutions to be implemented in the integrated diagnostic system's development.

### 5.8.1 Capacitive Sensor Design Issues

The primary design issue concerned the variable plate spacing mechanism. The spacing mechanism combined with tension in the SMB cable connecting the sensor to the measurement was found to make establishing a consistent capacitor plate distance across all capacitance tests problematic. This issue likely contributed to the less-than-unity experimental data linearity observed in most data sets. However, the spacing mechanism did accomplish the goal for which it was intended, which was to determine the capacitor plate spacing with produced the greatest agreement between theoretical and experimental data. The  $d=1.00$  mm capacitor plate spacing configuration consistently provided the lowest theoretical/experimental error and will be used exclusively in the second-generation embodiment. Finally, the second-generation sensor design should explore a "complementary" design for the channel connecting the capacitor plate electrode to the

SMB connection terminal to reduce the device's fringe capacitance. By situating these channels on opposite sides of the device, their contrasting electric field lines could potentially be used to minimize or eliminate the fringe offset.

### 5.8.2 Numerical Concentration-to-Capacitance Model Issues

The negative  $C_{air}$  capacitances observed in almost all data sets at the 10 g/L contaminant level suggests that the analysis chamber volume is simply too small to accommodate the quantity of contaminant particles at this concentration. For the second-generation device, the upper contaminant concentration limit will then be set to 5 g/L to ensure all theoretical capacitances and film height predictions are positive. In order to ensure sufficiently large data set to observe the film capacitance trend as a function of concentration, two additional contaminant concentrations will be investigated. An updated numerical concentration model should also explore the dielectric properties of oxides forming on the Cu capacitor plates and the extent to which these films could affect the theoretical versus experimental data agreement.

### 5.8.3 Experimental Setup Issues

The primary issue with the experimental setup was not attempting to account for the device's fringe capacitance by taking baseline samples of the empty device before introducing contaminant particles to the analysis chamber. In reality, the formation of oxide films or the accumulation of residue on the capacitor plate electrodes could vary the sensor's output with time to a significant degree. In this work, the constant fringe capacitance offset that calculated based on the device's benchmark capacitance in pristine condition can be seen as a less-than-ideal solution to this issue. In future work, baseline capacitance samples will be taken for each test and subtracted from the device's



capacitance when loaded with a contaminant sample in order to more effectively isolate the capacitance of the only the materials contained in the analysis chamber.

Additionally, all experimental capacitance data should be exported from the measurement board's software interface as a spreadsheet in order to compute the average, minimum, and maximum capacitance statistics for each data set. The experimental setup for the second-generation device should also explore shielding the sensor from ambient electromagnetic radiation with a Faraday cage-type device.

## 5.9 Conclusion

A parallel-plate capacitance-based sensing platform and numerical contaminant concentration-to-capacitance models were developed to identify the concentration of single and multiple contaminant species in a water sample. The first generation sensor prototype design included a mechanism to vary the capacitor plate separation distance in order to determine the optimal plate separation for maximum agreement between theoretical and experimental data.  $\text{Al}_2\text{O}_3$ ,  $\text{SiO}_2$ , and  $\text{NaCl}$  contaminants were measured singly at concentrations ranging from 10 to 0.1 g/L and four mixtures of each contaminant were measured between 10 and 1 g/L. Overall, the capacitance-based impurity concentration concept proved to be a viable method of characterizing a water contaminant's concentration in a miniaturized and field portable water diagnostic system.

## **CHAPTER 6**

### **INTEGRATED SENSING PLATFORM**

#### **6.1 Research Objectives**

This chapter discusses the design, fabrication, and testing of the final integrated water diagnostic device that incorporates updated embodiments of the plasma spectroscopic sensing platform, the capacitive sensing platform, and the numerical single contaminant concentration-to-capacitance model into a unified and field portable analysis system. The primary objective of this work was to implement the design modifications to each sensing platform and their experimental procedures proposed in their respective chapters during the development of the integrated water diagnostic system for improved functionality, sensitivity, and reliability.

#### **6.2 Design Considerations**

The following two subsections summarize the first generation plasma spectroscopic and capacitive sensing platforms' design and experimental procedure modifications proposed in Sections 3.7 and 5.8 and briefly describe how each modification was implemented into each sensing platform's second generation embodiment during development of the integrated diagnostic system. Design flaws and modifications to the single contaminant concentration-to-capacitance numerical model used in this work are discussed in greater detail in Section 6.4.

### 6.2.1 Plasma Spectroscopic Platform Modifications

The primary flaw in the first generation plasma spectroscopic sensor design was the use of thin metal films as the plasma discharge electrode material, which tended to quickly erode by sputtering. For the second-generation sensor, the plasma electrodes were separated from the on-chip microheater element and machined from bulk Ti foils into thin filaments. This electrode scheme provided a significantly longer device lifetime due to the greater quantity of electrode material and Ti's superior resistance to sputtering compared to Cr. Additionally, the more robust Ti electrodes maintained their sharp terminals, which produced a more consistent emission spectra profile over all data sets.

Regarding the updated spectral collection procedure, all spectral data were processed from ten samples. Baseline spectra were recorded for each contaminant test and a consistent orientation between a single fiber optic cable and the spectroscopic device was maintained throughout the entire testing phase. This arrangement allowed photon count statistics to be computed for any spectral line and ensured that the photon count scale between background and contaminant spectra would be consistent for easier discrimination of contaminant fragment lines from the background. Spectra were collected with the 1000 micron optical fiber and the spectrometer's integration time was increased to 1 s (from 300 ms) to increase the visibility of weaker fragment lines.

### 6.2.2 Capacitive Sensing Platform Modifications

The second-generation capacitive sensor's plate spacing was fixed at  $d=1.0$  mm to improve the linearity of experimental data as a function of contaminant concentration. The fixed spacing also ensured that the numerical model's analysis chamber dimensions

were consistent with those of the actual device for greater agreement between theoretical and experimental data. All other chamber/electrode dimensions were unchanged.

Concerning the capacitance data collection procedure, all capacitance data were processed from 100 capacitance samples of a single contaminated water sample and exported from the measurement board interface as a spreadsheet to perform a statistical analysis of each capacitance data set. A baseline data set was also recorded for each test prior to sample injection. For each data set, the average baseline capacitance was subtracted from the average contaminant film capacitance in an attempt to more accurately account for the device's fringe capacitance offset, contributed primarily from the Cu leads connecting the capacitor plates to the SMB connection at the device's edges.

### 6.3 Integrated Sensor Design

The integrated plasma spectroscopic and capacitive sensor design comprises three layers fabricated from glass and quartz substrates with Cr, Cu, and Ti materials for the sensing and water sample preconcentration elements, as illustrated in **Figure 6-1**. The top device layer (L3) features a 1 mL sample reservoir basin and particle inlet channel etched into a glass substrate (**Figure 6-1a**). The middle layer (L2) houses a 10  $\mu$ L rectangular sample analysis chamber with plasma spectroscopic and capacitive sensing elements (**Figure 6-1b**). The sample analysis chamber is assembled from five machined glass pieces, where two opposing walls of the chamber are patterned with Cu foil to serve as parallel plate capacitor electrodes. The Cu channels connecting the capacitor plates to the SMB cable contact points are also asymmetrically oriented along the device's horizontal axis to minimize the channel's fringe capacitance. Two Ti filaments are flush mounted in a microchannel etched perpendicular to the capacitor electrodes to function as plasma

discharge electrodes. The L3 particle inlet channel is oriented directly over the L2 analysis chamber to allow contaminant particles to aggregate in the chamber during preconcentration. The bottom layer (L1) features a thin film Cr microheater to preconcentrate the water sample (**Figure 6-1c**). Each layer is stacked in the appropriate order and bonded and water sealed with epoxy (**Figure 6-1d**).

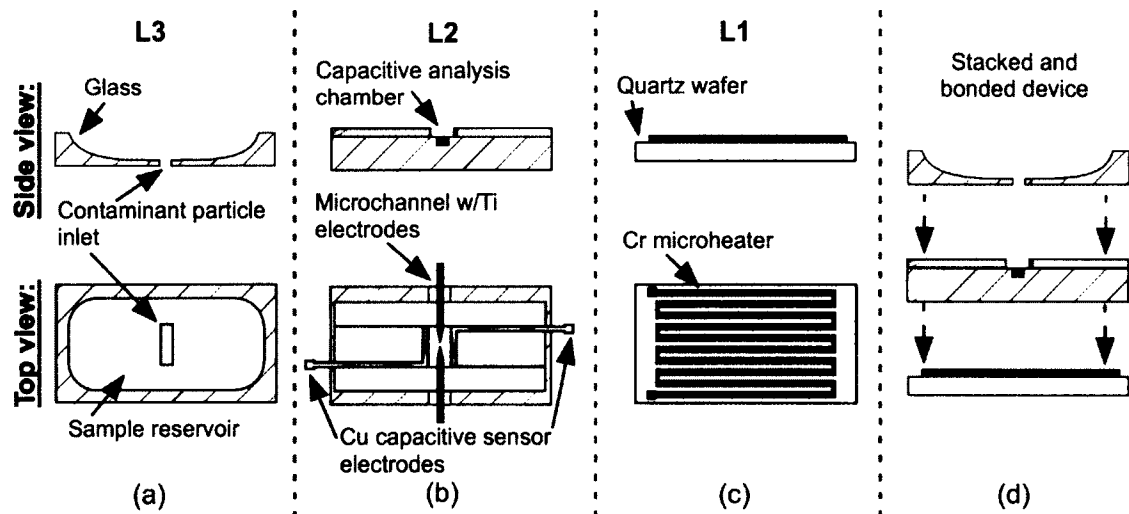


**Figure 6-1:** Three layer schematic of the integrated sensor prototype.

The integrated sensing device is utilized to identify a water contaminant's chemical composition and concentration using the two-phase electrochemical (plasma spectroscopic and capacitive) analysis process illustrated in **Figure 6-2**. First, a thin hydrophobic film is applied to the device's sample reservoir basin walls to limit contaminant particle stiction during the preconcentration stage and promote particle aggregation in the sample analysis chamber. Analysis begins by first recording 10 baseline spectra samples and 100 capacitance samples of the analysis chamber, when no contaminants are present and only air fills the chamber volume (**Figure 6-2a**). A high voltage DC bias is then applied to the Ti electrodes and the background spectra are

recorded an off-chip spectrometer and optical fiber. The analysis chamber's baseline capacitance is recorded with an off-chip capacitance measurement board.

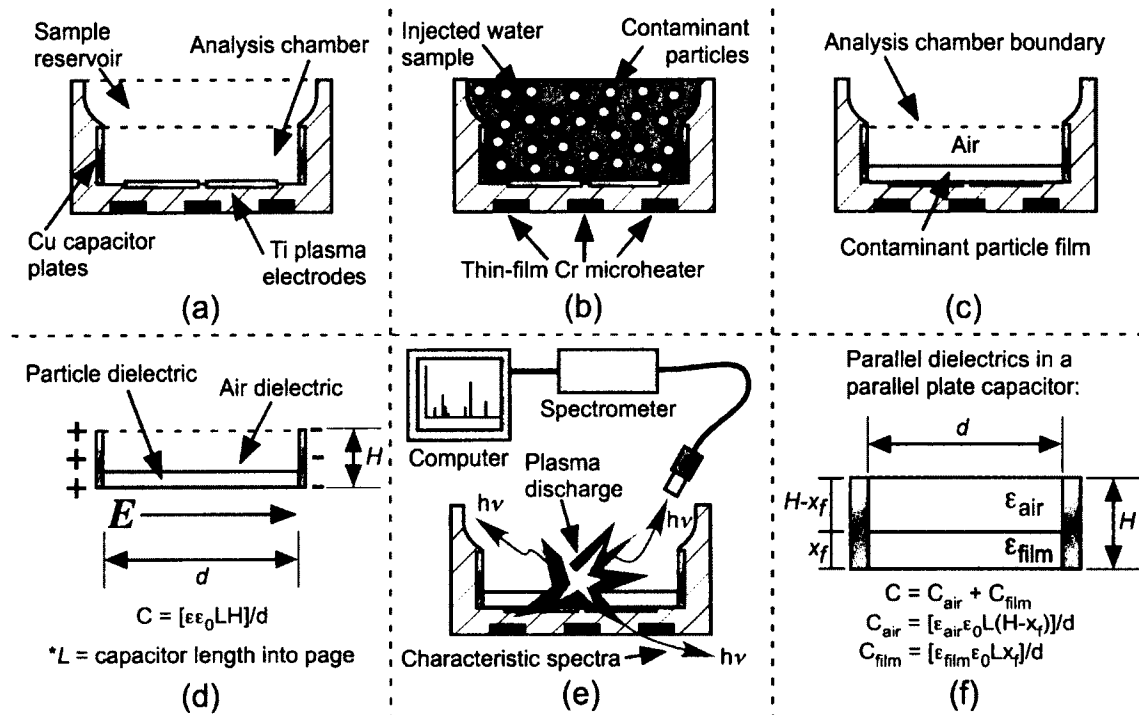


**Figure 6-2:** Capacitive/spectroscopic analysis procedure for the integrated device.

Next, a 1 mL water sample is injected into the device, filling the sample reservoir and analysis chamber (**Figure 6-2b**). Current is applied to the Cr microheater to preconcentrate the water sample as a porous contaminant particle film in the chamber base, in preparation for spectroscopic and capacitive analysis (**Figure 6-2c**). Here, the hydrophobic film supports the aggregation of contaminant particles into a film with uniform height and density over the entire chamber base. In this manner, the contaminant film and air space it above can be represented as two rectangular dielectric materials connected in parallel, as discussed previously in Sections 5.3 and 5.4. 100 samples of the analysis chamber's capacitance are recorded to preserve the original dielectric properties of the contaminant particles, which could be disturbed during the plasma spectroscopic

analysis (**Figure 6-2d**). The average capacitance of the contaminant data set is then subtracted from average capacitance of the baseline data set to isolate the capacitance of only the analysis chamber's contents.

A second DC bias voltage is then applied to the Ti electrodes and the contaminant's atomic and molecular fragment spectral lines are observed to identify its chemical composition, similar to the procedure discussed in Sections 3.3.3 and 3.5 (**Figure 6-2e**). Here, however, the discrimination of contaminant fragment lines is simplified by the superposition of representative spectra samples from the baseline and contaminant data sets. Furthermore, when a contaminant-exclusive spectral line is observed, the difference in the average photon counts for that line between the contaminant and baseline data sets is computed. The line's wavelength and average intensity are then compared to spectral data documented in reference texts to identify the contaminant with greater confidence. This statistical analysis of spectral data allows a contaminant line to be distinguished from background noise and is particularly helpful in observing contaminants with fragment lines that are inherently weak. Now identified, the contaminant's physical parameters can be used to characterize its concentration (**Figure 6-2f**) using the updated numerical concentration-to-capacitance model.

#### **6.4 Modified Single Contaminant Concentration Model**

The original single contaminant numerical concentration-to-capacitance model developed in Section 5.4.1 was modified for this work with three new features to provide a more realistic simulation of the contaminant film's capacitance, including:

- (1) A bulk density optimization method to maximize agreement between theoretical and experimental capacitance data;

- (2) An updated formulation of the Lichtenecker mixture equation to more accurately model the composite permittivity of a porous contaminant film; and
- (3) Consideration of the dielectric properties of Cu capacitor plate oxidation films.

The motivation behind each modification and the strategy used to implement them in the updated model is summarized in the following three sections.

#### 6.4.1 Bulk Density Optimization

A powdered material's bulk density is not an intrinsic quality and can vary widely with the degree of compaction and particle grain size. For example, a preconcentrated contaminant film's density in the analysis chamber base could vary according to the rate at which it is heat was applied to the water sample. The bulk density's upper bound, however, is limited by the material's density in the solid phase. The updated numerical concentration-to-capacitance model then considers the contaminant's bulk density as a "floating" variable to account for this variability in particle density and allow the model's theoretical capacitance's to be optimized to experimental data.

By following the single contaminant concentration-to-capacitance model derivation in Section 5.4.1 from Eq. 5-4 to Eq. 5-17, it can be seen that by treating the contaminant's bulk density variable  $\eta_p$  as an independent variable allows the slope of the model's theoretical capacitance versus concentration line to be reduced or increased to match that of an experimental data trendline. Therefore, the first step in the bulk density optimization process is to plot the experimental capacitance data set and impose a linear best-fit trendline through the data. This trendline is linear and not forced to zero at 0 g/L, in order to account for the empty chamber's non-zero air capacitance at this concentration, in agreement with Eq. 5-17.



Next, the model's bulk density parameter is varied and theoretical capacitances are computed for all contaminant concentrations in an iterative process until the theoretical capacitance versus concentration line and experimental trendline slope match to six decimal places (*i.e.* the AD7745 board capacitance resolution in pF). A reference bulk density for each contaminant was determined and used as a starting point in the iteration. With the theoretical and experimental trend lines' slopes now matched, the rate of change in the model's capacitance estimates as a function of impurity concentration will be identical to the experimental data. Any capacitance offset between the two lines can be accounted for with an offset capacitance, similar to that described in Section 5.6.1:

$$C = \frac{\epsilon_{eff}\epsilon_0 x_p l}{d} + \frac{\epsilon_{air}\epsilon_0 (h - x_p) l}{d} + C_{offset}, \quad \text{Eq. 6-1}$$

where  $C_{offset}$  (F) is the capacitive difference between the theoretical and experimental data sets. Because the slopes of both lines are matched,  $C_{offset}$  will be a constant.

#### 6.4.2 Modified Lichtenecker Equation

As discussed in Section 4.4.3, the original Lichtenecker mixture derivation was based on two faulty assumptions and has since been updated in [55] and [56] to better reflect the dielectric behavior of a composite material. Furthermore, when applied to the bulk density optimization process developed in the previous section, the original Lichtenecker mixture formulation was observed to yield nonsensical contaminant bulk densities that exceeded the contaminant material's solid density. For example, the "optimized" NaCl and MgO bulk densities were computed to be 12.52% and 78.34% greater than their respective solid phase densities. (NaCl: 2.4361 versus 2.165 g/cm<sup>3</sup> and MgO: 6.38473 vs. 3.58 g/cm<sup>3</sup>). The model's air and particle volume fractions for these

films were also observed to be unrealistic. After incorporating the new Lichtenecker mixture formulation, the optimized bulk densities were observed to be more realistic (*i.e.* less than the solid density), with air and particle volume fractions comparable to [62].

### 6.4.3 Capacitor Plate Oxides

The original numerical concentration-to-capacitance model derived in Section 5.4.1 assumed that the parallel capacitor plates were composed of pure Cu with no surface oxidation thins. However, a recent investigation into Cu oxidation patterns via X-ray absorption fine structure (XAFS) spectroscopy demonstrate that the surface of pure Cu film develops two thin oxidation layers after brief exposure (approximately 24 hours) to air at room temperature [63]. First, a  $\text{Cu}_2\text{O}$  film forms on the pure Cu surface that is then capped by a thin  $\text{CuO}$  film. Each film was measured to be 2.0 and 1.3 nm, respectively, on average. An updated representation of all dielectric materials in the capacitive analysis chamber based on this new data is illustrated in **Figure 6-3**.

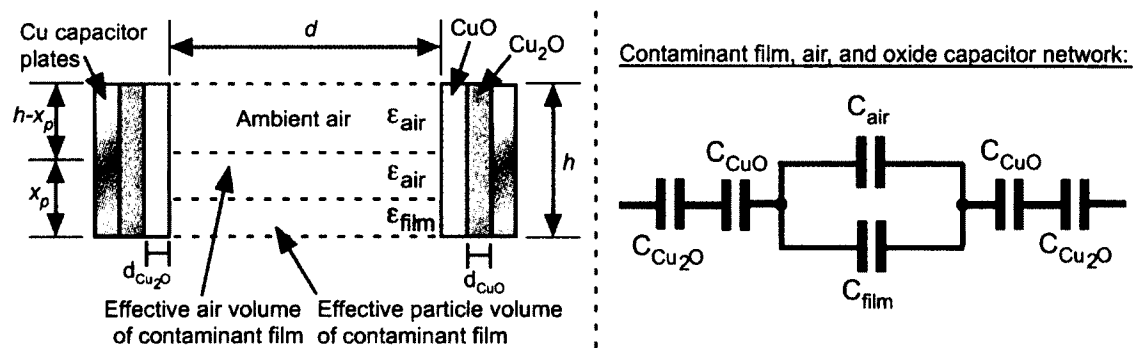


**Figure 6-3:** Cu capacitor plate oxide capacitor representation and schematic.

**Figure 6-3b** illustrates a schematic of the updated capacitor circuit representing all dielectric materials housed in the capacitive analysis chamber and between the capacitor plate electrodes. By combining the parallel capacitance of the rectangular

porous contaminant film ( $C_{film}$ ) with that of the rectangular air space above the contaminant film ( $C_{air}$ ) into a single capacitance ( $C_{chamber}$ ) according to:

$$C_{chamber} = \frac{\epsilon_{eff}\epsilon_0 x_p l}{d} + \frac{\epsilon_{air}\epsilon_0 (h - x_p) l}{d}, \quad \text{Eq. 6-2}$$

the total capacitive output of the of the capacitive sensing element, including the capacitive contribution from the plate electrodes' thin oxide films, can then be expressed with **Eq. 4-3** as a five-component circuit of series-connected capacitor devices by

$$\frac{1}{C} = \frac{1}{C_{Cu_2O}} + \frac{1}{C_{CuO}} + \frac{1}{C_{film}} + \frac{1}{C_{CuO}} + \frac{1}{C_{Cu_2O}} \quad \text{Eq. 6-3}$$

The capacitance contribution due to the capacitor plate electrodes' inner  $Cu_2O$  thin films,  $C_{Cu_2O}$  (F), can be modeled as a single capacitor device (*i.e.* for a single plate electrode) using **Eq. 5-1** according to:

$$C_{Cu_2O} = \frac{\epsilon_{Cu_2O}\epsilon_0 hl}{d_{Cu_2O}}, \quad \text{Eq. 6-4}$$

where  $\epsilon_{Cu_2O}$  is the permittivity of  $Cu_2O$  and  $d_{Cu_2O}$  is the  $Cu_2O$  film's thickness (m).

Similarly, the capacitance contribution of the outer  $CuO$  film can be modeled as a single capacitor device with **Eq. 5-1** according to:

$$C_{CuO} = \frac{\epsilon_{CuO}\epsilon_0 hl}{d_{CuO}}, \quad \text{Eq. 6-5}$$

where  $\epsilon_{CuO}$  and  $d_{CuO}$  are the  $CuO$  film's permittivity and thickness (m), respectively.

Finally, the total capacitive output of the device, including all dielectric materials in the contained in the analysis chamber and between each Cu capacitor plate electrode, is calculated with **Eq. 6-2** by solving for  $C$ , according to:

$$C = \frac{1}{\frac{2}{C_{CuO}} + \frac{2}{C_{C_2O}} + \frac{1}{C_{chamber}}} \quad \text{Eq. 6-6}$$

The physical parameters of each Cu oxide material are summarized in **Table 6-1**, with each material's permittivity obtained from [61].

**Table 6-1:** Cu oxide film parameters.

|                   | Permittivity | Thickness (nm) |
|-------------------|--------------|----------------|
| Cu <sub>2</sub> O | 7.6          | 2.0            |
| CuO               | 18.1         | 1.3            |

## 6.5 Device Fabrication

The integrated sensor's three device layers were fabricated individually, utilizing simple photolithographic and bulk machining processes similar to their respective first generation embodiments, as illustrated in **Figure 6-4**. The first device layer housing the Cr microheater circuit was fabricated on 500 μm quartz wafer. The wafer surface was first processed using the RCA 1 and 2 cleaning procedures prior to the deposition of a 50 nm Cr film by electron beam sputtering. The microheater circuit was then patterned using a single mask photolithography process similar to that described in Section 3.5. Leads were established with each terminal of the heater circuit with a two-part Ag epoxy. The second layer contained the analysis chamber housing the plasma spectroscopic and capacitor sensing elements. A 100 μm microchannel was etched into a 45 × 25 × 3 mm glass sheet using a polymer mask and sandblasting. 100 μm diameter filaments machined from Ti foil were then flush-mounted in the microchannel to function as plasma electrodes. The spacing between filament points was 500 μm to ensure reliable discharges

in air at atmospheric pressure. Electrical terminals were then soldered to each end of the electrode filaments as an interface for the high-voltage power supply.

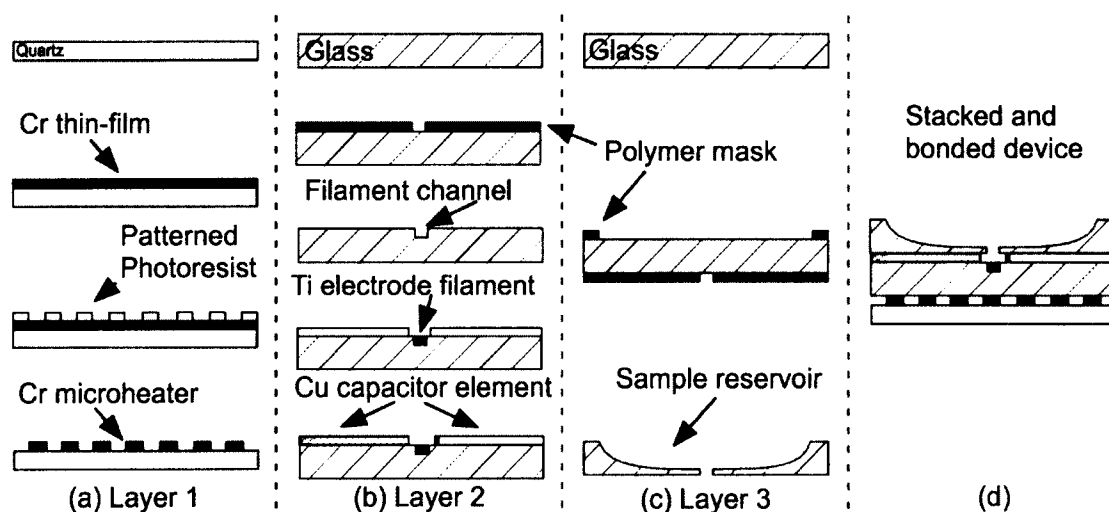


**Figure 6-4:** Fabrication process for the integrated sensor.

Next, a pair of  $20 \times 10 \times 1$  mm and  $45 \times 5 \times 1$  mm Pyrex tiles were machined to form the walls of the spectroscopic/capacitive analysis chamber. Cu foil was then patterned to two adjacent sidewalls of each  $20 \times 10 \times 1$  mm tile to serve as the parallel plate capacitive sensing element and electrical interface with the off-chip capacitance measurement board. The four tiles were then bonded to the substrate to form a  $10 \mu\text{L}$  the rectangular spectroscopic and capacitive analysis chamber. The tiles were oriented such that the analysis chamber was centered along the axis of the Ti electrode filament microchannel and the plasma discharge would occur in the center of the chamber base. The glass tiles containing the Cu capacitive sensing elements were oriented with their interface leads in opposition to minimize fringe capacitance effects, as discussed in Section 6.2.2. Miniature SMB cables were soldered to the ends of the Cu leads to interface with the capacitance measurement board. A layer of epoxy was then applied to the connection and SMB cables to provide a more stable connection between devices.

The third layer housing the 1 mL sample reservoir was fabricated from a  $45 \times 20 \times 3$  mm Pyrex substrate. A polymer mask patterned to the top and bottom faces to define the reservoir and particle aperture boundaries before sandblasting. Finally, the three device layers were stacked and bonded/water sealed with epoxy, as shown in **Figure 6-5**. The total material cost of the integrated device was estimated to be approximately \$45.

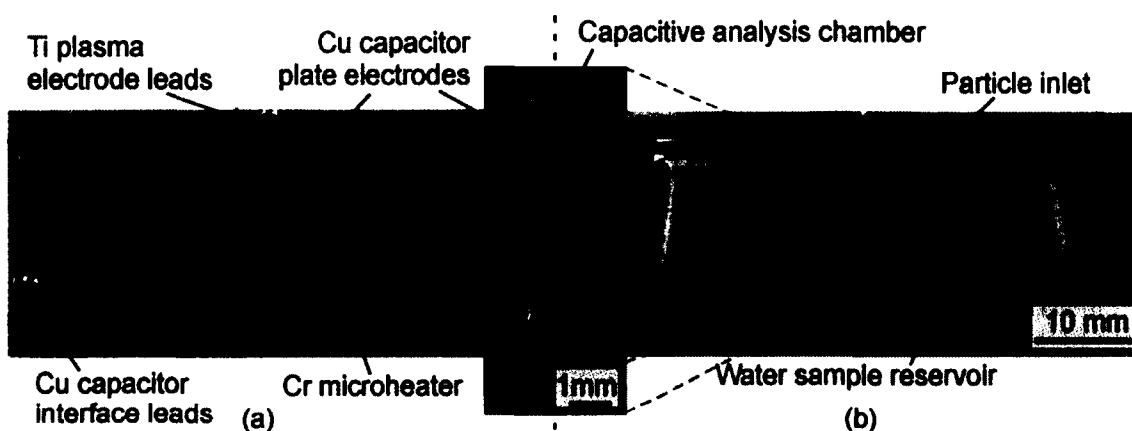


**Figure 6-5:** Finalized integrated sensor prototype.

## 6.6 Experimental Setup

All spectroscopic data were recorded and processed using the same spectrometer and interface software package (Ocean Optics HR2000CG UV-NIS and SpectraSuite) used to test the first-generation plasma spectroscopic device (Section 3.5). Similarly, all capacitive data were recorded using the same capacitance measurement board and interface software package (Analog Devices AD7745/46EBZ) used to test the first-generation capacitive sensing device (Section 5.6). In this work, however, the AD7745 board was powered with two “AA” batteries, rather than the laptop computer it was connected to via a USB 2.0 cable, in an attempt to further reduce noise in the capacitance measurement system that could originate from being powered by a laptop computer.

However, this new power configuration appeared to have no discernable effect on system's capacitive noise. An overview of the all devices and connections used in the integrated diagnostic system's experimental setup is illustrated in **Figure 6-6**.

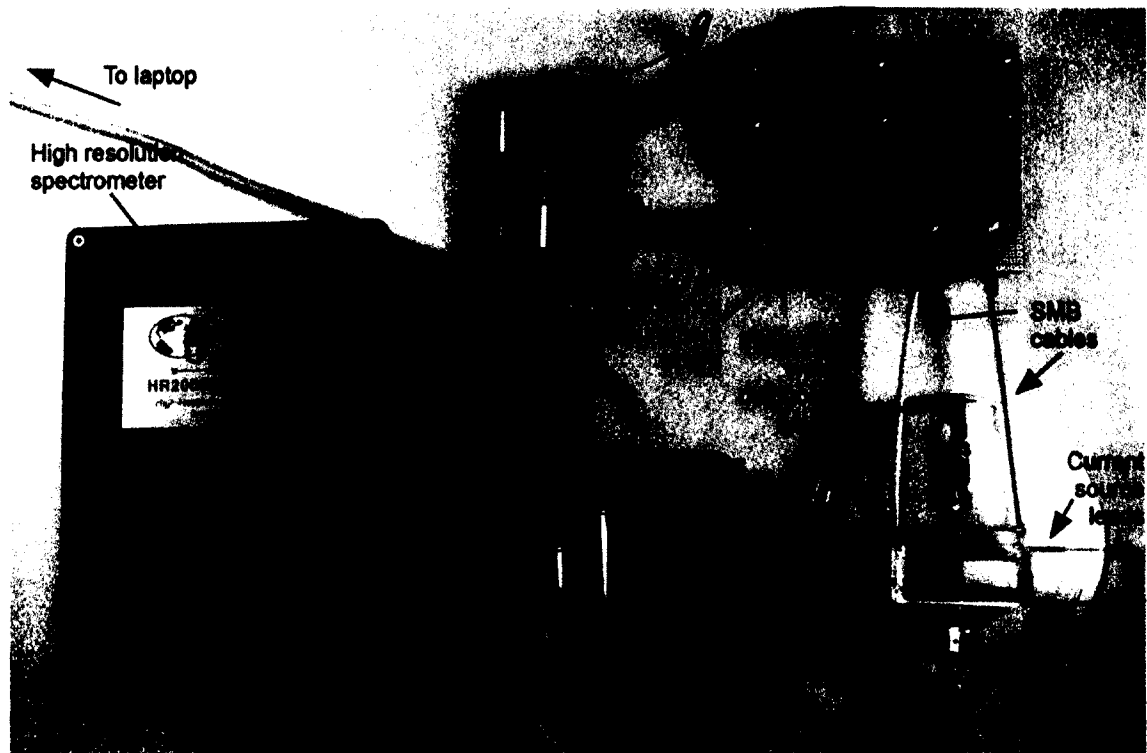


**Figure 6-6:** Experimental setup used to test the integrated sensor prototype.

Two significant hardware upgrades were incorporated into the integrated diagnostic sensor's experimental setup to promote field portability and to reduce capacitive signal noise. First, a custom miniature high voltage power supply was constructed to replace the cumbersome laboratory-scale power supply used previously. This lightweight and low profile power source was assembled from a miniature high voltage step-up transformer (EMCO Q30N-5), a toggle switch, a dual "AA" battery holder, two "AA" batteries, a breadboard, and two miniature "alligator" clips. When supplied with 3V from the two "AA" batteries, the Q30N-5 transformer provided a stable

-3000V DC bias voltage and 0.16 mA of current to the plasma discharge electrodes [64]. This arrangement provided ample voltage and current to create consistent plasma discharges in air at atmospheric pressure.

An improvised Faraday cage was also constructed to enclose the integrated sensor prototype and shield ambient electromagnetic radiation during capacitive analysis. The Faraday cage was constructed from the rectangular bases of unused 250 mL (60 mm × 60 mm) and 500 mL (80 mm × 80 mm) Nalgene chemical storage bottles cut to a height of 18 and 21 mm, respectively. The smaller 250 mL bottle base served as the base of the Faraday cage with the larger 500 mL bottle base functioning as its lid. Rectangular slots were cut into two sides of one corner of the cage's base and lid to serve as feedthroughs for the miniature SMB cables. Two layers of Al foil were then patterned to the contours of each component, covering all exposed surface area. During testing, the integrated sensor prototype was placed diagonally within the Faraday cage's base and covered on top with the lid. Ground connections were established between each cage component, the ground terminals of the miniature SMB cables connecting the sensor prototype to the capacitance measurement board, and the ground terminal of an electrical wall outlet via jumper wires. In this configuration, the average baseline capacitance of the capacitive sensing component of the integrated sensor was reduced by 51.27% to 0.334494 pF, from 0.686471 pF in the first generation capacitive sensing device.

The improvised Faraday cage also minimized the disturbance of fine particles at the contaminant film's surface from ambient air currents. If left uncovered, air currents could be expected to continuously disturb the film's surface particles. In this scenario, the interface between the contaminant particle film and air above would resemble a gradient,



rather than the well-defined boundary between each dielectric material simulated by the model. The Faraday cage ensured the contaminant particles quickly settled at the air/particle interface such that the interface resembled two discrete dielectric materials.

## 6.7 Results

CaCO<sub>3</sub>, MgO, and NaCl contaminants were used to characterize the performance of the integrated sensor prototype and updated numerical concentration-to-capacitance model for water samples with a single contaminant species. Liquid water samples were prepared by mixing high purity (99+%) powders of each contaminant in distilled water at 5, 3.5, 2.5, 1, 0.5, and 0.1 g/L concentrations. Similar to Section 5.7, each contaminant's permittivity was obtained from [61] and their solid densities from their manufacturer's MSDS sheets [65] [66] [60]. Reference bulk densities were measured experimentally.

### 6.7.1 Baseline/Theoretical Capacitance Predictions

The updated single contaminant numerical concentration-to-capacitance model was simulated in MATLAB for each contaminant and concentration level. The material parameters used to simulate each contaminant film's initial theoretical parameters (*i.e.* before applying the bulk density optimization processes discussed in Section 6.4.1) are summarized in rows 2-4 in **Table 6-2**. Model-computed parameters of each composite film are summarized in rows 5-7. As observed in the original single contaminant numerical concentration-to-capacitance model, air-filled interparticle voids were predicted to comprise the majority of the contaminant particle films' volume. These initial porosity estimates were found to be comparable to loosely packed soils in [62]. Initial theoretical capacitance predictions for each contaminant, as a function of contaminant concentration, are shown in **Figure 6-7**. Again, each film's capacitance is

linear (Eq. 6-1 and Eq. 6-6) with its thickness  $x_p$ , which is itself a function of contaminant concentration  $\beta_p$ , according to Eq. 5-3 and Eq. 5-4.

**Table 6-2:** Simulated contaminant parameters based on reference bulk densities.

|  | CaCO <sub>3</sub> | MgO      | NaCl     |
|--|-------------------|----------|----------|
| Density, $\rho$ (g/m <sup>3</sup> )                      | 2.93              | 3.58     | 2.165    |
| Reference Bulk Density, $\eta_{ref}$ (g/m <sup>3</sup> ) | 0.465             | 0.474    | 0.624    |
| Ordinary Permittivity, $\epsilon$                        | 9.15              | 9.65     | 5.9      |
| Effective Permittivity, $\epsilon_{eff}$                 | 1.12824           | 1.00552  | 1.54589  |
| Particle Volume Fraction, $\phi_p$                       | 0.158703          | 0.132402 | 0.288222 |
| Air Volume Fraction, $\phi_{air}$                        | 0.841297          | 0.867598 | 0.711778 |

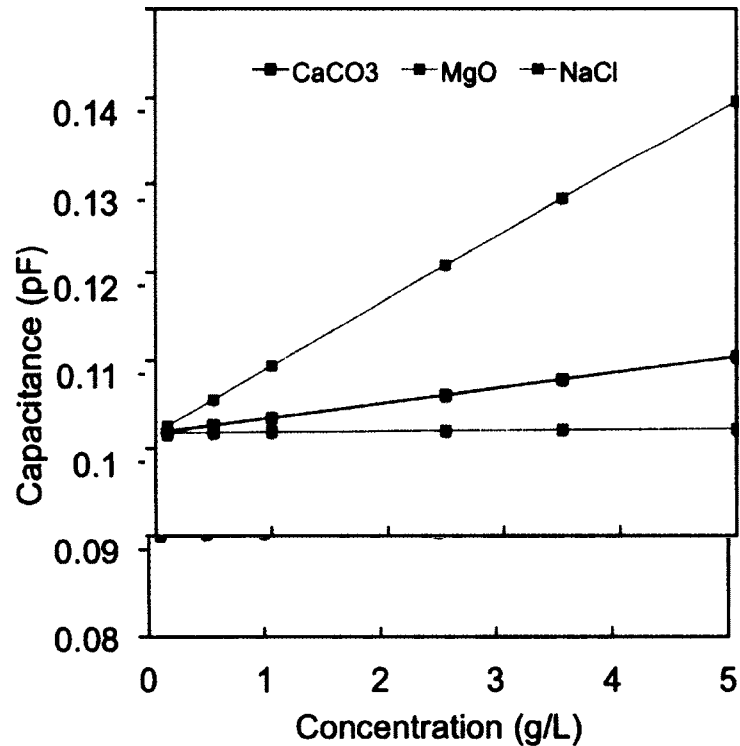


**Figure 6-7:** Theoretical contaminant capacitances based on reference bulk densities.

Specific theoretical capacitances for each contaminant and concentration are detailed in their respective sections below. The numerical model's initial theoretical capacitances, based on the material's reference bulk density, are shown first with an error analysis of these results against experimentally measured capacitance data. The

contaminant material's bulk density is then optimized, as described in Section 6.4.1, for maximal agreement between theoretical and experimental data with updated error analysis results. A MATLAB template representing the updated single contaminant model used to simulate this data is provided in Appendix D.

### 6.7.2 CaCO<sub>3</sub> Spectral Data

A representative spectrum of the atomic and molecular fragments of CaCO<sub>3</sub> contaminant particle films at a concentration of 3.5 g/L is illustrated in **Figure 6-8**.

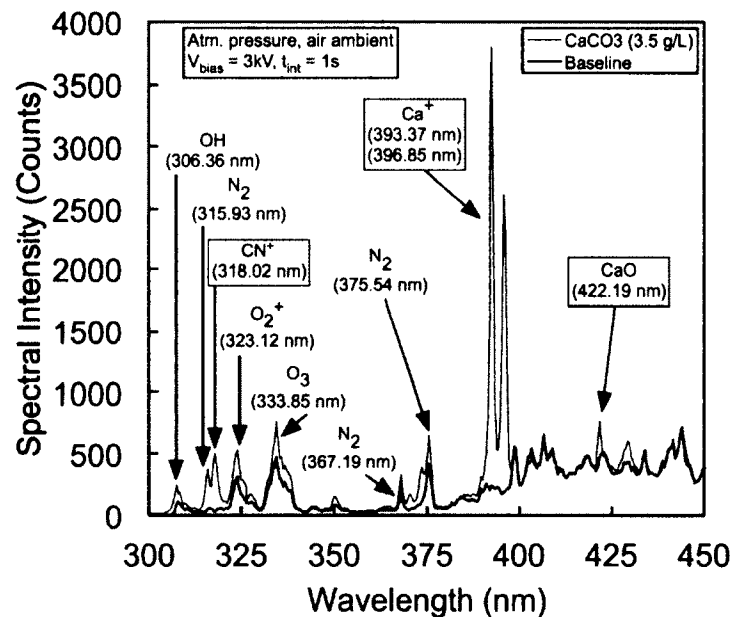


**Figure 6-8:** CaCO<sub>3</sub> atomic and molecular fragment spectra at 3.5 g/L.

Similar to the Section 3.6.3 results, the atomic components of CaCO<sub>3</sub> were only partially represented in the film's spectra. CaCO<sub>3</sub> contaminants could be identified by observing spectral lines from three atomic and molecular groups, including CN<sup>+</sup>, Ca<sup>+</sup>, and an ambiguous spectral line at 422.19 nm due to either a Ca ion or a CaO molecule. The 422.19 nm line was again observed with a spectral intensity comparable to the previous

CaCO<sub>3</sub> data set in Section 3.6.3. The CN<sup>+</sup> line observed at 318.02 nm is very likely the result of C from decomposed CaCO<sub>3</sub> recombining with atmospheric N. Again, two Ca<sup>+</sup> lines were observed at 393.37 and 396.85 nm at substantially greater intensity. The average line intensities for each group in **Figure 6-8** were observed to generally decrease with decreasing contaminant concentration, as shown in **Figure 6-9**.

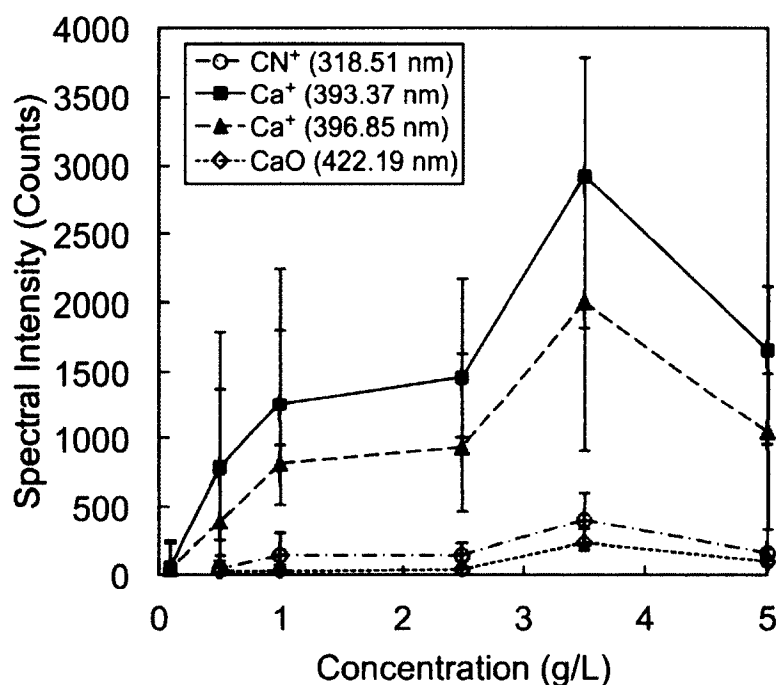


**Figure 6-9:** CaCO<sub>3</sub> fragment spectral line intensity versus concentration.

The most striking feature of this data is the 5 g/L data point, where the average, minimum, and maximum photon counts for all fragment lines breaks the decreasing trend with concentration. Because all spectral lines in the 5 g/L data set were affected, this is a possible result of a mismatch between the optical fiber and device orientation during the 5 g/L test, lowering the overall photon count. Overall, Ca<sup>+</sup> lines were observed to have significantly more counts and exhibited a greater min/max count range. Further, the ionic

Ca lines were observed to emit discernable spectra at all contaminant concentration levels while the (putative) Ca and C-based molecular fragments were only observed to 0.5 g/L.

### 6.7.3 CaCO<sub>3</sub> Capacitance Data

Experimental and (un-optimized) theoretical CaCO<sub>3</sub> film capacitances, as a function of contaminant concentration, are illustrated in **Figure 6-10**. The 0.1 g/L capacitance was measured but excluded from this data set because its value was negative (-0.009074 pF), representing an average film capacitance that was less than the average baseline capacitance. This concentration level could represent the device's noise floor where a film's capacitance becomes indistinguishable from system noise. Exclusion of this erroneous capacitance value improved the data's R<sup>2</sup> value from 0.898144 to 0.91009, allowing greater theoretical/experimental agreement after optimizing the bulk density.

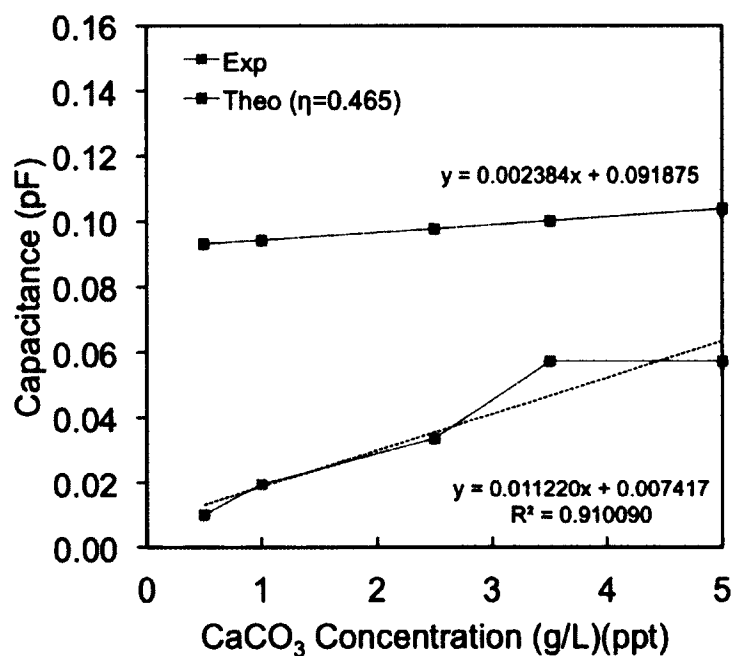


**Figure 6-10:** Theo/Exp results for CaCO<sub>3</sub> films, for reference  $\eta$ .

The y-intercept for a capacitance-versus-concentration line represents the zero concentration capacitance (*i.e.* the capacitance between the sensor's plates when no contaminants are present and only air fills the chamber volume). The y-intercept resulting from the experimental trendline suggests the device's zero contaminant concentration capacitance to be 0.007417 pF. The numerical model, however, predicted a much greater zero concentration capacitance of 0.091875 pF, representing a 1238.71% increase over that resulting from the experimental data. **Table 6-3** summarizes the error analysis results for the initial theoretical/experimental CaCO<sub>3</sub> film capacitances.

**Table 6-3:** Theo/Exp data summary for CaCO<sub>3</sub> films, for reference  $\eta$ .

| Contaminant Concentration, $\beta_p$ (g/L) | Theoretical Capacitance ( $\eta=0.465 \text{ g/cm}^3$ ) (pF) | Experimental Capacitance (pF) | Error    |
|--|--|-------------------------------|----------|
| 5.0  | 0.103793   | 0.057225                      | 44.8661% |
| 3.5  | 0.100218   | 0.057384                      | 42.7403% |
| 2.5  | 0.097834   | 0.033408                      | 65.8522% |
| 1.0  | 0.094259   | 0.019319                      | 79.5042% |
| 0.5  | 0.093067   | 0.009998                      | 89.2571% |

The initial theoretical and experimental capacitance agreement was generally poor and tended to degrade as the concentration decreased. Before optimizing the CaCO<sub>3</sub> bulk density, the model tended to overestimate the film's capacitance by between 42.7403% at 3.5 g/L and 89.2571% at 0.5 g/L. The optimized capacitance versus concentration line is shown in **Figure 6-11**. Optimal slope agreement occurred when the CaCO<sub>3</sub> bulk density was increased 84.34% to 0.8572 g/cm<sup>3</sup>. Here, the optimized theoretical and experimental trendlines were offset by a constant capacitance of 0.084458 pF, which was substituted into **Eq. 6-1** for maximal theoretical/experimental agreement, as shown in **Figure 6-12**.

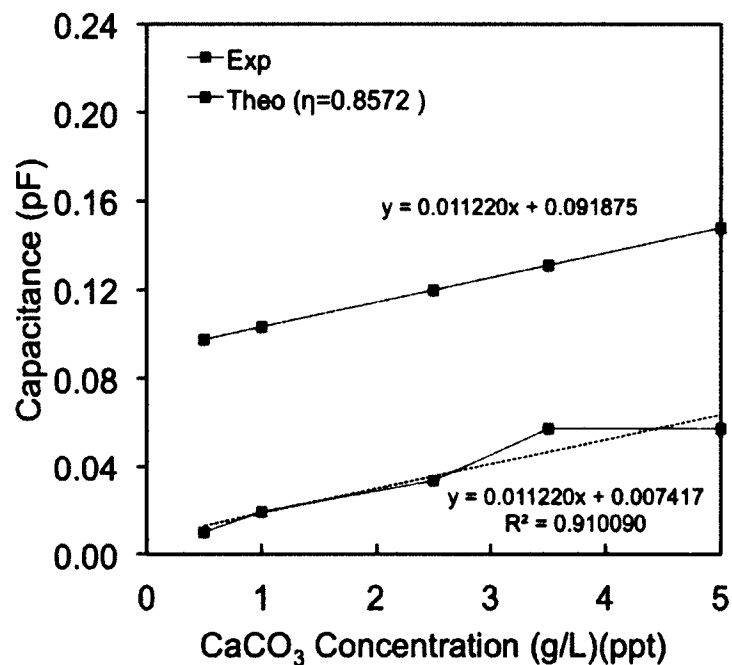


**Figure 6-11:** Theo/Exp results for CaCO<sub>3</sub> films, with optimized  $\eta$ .

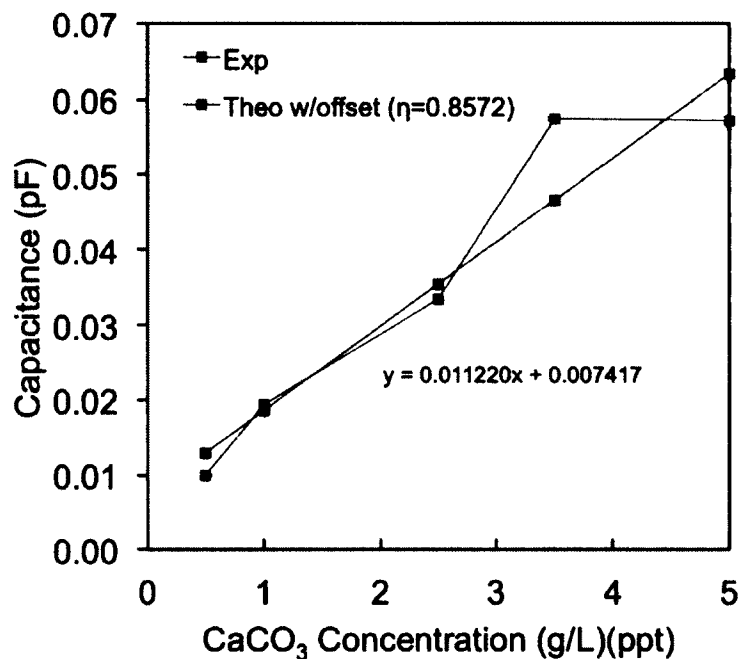


**Figure 6-12:** Theo/Exp results for CaCO<sub>3</sub> films, for optimized  $\eta$ , with offset.

An updated error analysis for the theoretical and experimental capacitance data is summarized in **Table 6-4**. Overall,  $\text{CaCO}_3$  bulk density optimization significantly improved the theoretical versus experimental error. The updated error results at 5, 2.5, and 1 g/L levels were comparable to those in Chapter 5 for single contaminant films with the original capacitive sensor. The greater theoretical/experimental error at the 3.5 and 0.5 g/L concentrations was the result of poor experimental linearity at these points.

**Table 6-4:** Theo/Exp data summary for  $\text{CaCO}_3$  films, with optimized  $\eta$  and offset.

| Contaminant Concentration, $\beta_p$ (g/L) | Theoretical Capacitance ( $\eta=0.8572 \text{ g/cm}^3$ + Offset (pF)) | Experimental Capacitance (pF) | Error     |
|--|---|-------------------------------|-----------|
| 5  | 0.063518  | 0.057225                      | 9.90721%  |
| 3.5  | 0.046688  | 0.057384                      | -22.9106% |
| 2.5  | 0.035468  | 0.033408                      | 5.80757%  |
| 1  | 0.018637  | 0.019319                      | -3.65966% |
| 0.5  | 0.013027  | 0.009998                      | 23.2528%  |

Updated physical parameters of the  $\text{CaCO}_3$  films with the optimized bulk density (highlighted in blue) are summarized in **Table 6-5**. The porous  $\text{CaCO}_3$  film's effective permittivity  $\epsilon_{eff}$  was observed to increase 86.9% (from 1.12824), while the film's porosity  $\phi_{air}$  decreased by 15.91% (from 0.841297).

**Table 6-5:**  $\text{CaCO}_3$  film parameters based on optimized  $\eta$ .

|  | $\text{CaCO}_3$ |
|--|-----------------|
| Density, $\rho$ ( $\text{g/m}^3$ )                       | 2.93            |
| Reference Bulk Density, $\eta_{ref}$ ( $\text{g/cm}^3$ ) | 0.465           |
| Optimized Bulk Density, $\eta_{opt}$ ( $\text{g/cm}^3$ ) |                 |
| Ordinary Permittivity, $\epsilon$                        | 9.15            |
| Effective Permittivity, $\epsilon_{eff}$                 |                 |
| Particle Volume Fraction, $\phi_p$                       |                 |
| Air Volume Fraction, $\phi_{air}$                        |                 |



### 6.7.4 MgO Spectral Data

A representative spectrum of the atomic and (putative) molecular fragments of MgO contaminant films, at the 5 g/L concentration level, is illustrated in **Figure 6-13**. Here, the two atomic components of the MgO contaminant can only be partially accounted for, due to the ambiguity regarding the origin of the line at 383.48 nm. It is possible that this line results from an MgOH molecule, thereby potentially representing the O component of the original MgO contaminant. Other possibilities for the origin of the 383.48 nm spectral line are likely similar to those described at length in Section 3.6.6. Similar to the previous CaCO<sub>3</sub> spectral data set, a robust and unambiguous Mg ion line was observed at 280.27 nm. Additionally, the overall photon counts for this Mg ion line and the putative 383.48 nm MgOH line were comparable to those for MgO contaminants observed in Chapter 3 (see **Figure 3-15**).

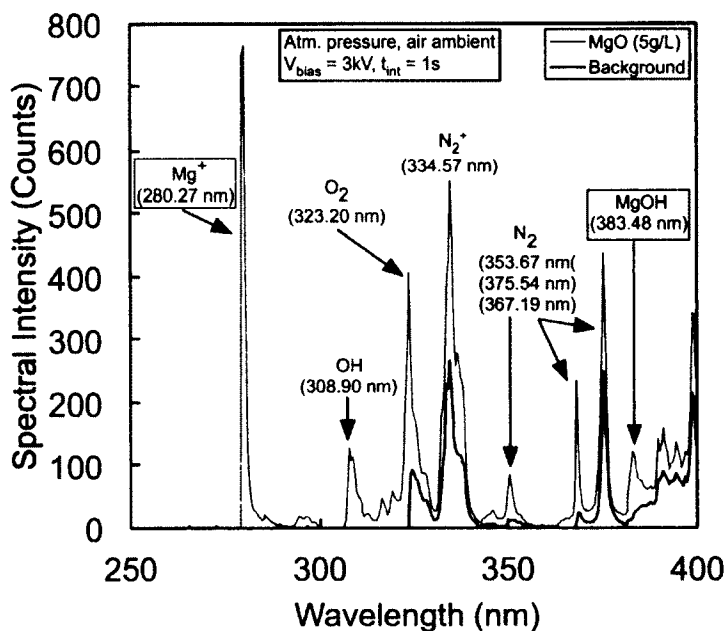


**Figure 6-13:** MgO atomic and molecular fragment spectra at 5 g/L.

As with the  $\text{CaCO}_3$  fragment spectra in the previous section, the average ionic Mg and putative MgOH line intensities from the MgO contaminants tended to decrease with decreasing MgO contaminant concentration, as illustrated in **Figure 6-14**. Again, the ionic Mg atomic fragment emitted significantly more photons than the supposed 383.48 nm MgOH fragment and exhibited a greater degree of variation in its minimum and maximum photon counts. Both lines were observable between 5 and 0.5 g/L but were not detected at 0.1 g/L, which may represent the integrated device's spectral noise floor for this contaminant species.

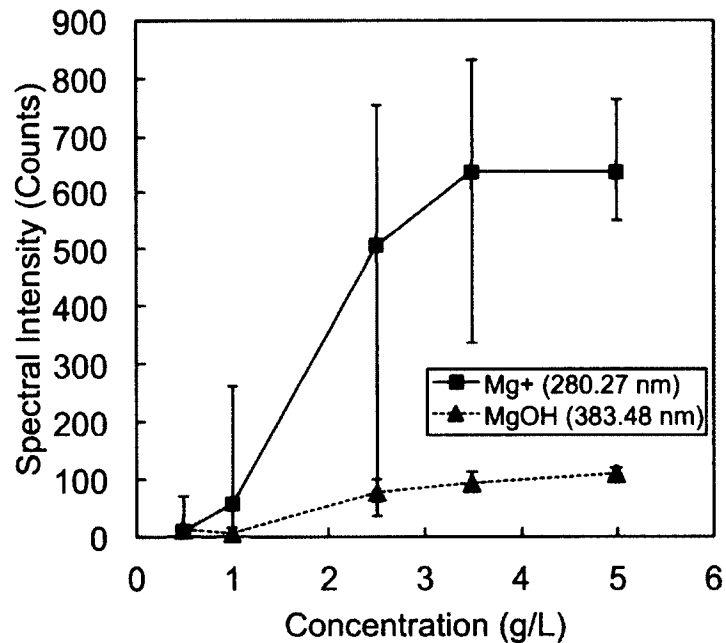


**Figure 6-14:** MgO fragment spectral line intensity versus concentration.

#### 6.7.5 MgO Capacitance Data

The initial theoretical MgO film capacitances based on the material's reference bulk density and experimentally measured MgO film capacitances, as a function of contaminant concentration, are illustrated graphically in **Figure 6-15**.

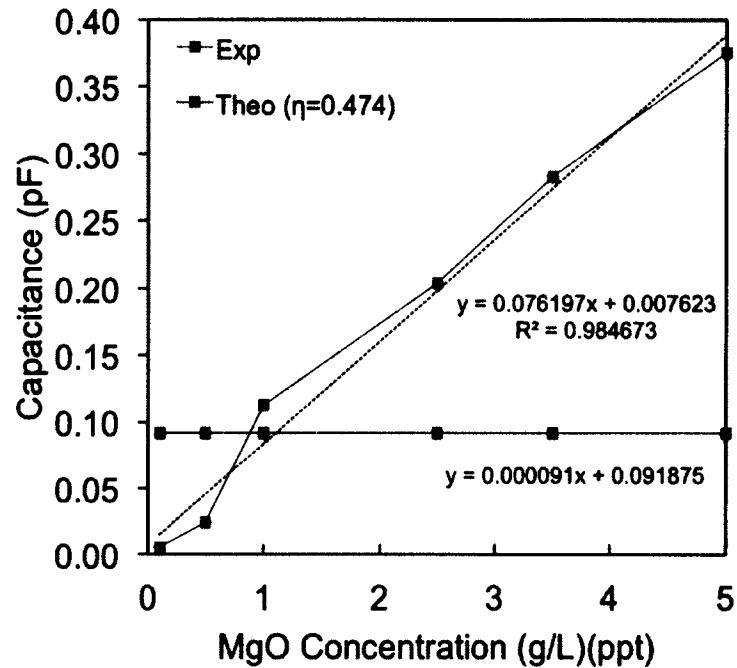


**Figure 6-15:** Theo/Exp results for MgO films, for reference  $\eta$ .

Clearly, the agreement between the optimized initial theoretical and experimental capacitances is very poor, due to the extreme mismatch between the slopes of the theoretical and experimental trendlines. As illustrated in **Figure 6-15**, the theoretical trendline slope was observed to be three orders of magnitude lower than that of the experimental trendline, causing the theoretical capacitance line to be nearly horizontal (*i.e.* a trendline slope of approximately zero). The  $R^2$  value for the MgO experimental capacitance trendline, however, was significantly higher than that observed in the  $\text{CaCO}_3$  data set. As expected, the model's zero concentration capacitance remained the same (0.091875 pF), while that of the MgO experimental data increased by only 2.78% to 0.007623 pF from 0.07417 pF in the  $\text{CaCO}_3$  experimental data set. Error analysis results for the numerical model's initial theoretical MgO film capacitances (based on the un-optimized bulk density parameter) and experimentally measured capacitances values for

the MgO contaminant films are shown in **Table 6-6**. Before applying the bulk density optimization process to the MgO theoretical capacitance data, the numerical concentration-to-capacitance model's results tended to significantly underestimate the MgO films' capacitances by between -22.505% at the 1 g/L concentration and -307.139% at the 5 g/L concentration level. The numerical model results were also observed to overestimate the MgO film capacitance by between 73.33251% and 94.0557% at the 0.5 and 0.1 g/L concentration levels, respectively.

**Table 6-6:** Theo/Exp data summary for MgO films, for reference  $\eta$ .

| Contaminant Concentration, $\beta_p$ (g/L) | Theoretical Capacitance ( $\eta=0.465 \text{ g/cm}^3$ ) (pF) | Experimental Capacitance (pF) | Error     |
|--|--|-------------------------------|-----------|
| 5  | 0.092332   | 0.375917                      | -307.139% |
| 3.5  | 0.092195   | 0.283429                      | -207.425% |
| 2.5  | 0.092103   | 0.203838                      | -121.315% |
| 1  | 0.091966   | 0.112661                      | -22.5025% |
| 0.5  | 0.091921   | 0.024520                      | 73.3251%  |
| 0.1  | 0.091884   | 0.005462                      | 94.0557%  |

Optimal agreement between the slopes of the theoretical and experimental capacitance trendlines occurred when the MgO bulk density parameter was increased by 724.49% to  $3.43412 \text{ g/cm}^3$ , as illustrated graphically in **Figure 6-16**. The bulk density-optimized theoretical and experimental capacitance trendlines were again offset by their respective zero contaminant concentration capacitances of 0.091875 and 0.007623 pF, respectively, representing a total fringe capacitance offset of 0.084252 pF. The numerical model was then updated to reflect this new fringe capacitance offset correction factor (see **Eq. 6-1**) and a greater degree of theoretical versus experimental agreement was observed with the optimized data, as shown in **Figure 6-17**.

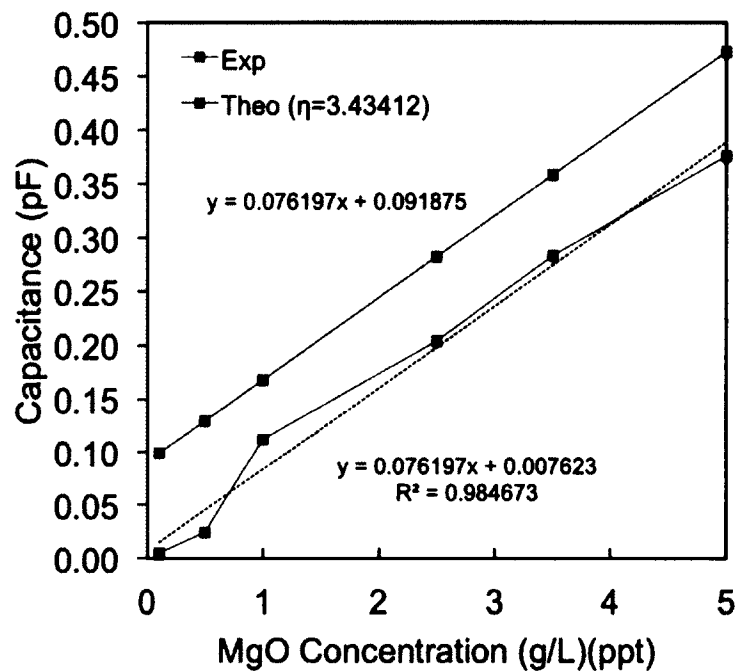


Figure 6-16: Theo/Exp results for MgO films, with optimized  $\eta$ .

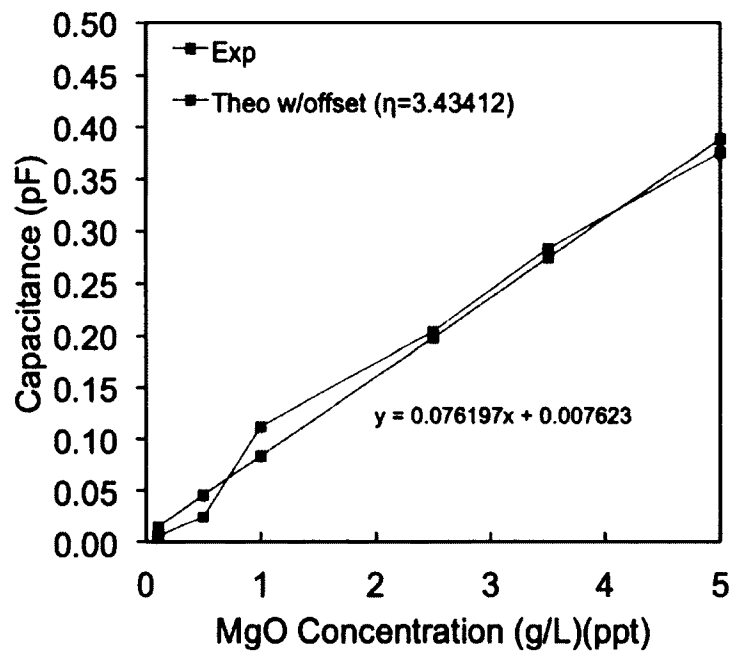


Figure 6-17: Theo/Exp results for MgO films, for optimized  $\eta$ , with offset.

An updated error analysis between the bulk density-optimized theoretical and experimental capacitance values for MgO films is summarized in **Table 6-7**.

Optimization of the MgO bulk density parameter significantly improved the theoretical versus experimental error at all concentration levels. However, the 5 to 2.5 g/L concentration range saw the greatest improvement in error, with the updated model's results in this range being comparable to error results reported in Chapter 5 for single contaminant tests. Below 2.5 g/L, the error increased with decreasing contaminant concentration due to the experimental capacitances at the lower bound of the concentration range diverging significantly from data set's trendline.

**Table 6-7:** Theo/Exp data summary for MgO films, with optimized  $\eta$  and offset.

| Contaminant Concentration, $\beta_p$ (g/L) | Theoretical Capacitance ( $\eta=3.43412 \text{ g/cm}^3$ ) + Offset (pF) | Experimental Capacitance (pF) | Error     |
|--|---|-------------------------------|-----------|
| 5  | 0.388609  | 0.375917                      | 3.26589%  |
| 3.5  | 0.274314  | 0.283429                      | -3.32283% |
| 2.5  | 0.198116  | 0.203838                      | -2.88837% |
| 1  | 0.083821  | 0.112661                      | -34.4068% |
| 0.5  | 0.045722  | 0.02452                       | 46.3720%  |
| 0.1  | 0.015243  | 0.005462                      | 64.1676%  |

Updated physical parameters (highlighted in blue) of the MgO films based on the optimized bulk density parameter are summarized in **Table 6-8**. Here, the MgO composite film's effective permittivity  $\epsilon_{eff}$  increased by 3097.76% to 31.14886 from 1.00552, while the film's porosity  $\phi_{air}$  was decreased significantly (95.3%) to 0.0407486 from 0.867598. The dramatic change in the model's MgO/air composite film permittivity and porosity can be seen as the result of the material's bulk density nearly approaching its

solid density in model estimates. The optimized porosity estimate was observed to be just below the minimum porosity of 11% for densely packed soils in [62].

**Table 6-8:** MgO film parameters based on optimized  $\eta$ .

|   | MgO   |
|---|-------|
| Density, $\rho$ (g/m <sup>3</sup> )                       | 3.58  |
| Reference Bulk Density, $\eta_{ref}$ (g/cm <sup>3</sup> ) | 0.465 |
| Optimized Bulk Density, $\eta_{opt}$ (g/cm <sup>3</sup> ) |       |
| Ordinary Permittivity, $\epsilon$                         | 9.65  |
| Effective Permittivity, $\epsilon_{eff}$                  |       |
| Particle Volume Fraction, $\phi_p$                        |       |
| Air Volume Fraction, $\phi_{air}$                         |       |

#### 6.7.6 NaCl Spectral Data

A representative spectrum of NaCl contaminant films at 5 g/L is illustrated in **Figure 6-18**. NaCl contaminants could be partially identified by observing an atomic Na line at 589.00 nm and two much weaker (and therefore ambiguous) spectral lines detected at 396.15 and 465.51 nm, which could potentially be due to  $\text{Cl}_2^+$  molecules. The 465.51 nm line was not previously observed in Section 3.6.7. In contrast with **Figure 3-16**, the intensity of the 589.00 nm Na line in **Figure 6-18** is surprisingly low, considering this line's intensity is documented to be several orders of magnitude in [40]. The general trend of the Na and putative  $\text{Cl}_2^+$  line intensities was also observed to decrease as a function on decreasing contaminant concentration, as shown in **Figure 6-19**. As with  $\text{Ca}^+$  in  $\text{CaCO}_3$  and  $\text{Mg}^+$  in MgO contaminants, the Na ion emitted significantly more photons and exhibited a greater degree of variation in its minimum and maximum photon counts than the putative  $\text{Cl}_2^+$  line. Detection of NaCl fragments also fell off much more quickly with decreasing concentration over the other two contaminants, with ionic Na observable down to 1 g/L while  $\text{Cl}_2^+$  was only observed at 5 and 3.5 g/L.

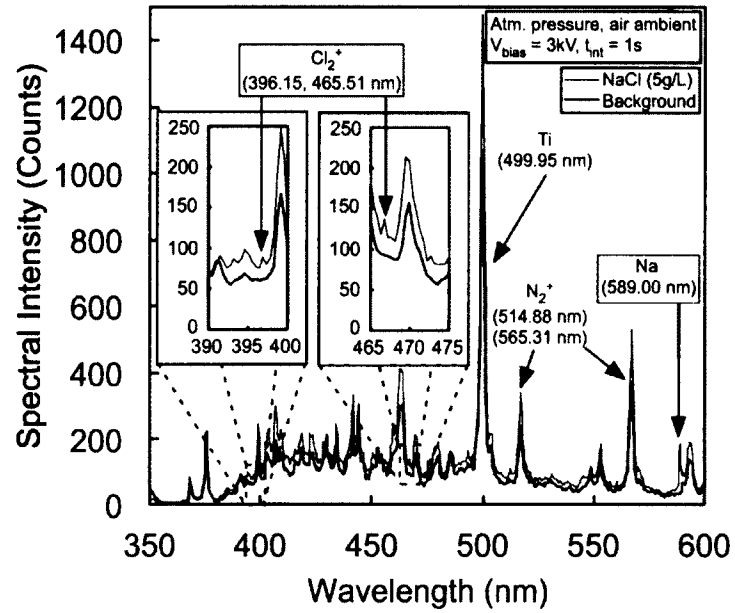


**Figure 6-18:** NaCl atomic and molecular fragment spectra at 5 g/L.

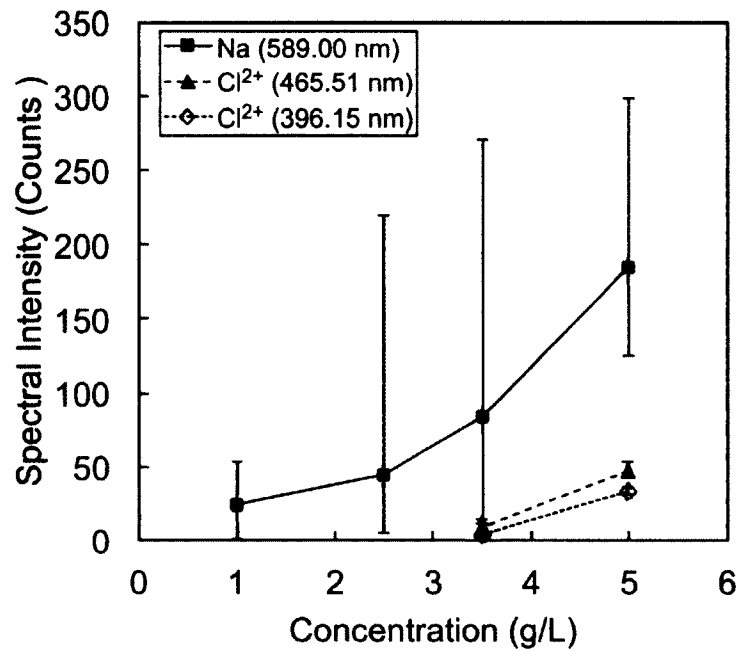


**Figure 6-19:** NaCl fragment spectral line intensity versus concentration.



### 6.7.7 NaCl Capacitance Data

The initial theoretical NaCl film capacitances, based on the reference bulk density, and experimentally measured NaCl film capacitances, as a function of concentration, are illustrated in **Figure 6-20**. The original “best fit” trendline for the NaCl experimental data resulted in a y-intercept, or zero concentration capacitance, of -0.008496 pF. This negative zero concentration capacitance was concluded to be erroneous and a likely result of capacitance measurement errors at lower contaminant concentrations, particularly 2.5 g/L and less. To reflect a more realistic scenario, the y-intercept for the experimental trendline was manually set to 0.007 pF, which was similar to that in the CaCO<sub>3</sub> and MgO data set—to three decimal places—and resulted in an R<sup>2</sup> value comparable to the other experimental data sets in this work (R<sup>2</sup>=0.939181).

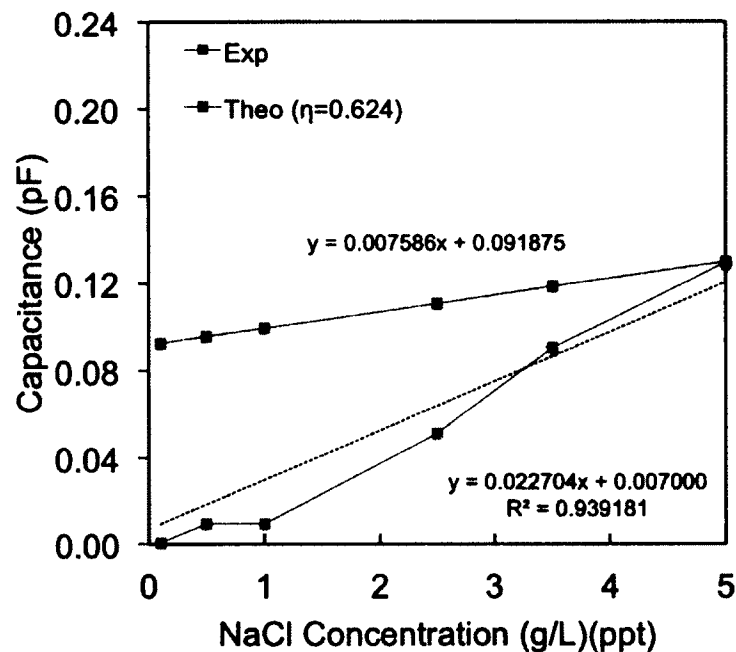


**Figure 6-20:** Theo/Exp results for NaCl films, for reference  $\eta$ .

**Table 6-9** summarizes the error analysis results for the updated numerical model's initial theoretical (*i.e.* utilizing the un-optimized reference bulk density parameter) results and experimentally measured capacitance values for the NaCl films. Overall, the error between initial theoretical and experimental capacitances was poor and increased with decreasing contaminant concentration, due to the mismatched slopes of the theoretical and experimental trendlines and the fringe capacitance offset.

**Table 6-9:** Theo/Exp data summary for NaCl films, for reference  $\eta$ .

| Contaminant Concentration, $\beta_p$ (g/L) | Theoretical Capacitance ( $\eta=0.624$ g/cm <sup>3</sup> ) (pF) | Experimental Capacitance (pF) | Error     |
|--|---|-------------------------------|-----------|
| 5  | 0.129803  | 0.129233                      | 0.438827% |
| 3.5  | 0.118425  | 0.090526                      | 23.5585%  |
| 2.5  | 0.110839  | 0.050993                      | 53.9933%  |
| 1  | 0.099461  | 0.009176                      | 90.7739%  |
| 0.5  | 0.095668  | 0.009356                      | 90.2202%  |
| 0.1  | 0.092634  | 0.000769                      | 99.1695%  |

Optimal agreement between the NaCl theoretical and experimental trendline slopes occurred when the film's bulk density was increased by 212.04%, from 0.624 g/cm<sup>3</sup> to 1.32315 g/cm<sup>3</sup>, as illustrated in **Figure 6-21**. As before, the numerical capacitance-to-concentration model's bulk density-optimized theoretical line and experimental trendline were offset by a constant capacitance value (0.084875 pF for this data set), representing the difference between the theoretical and experimental trendline zero concentration capacitances of 0.091875 and 0.007000 pF, respectively. The numerical model was then updated to reflect this new fringe capacitance offset correction factor (see **Eq. 6-1**) and a greater degree of agreement between the theoretical and experimental data was realized, as illustrated in **Figure 6-22**.

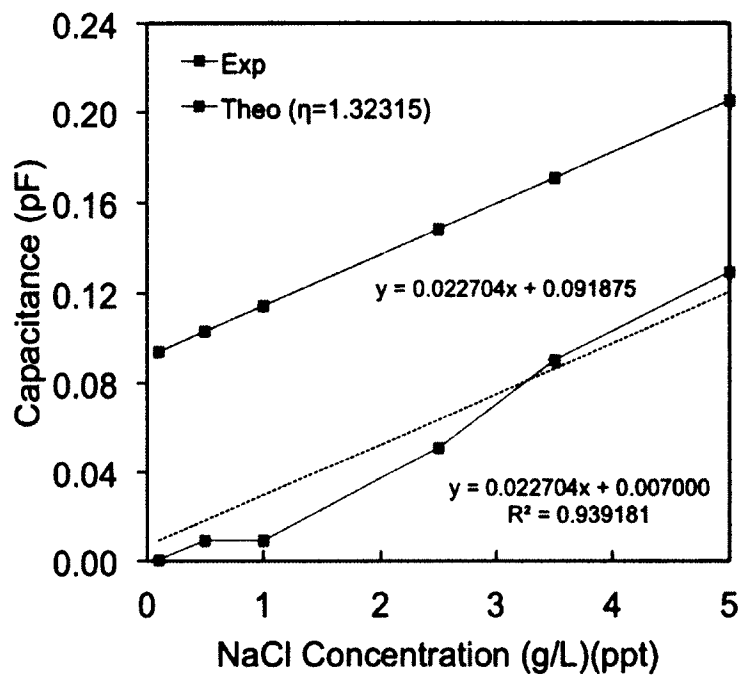


Figure 6-21: Theo/Exp results for NaCl films, with optimized  $\eta$ .

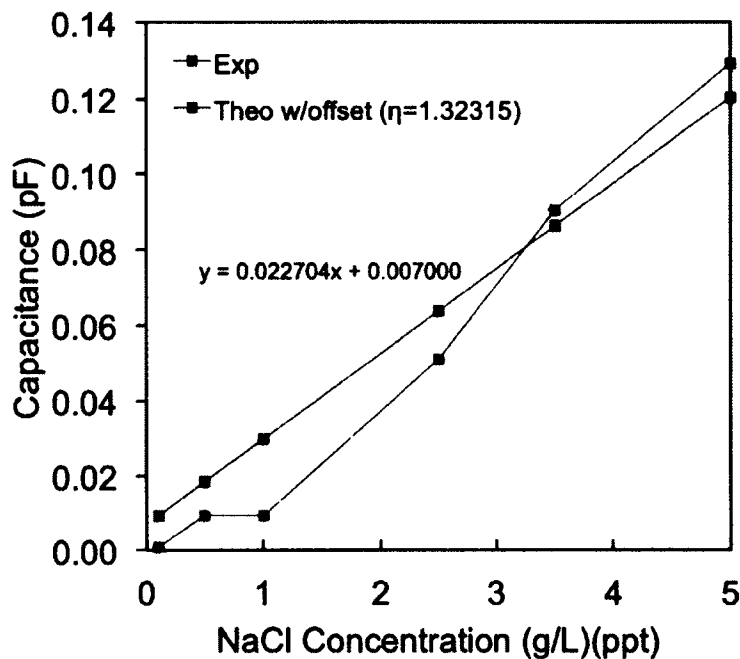


Figure 6-22: Theo/Exp results for NaCl films, for reference  $\eta$ , with offset.

An updated error analysis between the numerical model's bulk density-optimized theoretical results and experimental capacitance values is summarized in **Table 6-10**. Overall, the error between the updated numerical model's theoretical results and experimentally measured film capacitances was improved by optimizing the NaCl film's bulk density parameter and considering the offset capacitance between the data sets. However, this improvement in error was marginal at NaCl contaminant concentrations of 2.5 g/L and less, where the greatest divergence between experimental capacitance data and the experimental capacitance trendline were observed to occur. While the experimental data already showed a less than satisfactory linearity, artificially setting the experimental data trendline's y-intercept to 0.007 pF further reduced the data set's linearity and had a detrimental effect on the theoretical versus experimental error, particularly below the 2.5 g/L concentration level. However, the theoretical versus experimental error at concentrations between 5 and 2.5 g/L were observed to be comparable to the error results reported in Chapter 5 for single contaminant data.

**Table 6-10:** Theo/Exp data summary for NaCl films, with optimized  $\eta$  and offset.

| Contaminant Concentration, $\beta_p$ (g/L) | Theoretical Capacitance ( $\eta=1.39956 \text{ g/cm}^3$ ) + Offset (pF) | Experimental Capacitance (pF) | Error     |
|--|---|-------------------------------|-----------|
| 5  | 0.120518  | 0.129233                      | -7.23161% |
| 3.5  | 0.086463  | 0.090526                      | -4.69897% |
| 2.5  | 0.063759  | 0.050993                      | 20.0217%  |
| 1  | 0.029704  | 0.009176                      | 69.1072%  |
| 0.5  | 0.018352  | 0.009356                      | 49.0182%  |
| 0.1  | 0.009270  | 0.000769                      | 91.7018%  |

Updated physical parameters (highlighted in blue) of the NaCl films based on the optimized bulk density parameter are summarized in **Table 6-11**. Optimization of the

NaCl film's bulk density parameter resulted in a 288.61% increase in the film's composite permittivity from 1.5459 to 4.4616 and a 54.63% decrease in the films' simulated porosity, decreasing from 0.711778 to 0.388845.

**Table 6-11:** NaCl film parameters based on optimized  $\eta$ .

|   | NaCl  |
|---|-------|
| Density, $\rho$ (g/m <sup>3</sup> )                       | 2.165 |
| Reference Bulk Density, $\eta_{ref}$ (g/cm <sup>3</sup> ) | 0.624 |
| Optimized Bulk Density, $\eta_{opt}$ (g/cm <sup>3</sup> ) |       |
| Ordinary Permittivity, $\epsilon$                         | 5.9   |
| Effective Permittivity, $\epsilon_{eff}$                  |       |
| Particle Volume Fraction, $\phi_p$                        |       |
| Air Volume Fraction, $\phi_{air}$                         |       |

## 6.8 Discussion

Overall, the integrated device provided a satisfactory spectroscopic analysis of a contaminant's chemical composition, with almost all of a contaminant's atomic components being accounted for down to 1 g/L concentrations or less. The results of the capacitive sensing and updated numerical model components' characterization of an impurity's concentration, however, were mixed. For contaminant concentrations in the range of 5 to 2.5 g/L, the model's agreement with experimental results were satisfactory but below 2.5 g/L, its error was significant.

Two defects limited the integrated device's performance. First, the 50 nm microheaters were inoperable, evidently due to excessive oxidation of the Cr surface resulting in a microheater resistance exceeding 10,000 Ohms. Water samples were then preconcentrated by placing the device on a hotplate. The hydrophobic film also proved to be ineffective at promoting the aggregation of contaminant particles in the analysis chamber. Instead, particles were manually placed in the analysis chamber after hotplate

preconcentration with as little compaction as possible. Manual placement of contaminant particles likely contributed to the poorer linearity observed here, compared to the work reported in Chapter 5 with the first generation capacitive sensor.

When considering the tradeoffs between sample/device size and concentration detection levels, this investigation demonstrated that even larger sample volumes than 1 mL would be advantageous for achieving greater accuracy between theoretical predictions and experimental data, particularly at the 0.1 g/L concentration where EPA regulations are often set. The larger sample volume would provide a greater quantity of contaminant particles, which would then yield greater capacitances above the measurement boards minimum resolvable capacitance, which was often approached in this investigation for 1 g/L concentrations and lower. This increased sample size would also be expected to improve the spectroscopic components detection sensitivity.

## 6.9 Conclusion

An integrated plasma spectroscopic and capacitive sensing device was developed to identify a water contaminant's chemical composition and characterize its concentration in conjunction with an updated numerical capacitance-to-concentration model.  $\text{CaCO}_3$ ,  $\text{MgO}$ , and  $\text{NaCl}$  water contaminants were investigated at 5, 3.5, 2.5, 1, 0.5, and 0.1 g/L concentrations. The device's plasma spectroscopic component provided a satisfactory accounting of each material though atomic and molecular spectral lines observed down to 0.5 g/L or less for  $\text{CaCO}_3$  and  $\text{MgO}$  contaminants and to 3.5 g/L for  $\text{NaCl}$ . The capacitive sensor and numerical model's characterization of the contaminant's capacitance was much more limited, the 5 to 2.5 g/L range providing the best agreement between theoretical and experimental data.

## **APPENDIX A**

### **COMPREHENSIVE SPECTRAL LINE DATA**

**Table A-1** summarizes all spectral data referenced in this work. Atomic spectral lines were obtained from the *CRC Handbook of Chemistry and Physics* (77<sup>th</sup> Edition) [40] and molecular line data from *Identification of Molecular Spectra* (3<sup>rd</sup> Edition) [41]. The lower case k in the spectral intensity column represents a 1000 multiplier.

**Table A-1:** Comprehensive atomic and molecular spectral line data.

| Atom/<br>Molecule           | Experimental<br>Wavelength<br>(nm) | Reference<br>Wavelength<br>(nm) | Wavelength<br>Difference<br>(nm) | Reference<br>Intensity<br>(a.u.) | Reference |
|-----------------------------|------------------------------------|---------------------------------|----------------------------------|----------------------------------|-----------|
| Fe                          | 259.26                             | 259.94                          | 0.68                             | 2000                             | [40]      |
| Fe                          | 280.03                             | 281.33                          | 1.3                              | 2500                             | [40]      |
| Mg <sup>+</sup>             | 280.6                              | 279.55                          | 1.05                             | 8/10                             | [40]      |
| Mg <sup>+</sup>             | 280.6                              | 280.27                          | 0.33                             | 8/10                             | [40]      |
| N <sub>2</sub>              | 294.95                             | 295.32                          | 0.37                             | 6/10                             | [41]      |
| OH                          | 307.29                             | 306.36                          | 0.93                             | 10/10                            | [41]      |
| OH                          | 308.67, 309.14                     | 308.9                           | 0.23, 0.24                       | 10/10                            | [41]      |
| N <sub>2</sub>              | 312.36                             | 313.6                           | 1.24                             | 8/10                             | [41]      |
| N <sub>2</sub>              | 315.31                             | 315.93                          | 0.62                             | 9/10                             | [41]      |
| CN <sup>+</sup>             | 317.89                             | 318.51                          | 0.62                             | 5/10                             | [41]      |
| O <sub>2</sub>              | 323.88                             | 323.2                           | 0.68                             | 9/10                             | [41]      |
| Cu                          | 324.17                             | 324.76                          | 0.59                             | 10k, 9/10                        | [40] [41] |
| Cu                          | 326.95                             | 327.4                           | 0.45                             | 10k, 1/10                        | [40] [41] |
| N <sub>2</sub> <sup>+</sup> | 334.47                             | 334.57                          | 0.1                              | 8/10                             | [41]      |
| NH                          | 335.85, 336.39                     | 336                             | 0.15, 0.39                       | 10/10                            | [41]      |
| Al I                        | 344.13                             | 344.364                         | 0.234                            | 150                              | [40]      |
| N <sub>2</sub>              | 352.41                             | 353.67                          | 1.26                             | 8/10                             | [41]      |
| N <sub>2</sub>              | 356.54, 357.14                     | 357.69                          | 1.15, 0.55                       | 10/10                            | [41]      |
| Al II                       | 361.13                             | 360.163                         | 0.967                            | 870                              | [40]      |
| N <sub>2</sub> <sup>+</sup> | 368.02                             | 368.21                          | 0.19                             | 7/10                             | [41]      |
| Fe                          | 363.82                             | 363.15                          | 0.67                             | 1200                             | [40]      |
| Fe                          | 368.82                             | 367.99                          | 0.83                             | 1500                             | [40]      |
| CO <sup>+</sup>             | 370.32                             | 370.53                          | 0.21                             | 4/10                             | [41]      |
| CO <sup>+</sup>             | 373.53                             | 372.97                          | 0.56                             | 3/10                             | [41]      |
| N <sub>2</sub>              | 373.99, 374.85                     | 375.54                          | 1.55, 0.69                       | 10/10                            | [41]      |
| N <sub>2</sub>              | 379.03, 379.84                     | 380.49                          | 1.46, 0.65                       | 10/10                            | [41]      |
| MgOH                        | 383.16                             | 383.48                          | 0.32                             | 6/10                             | [41]      |
| O <sub>2</sub>              | 390.03, 391.64                     | 391.4                           | 1.37, 0.24                       | 8/10                             | [41]      |
| Ca <sup>+</sup>             | 392.11                             | 393.37                          | 1.26                             | 230, 10/10                       | [40] [41] |
| N <sub>2</sub> <sup>+</sup> | 392.78                             | 391.44                          | 1.34                             | 6/10                             | [41]      |
| Ca <sup>+</sup>             | 395.79                             | 396.85                          | 1.06                             | 220, 10/10                       | [40] [41] |



| Atom/<br>Molecule            | Experimental<br>Wavelength<br>(nm) | Reference<br>Wavelength<br>(nm) | Wavelength<br>Difference<br>(nm) | Reference<br>Intensity<br>(a.u.) | Reference |
|------------------------------|------------------------------------|---------------------------------|----------------------------------|----------------------------------|-----------|
| Al                           | 396.45                             | 396.15                          | 0.3                              | 9k, 10/10                        | [40]      |
| Cl <sub>2</sub> <sup>+</sup> | 396.91                             | 396.15                          | 0.76                             | 5/10                             | [41]      |
| N <sub>2</sub>               | 398.28, 399.29                     | 399.84                          | 1.56, 0.55                       | 9/10                             | [41]      |
| N <sub>2</sub>               | 404.23, 405.26                     | 405.94                          | 1.71, 0.68                       | 8/10                             | [41]      |
| Fe                           | 405.47                             | 404.58                          | 0.89                             | 4000                             | [40]      |
| N <sub>2</sub> <sup>+</sup>  | 418.41, 418.87                     | 419.91                          | 1.50, 1.04                       | 2/10                             | [41]      |
| CaO                          | 421.52                             | 422.19                          | 0.67                             | 5/10                             | [41]      |
| N <sub>2</sub> <sup>+</sup>  | 422.06, 422.1                      | 423.65                          | 1.59, 1.55                       | 5/10                             | [41]      |
| N <sub>2</sub> <sup>+</sup>  | 425.79, 426.18                     | 427.81                          | 2.02, 1.63                       | 6/10                             | [41]      |
| N <sub>2</sub>               | 433.48                             | 434.36                          | 0.88                             | 4/10                             | [41]      |
| AlO                          | 437.13                             | 437.37                          | 0.24                             | 1/10                             | [41]      |
| AlO                          | 439.41                             | 439.38                          | 0.03                             | 1/10                             | [41]      |
| Cl <sub>2</sub> <sup>+</sup> | 466.75                             | 465.51                          | 1.24                             | 8/10                             | [41]      |
| Ti                           | 499.92                             | 499.95                          | 0.03                             | 4000                             | [40]      |
| N <sub>2</sub> <sup>+</sup>  | 517.14                             | 514.88                          | 2.26                             | 3/10                             | [41]      |
| N <sub>2</sub>               | 553.3                              | 552.71                          | 0.59                             | 2/10                             | [41]      |
| N <sub>2</sub> <sup>+</sup>  | 567.28                             | 565.31                          | 1.97                             | 1/10                             | [41]      |
| Na                           | 588.87                             | 588.99                          | 0.12                             | 80k, 10/10                       | [40] [41] |
| Na                           | 590.22                             | 589.592                         | 0.628                            | 40k                              | [40]      |
| Na                           | 590.22                             | 589.6                           | 0.62                             | 9/10                             | [41]      |
| N <sub>2</sub>               | 593.36                             | 592.4                           | 0.96                             | 1/10                             | [41]      |
| O <sub>2</sub>               | 777.59                             | 777.9                           | 0.31                             | 2/10                             | [41]      |

## **APPENDIX B**

### **FIRST GENERATION SINGLE CONTAMINANT MODEL**

The following MATLAB code (shown in Courier font) represents a template for calculating the capacitance of a single contaminant film, as a function of contaminant concentration. Values for the contaminant density ( $\rho_p$ ), bulk density ( $\eta$ ), ordinary dielectric constant ( $\epsilon_r$ ), and concentration ( $\beta_p$ ) are required by the user.

```
% Generic contaminant concentration to capacitance conversion template.
% First-generation version.

% Units: gram (g), liter (l), meter (m), farad (F).

clear all; clc; % Clear all data.

% Constants:

eta0 = 8.854e-12; % Permittivity of vacuum (F/m).
etaAIR = 1.00054; % Permittivity of air.
eta_p = X; % Permittivity of contaminant.
rho_p = X; % Density of contaminant (g/m^3).
nu_p = X; % Bulk density of contaminant (g/m^3).
beta_p = X; % Contaminant concentration (g/l).

% Device parameters:

h = 0.001; % Height of capacitor plate (m).
l = 0.01; % Length of capacitor plate (m).
d = 0.0010; % Capacitor plate spacing (m).
v_s = 0.001; % Sample size (l).

Acap = l*h; % Area of capacitor plate (m^2).
Abase = d*l; % Area of chamber base. (m^2).

% Analysis:

m = beta_p *v_s; % Tot. mass of cont. in sample (g).
x = m/(nu_p*Abase); % Height of TSS in base (m).
y = h - x; % Height of air in base (m).

phi_p = nu_p/rho_p; % Height of cont. film in chamber (m).
y = h - x; % Height of air in chamber (m).
% Lichtenecker. composite permittivity.
eta = 10^((1-phiAir)*log10(etaAIR)+phi_p*log10(eta_p));

cAIR = etaAIR*eta0*y+l/d; % Capacitance of air space (F).
c_film = eta*eta0*x*l/d; % Capacitance of cont. film (F).
C = c_film + cAIR; % Total capacitance (F).

% Analysis Overview
%*****
fprintf('_____ \n\n');
fprintf('Total capacitance = %g [F]\n',C);
fprintf('Capacitance contribution of contaminant film = %g [F]\n',c_film);
fprintf('Capacitance contribution of air in film = %g [F]\n',cAIR);
fprintf('Effective dielectric constant = %g \n',eta);
fprintf('Contaminant coating height = %g [m]\n',x);
fprintf('Volume percent of TSS in coating = %g \n',phi_p);
fprintf('Volume percent of air in coating = %g \n',phiAir);
fprintf('_____ \n');
```

## **APPENDIX C**

### **FIRST GENERATION MULTIPLE CONTAMINANT MODEL**

The following MATLAB code (shown in Courier font) represents a template for calculating the capacitance of a contaminant film with multiple contaminant species as a function of contaminant concentration. Values for the contaminant density ( $\rho_p$ ), bulk density ( $\eta$ ), ordinary dielectric constant ( $\epsilon_r$ ), and concentration ( $\beta_p$ ) are required by the user. Each contaminant species relative fraction is represented by  $a_{Al2O3}$ ,  $b_{NaCl}$ , and  $c_{SiO2}$ .

```
% Generic multi-contaminant concentration to capacitance conversion template.
% First-generation version.

% Contaminants: Al2O3, NaCl, and SiO2.

% Units: gram (g), liter (l), meter (m), farad (F).

clear all; clc; % Clear all data.

% Constants:

eta0 = 8.854e-12; % Permittivity of vacuum (F/m).
etaAIR = 1.00054; % Permittivity of air.
etaNaCl = 5.9; % Permittivity of NaCl.
etaAl2O3 = 10.07; % Permittivity of Al2O3.
etaSiO2 = 4.53; % Permittivity of SiO2.
rhoNaCl = 2.17e6; % Density of NaCl (g/m^3).
rhoAl2O3 = 3.97e6; % Density of Al2O3 (g/m^3).
rhoSiO2 = 2.648e6; % Density of SiO2 (g/m^3).
nuNaCl = 0.916e6; % Bulk density of NaCl (g/m^3).
nuAl2O3 = 1.322e6; % Bulk density of Al2O3 (g/m^3).
nuSiO2 = 0.908e6; % Bulk density of SiO2 (g/m^3).
beta_p = X; % Contaminant concentration (g/l).

a = X; % Fraction of NaCl in sample.
b = X; % Fraction of SiO2 in sample.
c = X; % Fraction of Al2O3 in sample.

% Device parameters:

h = 0.001; % Height of capacitor plate (m).
l = 0.01; % Length of capacitor plate (m).
d = 0.001; % Capacitor plate spacing (m).
v_s = X; % Sample size (l).

Acap = l*h; % Area of capacitor plate (m^2).
Abase = d*l; % Area of chamber base. (m^2).

% Analysis:

m = rho_p*v_s; % Tot. mass of cont. in sample (g).
mNaCl = m*a; % Mass of NaCl in sample (g).
mSiO2 = m*b; % Mass of SiO2 in sample (g).
mAl2O3 = m*c; % Mass of Al2O3 in sample (g).

vNaCl = mNaCl/pNaCl; % "Solid" vol. of NaCl (m^3).
vSiO2 = mSiO2/pSiO2; % "Solid" vol. of SiO2 (m^3).
vAl2O3 = mAl2O3/pAl2O3; % "Solid" vol. of Al2O3 (m^3).
v = vNaCl + vSiO2 + vAl2O3; % Combined "solid" volume (m^3).
rho = (mNaCl + mSiO2 + mAl2O3)/v; % Combined "solid" density (g/m^3).
```

```

nu_v_NaCl = mNaCl/nu_NaCl;          % "Porous" vol. of NaCl (m^3).
nu_v_SiO2 = mSiO2/nu_SiO2;         % "Porous" vol. of SiO2 (m^3).
nu_v_Al2O3 = mAl2O3/nu_Al2O3;      % "Porous" vol. of Al2O3 (m^3).
nu_v = nu_v_NaCl + nu_v_SiO2 + nu_v_Al2O3; % Combined "porous" volume (m^3).
nu = (mNaCl + mSiO2 + mAl2O3)/ nu_v; % Combined "porous" density (g/m^3).

phiNaCl = vNaCl/nu_v;               % Vol. % of NaCl particles (m^3).
phiSiO2 = vSiO2/nu_v;               % Vol. % of SiO2 particles (m^3).
phiAl2O3 = vAl2O3/nu_v;             % Vol. % of Al2O3 particles (m^3).
phiAir = (nu_v-vNaCl-vSiO2-vAl2O3)/nu_v; % Vol. % of air (m^3).
phi = phiNaCl+phiSiO2+phiAl2O3+phiAir; % Verify tot. vol. % is unity (m^3).

x = m/nu_p/Abase;                   % Height of cont. film in chamber (m).
y = h - x;                           % Height of air in chamber (m).

r =
(phiAir)*log10(etaAIR)+(phiNaCl)*log10(etaNaCl)+(phiSiO2)*log10(etaSiO2)+(phiAl
2O3)*log10(etaAl2O3);                % Lich. eq. exponent
eta = 10^(r);                         % Lich. composite permittivity.

cAIR = etaAIR*eta0*y*l/d;             % Capacitance of air space (F).
c_film = eta*eta0*x*l/d;              % Capacitance of cont. film (F).
C = c_film + cAIR;                    % Total capacitance (F).

% Analysis Overview
%*****
fprintf('_____ \n\n');
fprintf('Total capacitance = %g [F]\n',C);
fprintf('Capacitance contribution of contaminant film = %g [F]\n',c_film);
fprintf('Capacitance contribution of air in film = %g [F]\n',cAIR);
fprintf('Effective dielectric constant = %g \n',eta);
fprintf('Contaminant coating height = %g [m]\n',x);
fprintf('Volume percent of NaCl in coating = %g \n',phiNaCl);
fprintf('Volume percent of Al2O3 in coating = %g \n',phiAl2O3);
fprintf('Volume percent of SiO2 in coating = %g \n',phiSiO2);
fprintf('Volume percent of air in coating = %g \n',phiAir);
fprintf('_____ \n\n');

```

## **APPENDIX D**

### **SECOND GENERATION SINGLE CONTAMINANT MODEL**

The following MATLAB code (shown in Courier font) represents a template for calculating the capacitance of a contaminant film with a single contaminant species as a function of contaminant concentration, based on the updated Lichtenecker formulation in [55] and [56]. Values for the contaminant density ( $\rho_p$ ), bulk density ( $\eta$ ), ordinary dielectric constant ( $\epsilon_r$ ), and concentration ( $\beta_p$ ) are required by the user.

```
% TSS concentration to capacitance conversion
% Based on modified Lichtenecker's

% Contaminants: MgO, CaCO3, and NaCl.

% Units: gram (g), liter (l), meter (m), farad (F).

clear all; clc; % Clear all data.

% Constants:

eta0 = 8.854e-12; % Permittivity of vacuum (F/m).
eta_contaminant = X; % Permittivity of contaminant.
etaAIR = 1.00054; % Permittivity of air.
etaCuO = 18.1; % Permittivity of CuO.
etaCu2O = 7.6; % Permittivity of Cu2O.
dCuO = 1.3e-9; % Thickness of CuO layer (m).
dCu2O = 2.0e-9; % Thickness of Cu2O layer (m).
nu_p = Xe6; % Bulk density of contaminant (g/m^3).
rho_p = Xe6; % Solid density of contaminant (g/m^3).
e = 0.000000000001; % Eccentricity of particles.
beta_p = X; % Contaminant concentration (g/l).

% Device parameters:

h = 0.001015; % Height of capacitor plate (m).
l = 0.01032; % Length of capacitor plate (m).
d = 0.00101; % Capacitor plate spacing (m).
v_s = 0.001; % Sample size (l).

% Analysis:

mass = beta_p*ss; % Contaminant mass in sample (g).
x = mass/(nu_p*d*l); % Height of TSS in chamber (m).
y = h - x; % Height of air in chamber (m).
phi_p = nu_p /rho_p; % Contaminant vol.% in coating.

phiAIR = 1-phi_contaminant; % Air vol.% in coating.

%*****

m = e^2*(1-sqrt(1-e^2)*(asin(e)/e))^-1;
M = 2/(m-1);
n = (5-M)/4; % n<1, n>=0.

a = (etaNaCl+etaAIR)/(2*(etaNaCl-etaAIR)*log(etaNaCl/etaAIR));
b = etaNaCl*etaAIR/((etaNaCl-etaAIR)^2);
t = a-b;
phi1 = 0.5-0.5*sqrt(1-4*t);
phi2 = 1-phi1;
```



```

etaUphiNaCl = (phiNaCl*etaNaCl)+((1-phiNaCl)*etaAIR);
etaLphiNaCl = ((phiNaCl/etaNaCl)+((1-phiNaCl)/etaAIR))^-1;

etaUphi1 = (phi1*etaNaCl)+((1-phi1)*etaAIR);
etaLphi1 = ((phi1/etaNaCl)+((1-phi1)/etaAIR))^-1;

etaUphi2 = (phi2*etaNaCl)+((1-phi2)*etaAIR);
etaLphi2 = ((phi2/etaNaCl)+((1-phi2)/etaAIR))^-1;

Aphi1 = 1+((etaUphi1^n)*(etaLphi1^n))^-1;

Bphi2 = 1+((etaUphi1^(n-1))*(etaLphi1^(n-1)))^-1;

Cphi = (sqrt(etaLphiNaCl/etaUphiNaCl))*(etaNaCl^phiNaCl)...
      *(etaAIR^(1-phiNaCl));
Cphi1 = (sqrt(etaLphi1/etaUphi1))*(etaNaCl^phi1)*(etaAIR^(1-phi1));
Cphi2 = (sqrt(etaLphi2/etaUphi2))*(etaNaCl^phi2)*(etaAIR^(1-phi2));

Zphi = (etaUphiNaCl^n)/(etaLphiNaCl^(n-1));

eta = 0.5*((Aphi1/(2*Cphi1))+(Bphi2/(2*Cphi2)))*Cphi*Zphi;

%*****

CAIR = (etaAIR*eta0*y*1/d)/(1e-12);      % Capacitance of air space (pF).
Cfilm = (eta*eta0*x*1/d)/(1e-12);      % Capacitance of film (pF).
CCuO = (etaCuO*eta0*h*1/dCuO)/(1e-12); % Capacitance of CuO layer (pF).
CCu2O = (etaCu2O*eta0*h*1/dCu2O)/(1e-12); % Capacitance of Cu2O (pF).
mu_x = x/(1e-6);                       % Contaminant film thickness (um).

Cchamber = Cfilm + CAIR;                % Total capacitance of chamber. (pF).
C = 1/((2/CCuO)+(2/CCu2O)+(1/Cchamber)); % Total capacitance (pF)

% Analysis Overview
%*****
fprintf('_____ \n\n');
fprintf('Total capacitance = %g [F]\n',C);
fprintf('Capacitance contribution of contaminant in coating = %g [F]\n',Cfilm);
fprintf('Capacitance contribution of air in coating = %g [F]\n',CAIR);
fprintf('Contaminant coating height = %g [m]\n',mu_x);
fprintf('Effective dielectric constant = %g \n',eta);
fprintf('Volume percent of NaCl in coating = %g \n',phiNaCl);
fprintf('Volume percent of air in coating = %g \n',phiAIR);
fprintf('_____ \n');

```

## BIBLIOGRAPHY

- [1] Ruston Water Utilities, "Annual Water Quality Report," Water Utilities, City of Ruston, Ruston, 2011.
- [2] United States Environmental Protection Agency, *EPA Guidance Manual: Turbidity Provisions*. USA: Environmental Protection Agency, 1999.
- [3] A. Prüss-Üstün *et al.*, "Safer Water, Better Health (2012 Update)," World Health Organization, 2008. [Online].  
[http://whqlibdoc.who.int/publications/2008/9789241596435\\_eng.pdf](http://whqlibdoc.who.int/publications/2008/9789241596435_eng.pdf)
- [4] World Health Organization, "Progress on Drinking Water and Sanitation: JMP Update 2012," UNICEF/World, March 2012. [Online].  
[http://whqlibdoc.who.int/publications/2012/9789280646320\\_eng\\_full\\_text.pdf](http://whqlibdoc.who.int/publications/2012/9789280646320_eng_full_text.pdf)
- [5] M. F. Craun *et al.*, "Waterborne outbreaks reported in the United States," *J. Wat. Health*, vol. 4, no. 2, pp. 19-30, 2006.
- [6] United States National Academy of Engineering. NAE Grand Challenges for Engineering. [Online].  
<http://www.engineeringchallenges.org/cms/8996/9142.aspx>
- [7] Louisiana Department of Environmental Quality, "Schedule A: effluent limitations and monitoring requirements for discharges of landfill wastewater from a construction/demolition debris and woodwaste landfill," Louisiana Department of Environmental Quality.
- [8] M. W. LeChevallier *et al.*, "Occurrence of *Giardia* and *Cryptosporidium* spp. in surface water supplies," *Appl. Env. Microbio.*, vol. 57, no. 9, pp. 2610-2616, September 1991.
- [9] M. W. LeChevallier *et al.*, "*Giardia* and *Cryptosporidium* spp. in filtered drinking water supplies," *Appl. Env. Microbio.*, vol. 57, no. 9, pp. 2617-2621, September 1991.

- [10] R. A. Guy *et al.*, "Real-time PCR for quantification of *Giardia* and *Cryptosporidium* in environmental Water Samples and Sewage," *Appl. Environ. Microbiol.*, vol. 69, no. 8, pp. 5178-5185, Sept 2003.
- [11] K C Marshall, *Interfaces in Microbial Ecology*. Cambridge, MA, USA: Harvard University Press, 1976.
- [12] B. H. Olson *et al.*, "Bacterial colonization of mortar-lined and galvanized iron water distribution mains," in *Am. Water Works Assoc. Nat. Conf.*, Denver, 1981.
- [13] D. S. Herson *et al.*, "Bacterial persistence in the distribution system," *J. Am. Water Works Assoc.*, vol. 76, pp. 309-322, 1984.
- [14] National Research Council, *Drinking Water and Health*. Washington, D.C.: National Academy Press, 1980, vol. 2.
- [15] S. Hatukai *et al.*, "Particle counts and size distribution in system design for removal of turbidity by granular deep bed filtration," *Wat. Sci. Tech.*, vol. 36, no. 4, pp. 225-230, 1997.
- [16] United States Environmental Protection Agency, *Methods for Chemical Analysis of Water and Wastes*, 2nd ed. Cincinnati, OH, USA: United States Environmental Protection Agency, 1982.
- [17] W. Hou *et al.*, "Why does the Secchi disk disappear? An imaging perspective," *Opt. Express*, vol. 15, no. 6, pp. 2791-2801, March 2007.
- [18] United States Environmental Protection Agency. (2012, March) United States Environmental Protection Agency. [Online].  
<http://water.epa.gov/type/rsl/monitoring/vms55.cfm>
- [19] United States Environmental Protection Agency. (2013, March) United States Environmental Protection Agency. [Online].  
<http://water.epa.gov/type/rsl/monitoring/155.cfm>
- [20] United States Environmental Protection Agency. (2013, June) United States Environmental Protection Agency. [Online].  
<http://water.epa.gov/drink/contaminants/index.cfm>
- [21] United States Environmental Protection Agency, "EPA Method 160.2," United States Environmental Protection Agency, 1971.

- [22] United States Environmental Protection Agency, "ESS Method 340.2," United States Environmental Protection Agency, 1993.
- [23] Z. Jin *et al.*, "A low-power atmospheric pressure pulsed plasma source for molecular emission spectrometry," *Anal. Chem.*, vol. 73, no. 2, pp. 360-365, January 2007.
- [24] J. C. T. Eijkel *et al.*, "A molecular emission detector on a chip employing a direct current microplasma," *Anal. Chem.*, vol. 71, no. 14, pp. 2600-2606, July 1999.
- [25] J. C. T. Eijkel *et al.*, "An atmospheric pressure dc glow discharge on a microchip and its application as a molecular emission detector," *J. Anal. At. Spectrom.*, vol. 15, pp. 297-300, 2000.
- [26] J. C. T. Eijkel *et al.*, "A dc microplasma on a chip employed as an optical emission detector for gas chromatography," *Anal. Chem.*, vol. 72, no. 11, pp. 2547-2552, June 2000.
- [27] F. G. Bessoth *et al.*, "Towards an on-chip gas chromatograph: the development of a gas injector and a dc plasma emission detector," *J. Anal. At. Spectrom.*, vol. 17, pp. 794-799, 2002.
- [28] C. G. Wilson *et al.*, "Profiling and modeling of dc nitrogen microplasmas," *J. Appl. Phys.*, vol. 94, no. 5, pp. 2845-2851, September 2003.
- [29] C. G. Wilson and Y. B. Gianchandani, "Miniaturized magnetic nitrogen dc microplasmas," *IEEE Trans. Plasma Sci.*, vol. 32, no. 1, pp. 282-287, February 2004.
- [30] G. G. Wilson and Y. B. Gianchandani, "Spectral detection of metal contaminants in water using an on-chip microglow discharge," *IEEE Trans. Electron Devices*, vol. 49, no. 12, pp. 2317-2322, December 2002.
- [31] L. Que *et al.*, "Microfluidic electrodischarge devices with integrated dispersion optics for spectral analysis of water impurities," *JMEMS*, vol. 14, no. 2, pp. 185-191, April 2005.
- [32] R. Yalavarthy and C. G. Wilson, "S-MAYHEM: a spectroscopic microanalytical hollow enhanced magnetron for explosive gas detection," in *IEEE MEMS Conference*, Istanbul, Turkey, 2006, pp. 362-365.

- [33] V. Karanassios *et al.*, "Elemental analysis of micro-samples of liquids or slurries by coiled-filament in-torch vaporization-inductively coupled plasma atomic emission spectrometry (ITV-ICP-AES)," *J. Anal. At. Spectrom.*, vol. 14, pp. 565-570, 1999.
- [34] H. R. Badiei and V. Karanassios, "Rhenium-cup in-torch vaporization inductively coupled plasma atomic emission spectrometry for liquid, slurry, or solid micro-samples," *J. Anal. At. Spectrom.*, vol. 15, pp. 1057-1062, 2000.
- [35] K. Johnson *et al.*, "Micro-fluidics in environmental monitoring: liquid micro-samples by an in-torch vaporization - micro-plasma device (ITV-MPD)," in *Adv. Env. Chem. Sens. Tech.*, vol. 4205, Boston, 2001, pp. 347-352.
- [36] S. J. Hill, Ed., *Inductively Coupled Plasma Spectrometry and its Applications*, 2nd ed. Oxford, UK: Blackwell Publishing, 2007.
- [37] D. W. Ball, *The Basics of Spectroscopy*, 1st ed. Bellingham, WA, USA: SPIE Press, 2001.
- [38] J. M. Hollas, *Modern Spectroscopy*, 4th ed. West Sussex, England: John Wiley & Sons, Ltd., 2009.
- [39] M. E. Zorn *et al.*, "Detection of aqueous metals using a microglow discharge atomic emission sensor," *Sensor Letters*, vol. 2, no. 3, pp. 179-185, 2004.
- [40] CRC Press, Inc., *CRC Handbook of Chemistry and Physics*, 77th ed., D. R. Lie, Ed. Boca Raton, FL, USA: CRC Press, Inc., 1996.
- [41] R. W. B. Pearse and A. G. Gaydon, *The Identification of Molecular Spectra*, 3rd ed. New York, NY, USA: John Wiley & Sons, Inc., 1963.
- [42] M. J. Madou, *Fundamentals of Microfabrication: The Science of Miniaturization*, 2nd ed. Boca Raton, FL, USA: CRC Press, LLC, 2002.
- [43] Ocean Optics, Inc. Ocean Optics, Inc. [Online].  
<http://www.oceanoptics.com/Products/HR2000CG.asp>
- [44] Alfa Aesar, "Silicon dioxide (13024)," Alfa Aesar, Ward Hill, Material Safety Data Sheet 2001.
- [45] D. J. Giffiths, *Introduction to Electrodynamics*, 3rd ed. Upper Saddle River, New Jersey, USA: Pearson Addison Welsey, 1999.

- [46] A. V. Goncharenko *et al.*, "Lichtenecker's equation: applicability and limitations," *Opt. Commun.*, vol. 174, pp. 19-32, January 2000.
- [47] Y. Zheng *et al.*, "Measurement of the complex permittivity of dry rocks and minerals: application of polythene dilution method and Lichtenecker's mixtures formulae," *Geophys. J. Int.*, vol. 163, no. 3, pp. 1195–1202, December 2005.
- [48] S. D. Cho *et al.*, "Comparison of theoretical predictions and experimental values of the dielectric constant of epoxy/BaTiO<sub>3</sub> composite embedded capacitor films," *J. of Mat. Sci.: Mat. in Electron.*, vol. 16, no. 2, pp. 77-84, February 2005.
- [49] R. Simpkin, "Derivation of Lichtenecker's logarithmic mixture formula from Maxwell's equations," *IEEE Trans. Microw. Theory Tech.*, vol. 58, no. 3, pp. 545-550, March 2010.
- [50] K. Lichtenecker, "Die Dielektrizitätskonstante natürlicher und künstlicher Mischkörper," *Phys. Zeitschr.*, vol. 27, pp. 115-158, 1926.
- [51] K. Lichtenecker and K. Rother, "Die Herleitung des logarithmischen Mischungsgesetzes aus allgemeinen Prinzipien der stationären Stromung," *Phys. Zeitschr.*, vol. 32, pp. 255-260, 1931.
- [52] Y. Wu *et al.*, "Evaluation of mixing rules for dielectric constants of composite dielectrics by MC-FEM calculation on 3D cubic lattice," *J. Electroceram.*, vol. 11, pp. 227-239, 2003.
- [53] Y. Rao *et al.*, "A precise numerical prediction of effective dielectric constant for polymer-ceramic composite based on effective-medium theory," *IEEE Trans. Compon. Packag. Technol.*, vol. 23, no. 4, pp. 680-683, December 2000.
- [54] E. M. Kiley *et al.*, "Applicability study of classical and contemporary models for effective complex permittivity of metal powders," *J. Microw. Power Electromagn. Energy*, vol. 46, no. 1, pp. 26-38, March 2012.
- [55] S. Kisdnasamy and P. S. Neelakantaswamy, "Complex permittivity of a dielectric mixture: modified Fricke's formula based on logarithmic law of mixing," *IEEE Sensors Lett.*, vol. 20, no. 7, pp. 291 - 293, March 1984.
- [56] P. S. Neelakantaswamy *et al.*, "Complex permittivity of a dielectric mixture: corrected version of Lichtenecker's logarithmic law of mixing," *IEEE Sensors Lett.*, vol. 21, no. 7, pp. 270-271, March 1985.

- [57] A. R. Jumikis, *Soil Mechanics*. Malabar, FL, USA: Robert E. Krieger Publishing Co., Inc., 1984.
- [58] Analog Devices, Inc., "AD7745/AD7746: 24-Bit Capacitance-to-Digital Converter with Temperature Sensor Datasheet," Norwood, MA, USA, 2005.
- [59] Alfa Aesar, "Aluminum oxide (10627)," Alfa Aesar, Ward Hill, Material Safety Data Sheet 2011.
- [60] Alfa Aesar, "Sodium chloride (12314)," Alfa Aesar, Ward Hill, Material Safety Data Sheet 2011.
- [61] K. F. Young and H. P. R. Frederikse, "Compilation of the static dielectric constant of inorganic solids," *J. Phys. Chem. Ref. Data*, vol. 2, no. 2, pp. 313-409, 1973.
- [62] B. K. Hough, *Basic Soils Engineering*. New York, NY, USA: The Ronald Press Company, 1957.
- [63] P. Keil *et al.*, "Investigation of room temperature oxidation of Cu in air by Yoneda-XAFS," in *AIP Conf.*, vol. 882, 2007.
- [64] EMCO High Voltage Corporation, "Ultra-Miniature DC to HV DC Converters," Sutter Creek, CA, USA,.
- [65] Alfa Aesar, "Calcium carbonate (43280)," Alfa Aesar, Ward Hill, MA, USA, Material Safety Data Sheet 2012.
- [66] Alfa Aesar, "Magnesium oxide (44733)," Alfa Aesar, Ward Hill, Material Safety Data Sheet 2012.
- [67] J. W. Sweeney *et al.*, "A plasma spectroscopic microdevice for on-site water monitoring," in *IEEE Sensors Conf.*, Christchurch, 2009, pp. 2005-2008.
- [68] J. W. Sweeney and C. G. Wilson, "Dusty plasmas for on-site spectroscopic analysis of water sources," in *SPIE Eur. Sec. + Def. Conf.*, vol. 7484, Berlin, 2009.